Towards the use of surrogate modeling in model parameter calibration in injection molding process simulation

Sandra Saad

▶ To cite this version:

Sandra Saad. Towards the use of surrogate modeling in model parameter calibration in injection molding process simulation. Chemical and Process Engineering. HESAM Université, 2022. English. NNT : 2022HESAE058 . tel-04042475

HAL Id: tel-04042475
https://pastel.hal.science/tel-04042475
Submitted on 23 Mar 2023

HAL is a multi-disciplinary open access archive for the deposit and dissemination of scientific research documents, whether they are published or not. The documents may come from teaching and research institutions in France or abroad, or from public or private research centers.

L'archive ouverte pluridisciplinaire **HAL**, est destinée au dépôt et à la diffusion de documents scientifiques de niveau recherche, publiés ou non, émanant des établissements d'enseignement et de recherche français ou étrangers, des laboratoires publics ou privés.

HESAM UNIVERSITÉ

Arts et Métiers Sciences et Technologies

ÉCOLE DOCTORALE SCIENCES ET MÉTIERS DE L'INGÉNIEUR
LAMPA - Campus d'Angers

THÈSE

présentée par : **Sandra SAAD**
soutenue le : **18 Novembre 2022**

pour obtenir le grade de : **Docteur d'HESAM Université**

préparée à : **École Nationale Supérieure d'Arts et Métiers**
Spécialité : **Procédés de fabrication - Génie mécanique (AM)**

Towards the use of surrogate modeling in model parameter calibration in injection molding process simulation

THÈSE dirigée par :
Mme SAAD Sandra

et co-encadrée par :
Prof. AMMAR Amine
Prof. RÉGNIER Gilles
Dr. CRUZ Camilo

Jury

Mme Nadia EL KISSI	Directrice de recherche, Laboratoire Rhéologie et Procédés, Université Grenoble Alpes	Présidente
M. Elias CUETO	Prof., Aragón Institute of Engineering Research, Universidad de Zaragoza	Rapporteur
M. Rudy VALETTE	Prof., Centre de Mise en Forme des Matériaux, Mines Paris	Rapporteur
M. Jan-Martin KAISER	Dr., Senior Manager, Robert Bosch GmbH, Renningen	Examinateur
M. Camilo CRUZ	Dr., Project Manager, Robert Bosch GmbH, Renningen	Examinateur
M. Amine AMMAR	Prof., LAMPA, Arts et Métiers ParisTech	Examinateur
M. Gilles RÉGNIER	Prof., PIMM, Arts et Métiers ParisTech	Examinateur

THÈSE

Acknowledgments

First of all, I would like to take this opportunity to express my deepest gratitude to my university supervisors Prof. Amine Ammar and Prof. Gilles Régnier. Their support and guidance throughout my PhD time was instrumental to my work and its success. They were always ready to offer me their time and knowledge to help me advance in my research. I consider myself very lucky to have had them as supervisors.

As this PhD work was done in cooperation with Robert Bosch GmbH (Corporate Sector Research and Advance Engineering), I was fortunate enough to have Dr. Camilo Cruz as my co-supervisor. He helped me tremendously and without his mentoring and direction this work would not have been possible. I learned a lot from him both professionally and personally and for that I am really grateful.

Moreover, I would like to express my deepest appreciation to Prof. Elias Cueto and Prof. Rudy Valette for reviewing my thesis and for the insightful discussions during my defense. Additionally, my appreciation goes to the president of the jury Prof. Nadia El Kissi, it was an honor to have you part of my jury.

I would also like to extend my sincere thanks to Dr. Jan-Martin Kaiser for being a supportive manager and helping me in my development as well as being part of my jury. Many thanks to Dr. Martin Giersberg, Dr. Marcus Lechmann and Cosima Thomas, as managers, they provided me with all the tools and opportunities needed for me to reach my goal. During my time as a PhD candidate at Bosch, I had the chance to get the guidance and help from many of my colleagues and for that I am very grateful. I would like to thank every colleague that was part of my journey and special thanks go to Dr. Michael Schick, Armin Kech and Juergen Denzingen.

Furthermore, I was fortunate to have the support of Alankar Sinha during my PhD. His master thesis work was one of the main building blocks of my final work and I am grateful that we got the chance to work together. I also had the pleasure of being part of a great PhD program community at Bosch which helped me meet a lot of interesting people. Through this community, I was able to form great friendships and get the technical and mental support needed to go on with my research.

Finally and most importantly, I would like to thank my family and my partner for their tremendous support and love. Their presence in my life and their constant motivation are the main reason I was able to push through and finalize this work.

Abstract

The computational costs of injection molding simulations have been increasing in the past years due to the higher complexity of the embedded models. This is especially problematic in case of using such simulation models for optimization routines or sensitivity analyses. One way to overcome this challenge is by having a surrogate model, also known as a metamodel, of these high-fidelity simulations, which provides a cheaper way to perform these types of analyses. These surrogate models can play an important role in the case of the injection molding of semi-crystalline polymers to model the flow-induced crystallization process. To date, most commercial software do not explicitly take polymer crystallization into account leading to various errors in the fill predictions as well as the calculation of warpage and shrinkage. This is mainly due to the common complexity of the models used to describe crystallization and the challenging respective model parameter identification process under injection molding conditions. To close this gap, in this thesis, the feasibility of using surrogate modeling to identify modeling parameters is first studied. This is then followed by the implementation of a thermo-mechanical crystallization model in order to describe the flow-induced and quiescent crystallization of an unreinforced semi-crystalline thermoplastic material during injection molding. The crystallization model is defined alongside crystallization-dependent viscosity, PVT and solidification models in the commercial software Autodesk® Moldflow® Insight 2021 using the Solver API feature. The model parameters are identified using a calibration scheme that employs three surrogate models representing the simulated pressure results to perform a multi-objective optimization. The fill predictions as well as the calculated pressure fields are presented using the calibrated model parameters in comparison to those measured during the actual injection molding of a polyoxymethylene part with different process conditions. The results show major improvements in the predictions of the pressure signals as well as the filling status of the produced parts and the estimated skin layer thicknesses formed under high-shear conditions. Additionally, the calibrated models are tested using various mold geometries to assess the calibrated models' performance.

Keywords: surrogate modeling, injection molding, crystallization, simulation, thermoplastic, model parameter, metamodel.

Résumé

Les coûts de calcul des simulations du procédé de moulage par injection ont augmenté au cours des dernières années en raison de la complexité accrue des modèles intégrés. Ceci est particulièrement problématique pour des calculs d'optimisation de pièces ou pour les analyses de sensibilité de paramètres. Une façon de surmonter ce problème est d'implémenter des métamodèles pour réaliser ces simulations haute-fidélités. Ces métamodèles peuvent jouer un rôle important dans le cas du moulage par injection de polymères semi-cristallins pour modéliser le processus de cristallisation induit par l'écoulement. À ce jour, la plupart des logiciels commerciaux ne prennent pas explicitement en compte la cristallisation des polymères, ce qui conduit à diverses erreurs dans les prédictions de remplissage, d'évolution des champs de contraintes et dans les prédictions dimensionnelles. La faisabilité de l'utilisation des métamodèles pour identifier les paramètres d'un modèle physique est d'abord présentée. Il s'en suit la mise en œuvre d'un modèle de cristallisation thermo-mécanique afin de décrire la cristallisation induite par l'écoulement d'un matériau thermoplastique semi-cristallin non renforcé pendant le procédé de moulage par injection. Le modèle de cristallisation est couplé aux modèles de viscosité et PVT dans le logiciel commercial Autodesk® Moldflow® Insight 2021 en utilisant la fonction Solver API. Les paramètres du modèle sont identifiés à l'aide d'un schéma de recalage qui utilise trois différents métamodèles représentant les résultats de pression simulés pour effectuer une optimisation multi-objectifs. Les prédictions de remplissage ainsi que les pressions calculées sont présentées en utilisant les paramètres du modèle calibré en comparaison avec celles mesurées pendant le moulage par injection réel d'une pièce en polyoxyméthylène avec différentes conditions de processus. Les résultats montrent des améliorations majeures dans les prédictions des signaux de pression ainsi que dans l'état de remplissage des pièces produites et les épaisseurs estimées de la couche de peau formée dans des conditions de cisaillement élevé. Les modèles recalés sont testés en utilisant différentes géométries de moules pour évaluer leurs performances.

Mots-clés : modélisation de substitution, moulage par injection, cristallisation, simulation, thermoplastique, paramètre de modèle, métamodèle.

Contents

List of Tables

List of Figures

Introduction

Injection molding is one of the main polymer processing techniques with which more than one-third of thermoplastic materials are produced [1]. The injection molding process is cyclic and ideal for the mass-production of complex geometries with tight tolerances [2]. In the case of part defects during production, a change in process conditions may not be sufficient and mold modifications must be applied to solve the problem [3]. However, this is expensive and time-consuming. Thus, it is important to be able to foresee such issues in the design phase of the part using simulation techniques. Therefore, to minimize such costs while guaranteeing a superior product quality, injection molding simulation is widely used to efficiently design molds and provide a tool to determine optimal process settings that overcome commonly observed defects such as warpage, shrinkage and short shots.

However, over the last years, the growing interest in highly accurate simulations resulted in the increase of the complexity of the embedded models and in turn to higher computational costs. This problem is specifically underlined when using such simulation models for optimization, sensitivity analyses or uncertainty quantification. Surrogate modeling offers a way to overcome the limitation of these high-fidelity simulations and to perform such analyses in a more cost- and time-efficient way. These models are usually generated using a relatively low number of simulations obtained by varying a specific number of input parameters and are then able to approximate the output of interest in a matter of seconds instead of minutes or hours using the high-fidelity simulation. An example application is presented in Figure 1 where a surrogate model is used to calibrate simulation model parameters by performing an efficient optimization routine. In the presented case, the surrogate model represents one output result learned from running multiple high-fidelity simulation runs and is then used independently to obtain the optimal input parameters that best fit the experimental results.

Currently, in the field of injection molding simulation, the use of surrogate modeling in the literature is mainly limited to the optimization of process parameters such as the mold and melt temperatures

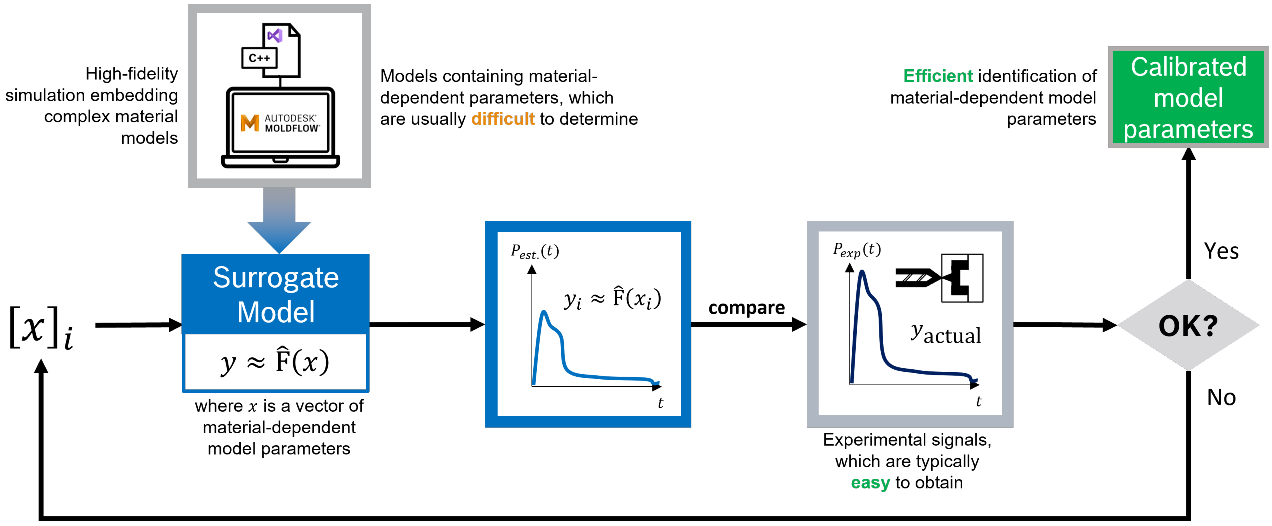

Figure 1 – Model parameter optimization scheme using a surrogate model [4].

[5, 6], packing and cooling times [7, 8], packing pressure [9, 10]... One recent publication by Ivan et al. [11] stands out in which the authors use a surrogate model to identify two model parameters that describe the fiber orientation. A similar approach could be utilized to calibrate other types of complex material models such as a crystallization model. Due to the complexity of experimentally identifying crystallization parameters under injection molding conditions, many commercial software do not take it into account even when dealing with the injection of semi-crystalline materials. This leads to inaccuracies in the fill predictions as well as in the estimation of warpage and shrinkage in the simulation [3].

In the last decades, great efforts have been made in order to model polymer crystallization while taking into account the flow history of the melt. A common approach utilized to describe flow-induced crystallization, observed during injection molding, is based on the Avrami-Kolmogorov nucleation and growth theory [12, 13] combined with Schneider's rate equations [14]. Such method necessitates the experimental determination of a high number of model parameters and solving of an intricate and interdependent system of differential equations [15]. Whereas, Poitou et al. [16, 17] proposed a thermo-mechanical approach describing both the flow-induced and quiescent crystallization with a much smaller number of model parameters making it more attractive to use in simulation software.

The main aim of this thesis is the use of surrogate modeling in the model parameter calibration of a crystallization model implemented in an injection molding simulation. In order to reach this goal, a feasibility study is first performed to assess the use of different surrogate modeling techniques and design of experiments in calibrating modeling parameters in the injection molding simulation of a polyoxymethylene thermoplastic part. This is followed by the implementation of a modified Poitou et al.'s crystallization model along with crystallization-dependent viscosity, PVT and solidification models in the commercial software Autodesk® Moldflow® Insight 2021 using the Solver API feature. The models are implemented in 3D and calibrated using three surrogate models representing the simulated pressure at different processing conditions. The ability of the calibrated models to predict accurately the pressure, fill status and skin layer thickness is tested at different conditions using a base mold geometry and three variations of it.

Chapter 1

Theory and State of the Art

Content

1.1 Injection Molding Process

The injection molding process is one of the most widely used plastics manufacturing techniques in the industry such as more than one-third of all thermoplastic materials are injection molded [1,18]. It enables the high production volumes of complex plastic parts while having short cycle times [3]. A cycle constitutes mainly of six phases [1,3,18]:

1. Mold closing: the mold is closed to obtain the cavity into which the molten material is injected.
2. Injection/Filling: the screw moves forward and forces the melt into the mold cavity.
3. Packing/Holding: the screw is held in its forward position after the mold is filled in order to maintain a holding pressure that compensates for material shrinkage.
4. Cooling: the gate freezes and the cavity is isolated from the pressure applied by the melt, the part cools down and solidifies until ejected.
5. Plastication and screw back: the screw rotates back while plasticating the feed for the next shot which is now in a molten state in front of the screw.
6. Ejection: the mold opens when the part is sufficiently cooled and it is then ejected.

The total cycle time t_{cycle} of an injection molding process is given by [1]:

$$t_{cycle} = t_{closing} + t_{cooling} + t_{ejection} \tag{1.1}$$

where the closing time $t_{closing}$ and ejection times $t_{ejection}$ usually last less than a few seconds whereas the cooling time $t_{cooling}$ dominates the process as the polymer melt is being cooled as soon as it enters the cavity after the closing of the mold till it is ejected from it. Therefore, $t_{cooling}$ includes the cooling taking place during the filling and packing phases as the mold is closed and surrounds the polymer melt during these stages.

During the operation of an injection molding machine, plastic granules are fed through the hopper shown in the simplified sketch in Figure 1.1. The fed material is then transported forward by the rotating screw. The granules melt while being transported due to both the friction created by the screw and the conduction from heating units along the barrel. The molten material is injected into the mold by the screw typically with high flow rates and therefore high shear rates. The main heat transfer mechanism during the filling stage is through convection of the melt in addition to some viscous heating primarily in the runner system and the gates [3]. Heat is constantly removed by

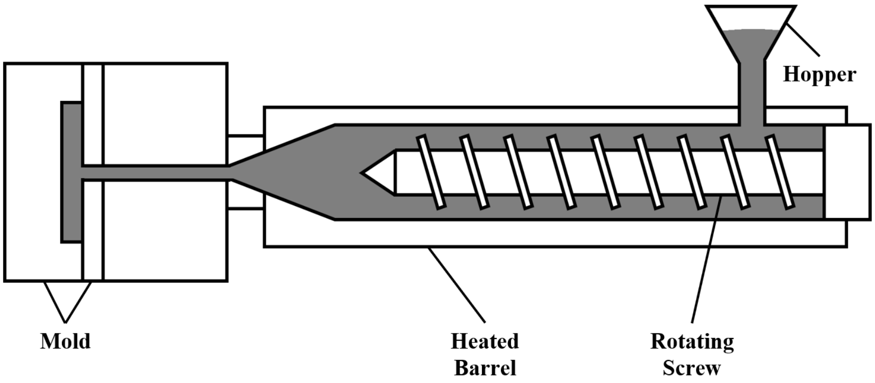

Figure 1.1 – Simple sketch of a reciprocating-screw injection molding machine, based on [18].

conduction through the mold wall to the cooling system. This leads to the formation of a frozen layer or skin layer near the wall. During the packing stage, the flow rates are relatively low and conduction becomes the main heat transfer mechanism leading to the increase of this frozen layer until the gate freezes followed by the solidification of the part due to conduction until it is ejected from the mold.

1.2 Injection Molding Simulation

To ensure high product quality and minimize design/production costs, injection molding simulation is broadly used in order to efficiently design molds and enable the identification of optimal process settings that mitigate common defects such as warpage, shrinkage, weldline and short shots. The simulation of the injection molding process constitutes using a numerical method with well-defined material models to solve a set of conservation equations [3]. Many commercial and academic software have been developed to tackle this problem which involves multiple heating mechanisms as described in Section 1.1 in addition to a phase change and time-dependent boundary conditions at the frozen layer during the various phases of the process. Taking into account all these complex physical phenomena in the simulation is not straightforward and necessitates some simplifying assumptions and approximations.

1.2.1 Main Approximations

These approximations are mainly needed due to the difficulties in determining some material properties experimentally under similar conditions as the ones experienced during injection molding.

An overview of these assumptions is summarized in the following points with a focus on the injection molding of an unfilled semi-crystalline thermoplastic in the commercial software Moldflow® during the filling, packing and cooling analyses [3]:

- Heat sources: the latent heat generated during crystallization is ignored and no heat source term is considered in the energy equation.
- Specific heat capacity: not coupled with crystallization and determined using differential scanning calorimetry for much lower cooling rates than those present during processing.
- Thermal conductivity: defined as a function of temperature without taking into account any pressure dependency.
- Solidification criterion: the use of a no-flow temperature (transition temperature) below which the material exhibits a high viscosity and solidifies with no link between solidification and crystallization.
- Pressure-Volume-Temperature (PVT) data: generated without taking into account the cooling rate or the deformation history of the sample which affects the transition temperature.

1.2.2 Governing Equations

By taking into account the simplifications listed in Section 1.2.1, the governing equations used to simulate the flow in the mold cavity are the three conservation equations. First, the conservation of mass for a fluid is represented as:

$$\frac{\partial \rho}{\partial t} + \nabla \cdot \rho \mathbf{v} = 0 \tag{1.2}$$

where ρ is the polymer density, t is the time and $\mathbf{v}$ is the velocity vector. Second, the conservation of momentum is given by:

$$\rho \frac{\partial \mathbf{v}}{\partial t} + \rho \mathbf{v} \cdot \nabla \mathbf{v} = -\nabla P + \nabla \cdot \tau + \rho g \tag{1.3}$$

where P is the pressure, τ is the viscous stress tensor and g is the gravitational acceleration vector. And, third, the conservation of energy is described by:

$$\rho c_p \left(\frac{\partial T}{\partial t} + \mathbf{v} \cdot \nabla T \right) = \nabla \cdot (k \nabla T) + \tau : \nabla \mathbf{v} + \zeta T \left(\frac{\partial P}{\partial t} + \mathbf{v} \cdot \nabla P \right) \tag{1.4}$$

where T is the temperature, k is the polymer thermal conductivity, c_p is the specific heat capacity of the melt and $\zeta = -\frac{1}{\rho} \frac{\partial \rho}{\partial T}$ is the polymer expansion.

In the case of a 3D analysis, the above-presented equations are typically solved using the finite element method (FEM) with the CAD of the injection molded part being meshed in tetrahedral or hexahedral elements. For a more detailed overview of the injection molding process along with the equations needed to define its simulation refer to Osswald and Menges [1] as well as Kennedy and Zheng [3].

1.3 Polymer Crystallization

1.3.1 Semi-crystalline Thermoplastics

Thermoplastic polymers are divided into amorphous and semi-crystalline polymers. They can mainly be distinguished by the molecular arrangement of their chains as the polymer melt cools down into the solid state. For amorphous polymers, the molecules are randomly oriented and intertwined after cooling. Whereas for semi-crystalline polymers, the molecular structures form ordered regions called crystallites that are surrounded by amorphous regions [1,3]. The coexistence of the two phases provides the polymer with a good balance of stiffness and toughness [19]. The properties of semi-crystalline thermoplastics are thus dependent on the content and orientation of both the crystalline and amorphous phases [3]. Semi-crystalline polymers are widely used in the plastic industry as both commodity plastics (e.g. PE, PP) as well as technical and functional polymers (e.g. PEEK, PVDF, POM) [19,20]. This is mainly due to their versatile nature; where changes in the processing conditions, and thus the thermo-mechanical history, can lead to modifications in the final product's properties e.g. strength, hardness, permeability [21].

The schematic in Figure 1.2 presents the hierarchical arrangement in a semi-crystalline material and the different crystal morphologies observed using polarized optical microscopy in injection molded components. The randomly oriented polymer chain folds into crystal lamella which in turn stacks together to form a lamellar stacking morphology leading to spherulites in the case of quiescent crystallization under no-flow conditions. Whereas in the case of high shear flows, fully extended chains result in extended chain crystals forming parallel to the flow direction along with lamellar crystals forming perpendicular to the flow direction. This leads to the shish-kebab structures characteristic of flow-induced crystallization (FIC) [22].

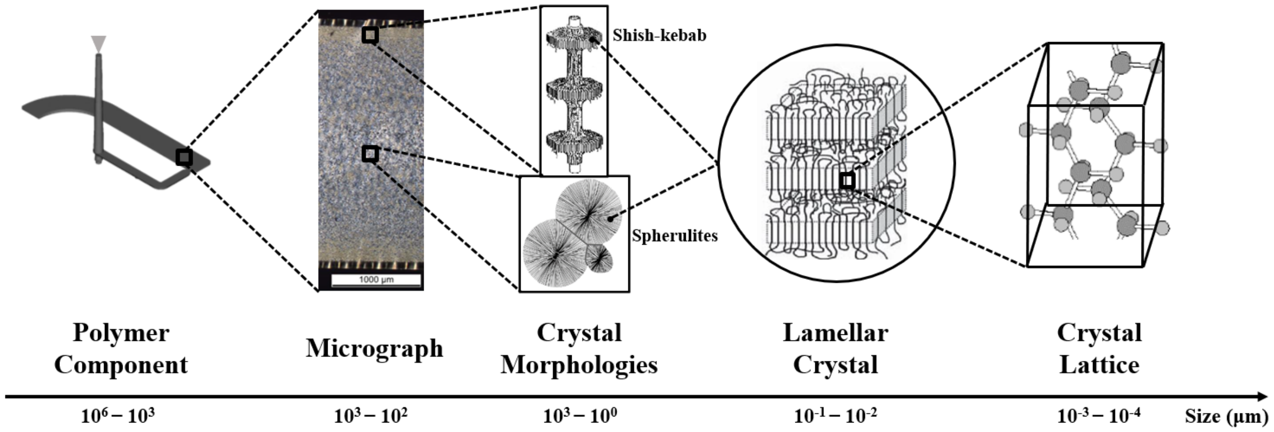

Figure 1.2 – Scheme of the hierarchical structure of an injection molded part with a semi-crystalline material, based on [1].

1.3.2 Crystallization from the Melt

There exist multiple types of crystallization such as crystallization from solution, crystallization by stretching or crystallization from the melt. In this work, the main interest is studying polymer crystallization during the injection molding process and therefore only the crystallization from the melt is considered. This process involves two stages:

1. Nucleation: the formation of active nuclei in the liquid phase acting as starting points for the appearance of crystals [3]. Two types of nucleation can be distinguished [23, 24]:
    - Homogeneous nucleation: caused by heat motion and starts within a few polymer chains or segments (e.g. from the bulk polymer phase).
    - Heterogeneous nucleation: appears on foreign substrates (e.g. nucleating agents, impurities, fillers) or interfaces in multiphase systems.
2. Growth: the growth of the formed nuclei into semi-crystalline morphological structures. These morphologies depend on the thermo-mechanical history experienced by the polymer melt leading to the formation of two distinct nuclei having different growing mechanisms [3, 22]:
    - Spherical nuclei: grow radially in space and form spherical structures known as spherulites, typically seen under no-flow conditions (quiescent crystallization).

- Thread-like nuclei: grow perpendicular to the thread and form the shish-kebab structures, commonly seen under flow conditions with the presence of high strains or shears (FIC crystallization).

The presence of flow, as commonly seen during polymer processing, affects the crystallization process as follows [25]:

- increase of the nucleation density,
- acceleration of the crystallization kinetics,
- changes in semi-crystalline morphological structures,
- increase of the crystallization and melting temperature.

A lot of work has been done in the last few decades to better understand the physics behind polymer crystallization whether under quiescent or flow conditions. An extensive review of the various theories postulated is given by Zhang et al. [26]. The current understanding of this process under flow conditions is that there exists one threshold below which no changes in crystal morphology are observed and above which the nucleation density and growth rate are altered by the presence of flow in addition to a second threshold where thread-like (fibrillar) morphologies start appearing [15, 27]. In the following sections, a brief overview is given of the different experimental and modeling techniques used to study both types of crystallization.

1.3.3 Experimental Methods

In order to obtain a better understanding of the crystallization process of semi-crystalline polymers, various experimental techniques are utilized in the literature. Microscopy is one of the main methods used to gather morphological information on developed crystalline structures in a given sample. Polarized-light optical microscopy is most commonly used for these purposes [28–32] in addition to scanning electron microscopy [28, 33] and atomic force microscopy [15, 34]. Light diffraction experiments are utilized to gain crucial knowledge about the crystallinity and the polymer chains' orientation. The main analysis employed is the wide-angle X-ray diffraction (WAXD) [17, 32, 35]. Additionally, IR spectroscopy is occasionally applied for the same purposes but is not able to discern between different crystalline phases such as WAXD [20].

Differential scanning calorimetry (DSC) measurements are widely performed in the literature to provide quantitative information about the crystallization kinetics which are then used to develop models to describe the process. In addition to DSC, a shearing hot-stage Linkam apparatus is used in combination with optical microscopy to quantify the nucleation and growth steps of crystallization [27, 30, 36, 37]. One major shortcoming of the before-mentioned methods is that they mainly characterize and quantify the crystallization kinetics under quiescent conditions and are not yet fully capable of recreating process-relevant conditions in order to fully model flow-induced crystallization. Nevertheless, there have been some advances in that regard such as the development of fast scanning calorimetry [38] and the use of an extrusion die in combination with optical microscopy to calculate the critical shear rate of activation [39, 40].

1.3.4 Modeling Approaches

To study the crystallization kinetics, whether quiescent or flow-induced, various theories and models have been developed in the literature. These models mainly describe the evolution of the relative crystallinity $\alpha(t)$ as a function of time t and temperature T as a state model expressing $\dot{\alpha}$ as a function of α and T. By definition, the relative crystallinity is the ratio of the crystallized volume X_c to the ultimate crystallizable volume X_∞, such as [25]:

$$\alpha = \frac{X_c}{X_\infty}. \tag{1.5}$$

1.3.4.1 Quiescent Crystallization

The first modeling approach used to describe the kinetics of quiescent crystallization is based on the Kolmogorov-Avrami-Evans (KAE) theory [12, 13, 41], developed for isothermal conditions. Kolmogorov [13] originally used a probabilistic approach to describe the space filling by the formation and growth of spherulites. Independently, Avrami [12] used a geometrical approach to express this growth while taking into account the impingement of the spherulites as they grow and block the growth of the neighboring spherulites. Later on, Evans [41] also developed the same model by analogy to expanding circular waves in water. All three models proved to be identical and are referred to as the KAE theory and is given by:

$$d\alpha = (1 - \alpha) d\Phi \tag{1.6a}$$

$$\alpha(t) = 1 - \exp(-\Phi(t)) \tag{1.6b}$$

where Φ is a fictitious crystallinity obtained by assuming an unrestricted growth $G(t)$ of the spherulites which are represented as spheres. This fictitious crystallinity is defined as follows for a time interval between s and t:

$$\Phi = \frac{4\pi}{3} \int_0^t \dot{N}_q(s) \left[\int_s^t G(u) du \right]^3 ds \tag{1.7}$$

where $\dot{N}_q(t)$ is the rate of nuclei number per unit volume. Under quiescent conditions and in the case of instantaneous nucleation, the nuclei number density $N_q(t) = N_0 H(t)$ where N_0 is the constant nuclei density also known as the number of activated nuclei, $H(t)$ is the Heaviside unit step function such as $H(t) = 0$ for $t < 0$ and $H(t) = 1$ for $t \geq 0$. In turn, $\dot{N}_q(t) = N_0 \delta(t)$ where $\delta(t)$ is the Dirac delta function centered at $t = 0$. By integrating equation 1.7, equation 1.6b is expressed for this considered case as:

$$\alpha(t) = 1 - \exp\left(\frac{-4\pi}{3} N_0 G^3 t^3 \right) \tag{1.8}$$

where the time exponent represents the Avrami index n which is 3 in the case of spherulitic growth and instantaneous nucleation as shown in equation 1.8. In general, the KAE model can be represented using the following expression:

$$\alpha(t) = 1 - \exp(-k_{Avrami} t^n) \tag{1.9}$$

where k_{Avrami} is the Avrami kinetic constant.

According to experimental findings by Koscher and Fulchiron [36], for instantaneous nucleation, the nuclei number density increases when the degree of supercooling $\Delta T = T_m^0 - T$ increases where T_m^0 is the equilibrium melting temperature, such as:

$$\ln N_0(T) = a_N \Delta T + b_N \tag{1.10}$$

where a_N and b_N are experimentally-fitted parameters. More complex temperature dependencies can be found in the literature given by Coppola et al. [42].

As for the temperature dependency of the spherulite growth, the Hoffman-Lauritzen theory is widely used to describe it [43]:

$$G(T) = G_0 \exp\left(-\frac{U^\star}{R(T - T_\infty)} \right) \exp\left(-\frac{K_g}{T(T_m^0 - T)} \right) \tag{1.11}$$

where G_0 and K_g are experimentally-determined parameters, $U^\star$ is the activation energy for segmental jump of polymer molecules with a universal value of 6270 J/mol, R is the gas constant and T_∞ is the temperature at which no molecular displacement happens defined using the glass transition temperature T_g as $T_\infty = T_g - 30$.

Ozawa [44] extended the phenomenological KAE model to adhere to the non-isothermal case such as:

$$\alpha(t) = 1 - \exp\left(-\frac{k_{Ozawa}}{\dot{T}^n}\right) \tag{1.12}$$

where k_{Ozawa} is the Ozawa kinetic constant and $\dot{T}$ is the cooling rate. However, this relation showed some limitations as it applies to a limited range of cooling rates.

Nakamura et al. [45] introduced an isokinetic approach to describe the kinetic constant in the KAE model under non-isothermal conditions:

$$\alpha = 1 - \exp\left[-\left(\int_0^t K(T)dt\right)^n\right] \tag{1.13}$$

where $K(T)$ is the Nakamura kinetics crystallization function and can be related to the Avrami isothermal kinetic constant by $K(T) = k_{Avrami}(T)^{1/n}$. The differential form of the Nakamura model is commonly used in literature such as:

$$\dot{\alpha}(t) = K(T)n(1-\alpha(t))[-\ln(1-\alpha)^{1-\frac{1}{n}}]. \tag{1.14}$$

An alternative approach for the modeling of non-isothermal crystallization is proposed by Schneider et al. [14]. This approach uses a set of four first-order differential equations derived from the KAE model to solve for the relative crystallinity. This is done by differentiating equation 1.7 four times with respect to time as follows:

$$\Phi_0 = \Phi = \frac{4\pi}{3}\left[\int_s^t G(u)du\right]^3 dN_q(s), \tag{1.15a}$$

$$\Phi_1 = \frac{1}{G}\dot{\Phi}_0 = 4\pi\left[\int_s^t G(u)du\right]^2 dN_q(s), \tag{1.15b}$$

$$\Phi_2 = \frac{1}{G}\dot{\Phi}_1 = 8\pi\left[\int_s^t G(u)du\right] dN_q(s), \tag{1.15c}$$

$$\Phi_3 = \frac{1}{G}\dot{\Phi}_2 = 8\pi N_q(t). \tag{1.15d}$$

Therefore, the Schneider rate equations are defined as:

$$\dot{\Phi}_3 = 8\pi \dot{N}_q(t), \tag{1.16a}$$

$$\dot{\Phi}_2 = G\Phi_3, \tag{1.16b}$$

$$\dot{\Phi}_1 = G\Phi_2, \tag{1.16c}$$

$$\dot{\Phi}_0 = G\Phi_1, \tag{1.16d}$$

The Schneider functions Φ_i provide morphological information concerning the formed crystalline structures such as:

- Φ_0: the total volume of the undisturbed spherulites (no impingement) per unit volume,
- Φ_1: the total surface area of the undisturbed spherulites per unit volume,
- Φ_2: 8π times the sum of the radii of the undisturbed spherulites per unit volume,
- Φ_3: 8π times the number of the undisturbed spherulites per unit volume.

The solution of the system of equations 1.16 is Φ_0 which can be written in the form of equation 1.6b to take into account the impingement of the spherulites, such as:

$$\alpha(t) = 1 - exp(-\Phi_0(t)) \tag{1.17a}$$

$$\Phi_0(t) = -\ln(1 - \alpha(t)). \tag{1.17b}$$

1.3.4.2 Flow-induced Crystallization

As already mentioned in Section 1.3.2, the presence of flow greatly affects the crystallization kinetics. This has been observed experimentally, however, the exact physics behind this phenomenon is still not fully understood [15]. Therefore, literature works proposed different approaches to model flow-induced crystallization. These can be clustered in two main categories according to which type of model the work is based on:

- Nakamura's model: the increase of crystallization kinetics is taken into account by multiplying the kinetic function $K(T)$ in equation 1.14 by an enhancement factor depending on the postulated driving force for flow-induced crystallization (stress, strain, shear rate, melting temperature increase). This approach neglects the changes in morphology.

- KAE model and/or Schneider's rate equations: the increase of crystallization kinetics is connected to enhancements in the nucleation rate and/or growth rate of the crystal morphologies as well as the volumetric free energy difference between the molten and crystalline phases used while describing the nucleation rate.

Table 1.1 presents an overview of the literature in the field of modeling the FIC categorized according to the two approaches presented previously in addition to the proposed driving force used to describe the effect of the flow on the crystallization kinetics. These two approaches are not strictly separate as some of the functions used to describe the driving force proposed by the authors using the Nakamura model can be easily used to obtain morphological information using a modified form of the Schneider rate equations. In the following, an example of that is shown, starting first by using an enhancement function derived by Eder et al. [57] followed by one proposed by Tanner et al. [49].

In the presence of flow, the total nuclei number density can be expressed as:

$$N(t) = N_q(t) + N_f(t) \tag{1.18}$$

where N_q is the number of existing nuclei at the beginning of the process equivalent to those present under quiescent conditions with a temperature dependence given in equation 1.10 and N_f is the flow-induced nuclei number density. Eder et al. [57] proposed the following differential equation to represent the flow-induced nucleation:

$$\dot{N}_f + \frac{1}{\lambda_N} N_f = \Upsilon \tag{1.19}$$

where λ_N is a temperature-dependent relaxation time and Υ is a function dependent on flow variables and temperature. This function represents the main driving force that enhances nucleation in the presence of flow. Eder et al. [57] postulated that the shear rate is that driving force and defined this function as:

$$\Upsilon = g_n \left(\frac{\dot{\gamma}}{\dot{\gamma}_n} \right)^2 \tag{1.20}$$

where $\dot{\gamma}$ is the shear rate, $\dot{\gamma}_n$ is the critical shear rate of activation and g_n is a factor. By assuming that each shish-kebab is represented as a cylinder, it is possible to modify the Schneider rate equations to describe the evolution of these crystals in the presence of flow using the enhanced nucleation expression

Table 1.1 – Overview of the literature in the field of modeling the flow-induced crystallization during polymer processing, based on [15].

Crystallization model based on	**Effect of flow on crystallization kinetics using**	**Author(s)**
Nakamura's model [45]	Multiplying factor function of the extra stress tensor	Doufas et al. [46], Zinet [47]
	Multiplying factor function of the strain and the shear rate	Kulkarni et al. [48], Tanner et al. [49], Brahmia [50], Mu et al. [37, 51]
	Melting temperature increase function of stress	Haas and Maxwell [52], Titomanlio et al. [53], Guo and Narh [54]
	Melting temperature increase function of molecular strain	Titomanlio and Lamberti [55], Kim et al. [56], Pantani et al. [27, 34]
	Irreversible thermodynamics based on the standard material formalism	Poitou et al. [16, 17]
KAE model [12, 13, 41], Schneider's rate equations [14] (Nucleation and growth models)	Enhancement of nucleation rate	Eder et al. [57], Zuidema et al. [29], Koscher and Fuchiron [36], Roozermond et al. [35], Kim et al. [58]
	Enhancement of growth rate	van Meerveld et al. [59], Zinet et al. [60], Roozemond et al. [61], Troisi and Arntz [32]
	Enhancement function of the free energy contribution affecting the nucleation rate	Acierno et al. [62], Zheng and Kennedy [63], Zheng et al. [30], Laschet et al. [64], Schrank et al. [65]

given in equation 1.19 such as:

$$\dot{\Phi}_{3,f} + \frac{\Phi_{3,f}}{\lambda_N} = 8\pi \left(\frac{\dot{\gamma}}{\dot{\gamma}_n}\right)^2 g_n, \tag{1.21a}$$

$$\dot{\Phi}_{2,f} + \frac{\Phi_{2,f}}{\lambda_l} = \Phi_{3,f} \left(\frac{\dot{\gamma}}{\dot{\gamma}_n}\right)^2 g_l, \tag{1.21b}$$

$$\dot{\Phi}_{1,f} = G\Phi_{2,f}, \tag{1.21c}$$

$$\dot{\Phi}_{0,f} = G\Phi_{1,f}, \tag{1.21d}$$

where λ_l is the temperature and shish length dependent relaxation time during axial growth and g_l is a factor for the axial growth of the shish. As for the crystal growth G, Eder assumed that it still follows the Hoffman-Lauritzen theory presented in equation 1.11. Additionally, the flow-induced Schneider functions represent the following:

- $\Phi_{0,f}$: the total volume of the undisturbed shish-kebabs (no impingement) per unit volume,
- $\Phi_{1,f}$: the total surface area of the undisturbed shish-kebabs per unit volume,
- $\Phi_{2,f}$: 8π times the total length of the shish per unit volume,
- $\Phi_{3,f}$: 8π times the number of the undisturbed flow-induced nuclei N_f per unit volume.

To take into account impingement and the fact that typically both spherulite and shish-kebab morphologies are present during polymer processing, the relative crystallinity evolution can be represented by including both the quiescent undisturbed volume Φ_0 and that of the flow-induced $\Phi_{0,f}$:

$$\alpha(t) = 1 - exp(-\Phi_0(t) - \Phi_{0,f}(t)) \tag{1.22a}$$

$$\Phi_0(t) + \Phi_{0,f}(t) = -\ln(1 - \alpha(t)). \tag{1.22b}$$

The equation system given by equations 1.21 and 1.22 is presented using the function Υ as defined by Eder et al. [57]. However, this can be easily generalized by using:

$$\dot{\Phi}_{3,f} = 8\pi\dot{N}_f \tag{1.23a}$$

$$\Phi_{3,f} = 8\pi N_f. \tag{1.23b}$$

Equations 1.23a and 1.23b provide a way to couple the work done by the different authors presented in Table 1.1. For example, Tanner et al. [49] proposed a relation connecting the flow-induced nucleation rate $\dot{N}_f$ to both shear rate and shear strain by:

$$\dot{N}_f = A|\dot{\gamma}(t)|^p(\dot{\gamma}t) \tag{1.24}$$

where $|\dot{\gamma}(t)|^p$ describes the effect of the chain relaxation, A and p are material parameters. Tanner's nucleation rate expression can be used in equation 1.23a in order to obtain a modified Schneider equation system such as the one presented in equation 1.21 making it possible to obtain morphological information.

A different approach based on thermodynamics is used by Poitou et al. [17] to describe the flow-induced crystallization in the framework of generalized standard materials. The standard material formalism is commonly used in solid mechanics to describe various coupled phenomena. It necessitates two potentials, a thermodynamic potential and a pseudo-potential, in order to describe the behavior of a material. The first potential helps in quantifying the capability of the material to store energy whereas the second potential quantifies the capability of the material to dissipate energy [17]. In this case, Poitou et al. [17] used the free energy Ψ as the thermodynamic potential, defined as:

$$\Psi(T, \alpha) = \alpha X_\infty \Psi_c(T) + (1 - \alpha X_\infty)\Psi_a(T) \tag{1.25}$$

where Ψ_c and Ψ_a correspond to the free energy of the crystalline and amorphous phases, respectively. By using the standard material formalism, it is therefore possible to fully describe a coupled phenomena such as the flow-induced crystallization since the mechanical parameters are dependent on the degree of crystallinity. The coupling is taken into account by adding up the potential representing the quiescent kinetics given by the Nakamura model [45] and the potential referring to the mechanical constitutive behavior [17]. By assuming that the material is a Newtonian fluid, this mechanical dissipation potential is thus approximated using a simple relation between the strain rate tensor and the viscosity. For more detailed information concerning the derivation of this model, refer to [16,17]. The model is given by:

$$\dot{\alpha}(t) = (1 - \alpha)\left[-\frac{1}{\beta(T)}\frac{\partial \eta}{\partial \alpha}\mathrm{tr}\mathbf{D}^2 + \frac{n}{\chi(T)}\left(-\ln(1-\alpha)\right)^{1-\frac{1}{n}}\right], \tag{1.26}$$

where $\mathbf{D}$ is the strain rate tensor, $\beta(T)$ is a function taking into account the temperature-dependency of the flow-induced crystallization and $\frac{\partial \eta}{\partial \alpha}$ is the viscosity derivative in respect to the relative crystallinity α. $\chi(T)$ is the temperature-dependent kinetic function as defined by Hieber [66]. The first term in equation 1.26 is the contribution of the flow to the relative crystallinity evolution whereas the second term is the original Nakamura model given in equation 1.14 with $\chi(T) = 1/K(T)$.

Table 1.2 – List of the commonly used models to couple the viscosity and the crystallization using a normalized rheological function $\Gamma = \eta/\eta_0$.

Author(s)	**Equation**	**Approach**
Kitano et al. [67], Metzner [68]	$\Gamma = 1/\left(1-\alpha/b_1\right)^{-2}$	Suspension
Ziabicki [69]	$\Gamma = 1/\left(1-\alpha/b_1\right)^{b_2}$	Empirical, based on suspension
Zuidema et al. [29], Doufas et al. [46]	$\Gamma = \exp\left(b_1\alpha + b_2\alpha^{b_3}\right)$	Empirical
Titomanlio et al. [53], Guo and Narh [40]	$\Gamma = 1 + b_1 \exp\left(-b_2/\alpha^{b_3}\right)$	Empirical
Tanner [70]	$\Gamma = 1 + b_1\alpha + b_2\alpha^2$	Empirical, based on suspension
Zheng et al. [30]	$\Gamma = 1 + \left(\alpha/b_1\right)^{b_2} / \left(1-\alpha/b_1\right)^{b_3}$	Empirical

1.3.5 Effect on Other Material Properties

During processing, the development and evolution of the different crystal structures influence other material properties such as viscosity, specific volume, thermal capacity and thermal conductivity. Therefore, in the last two decades, various efforts have been made to develop models that describe the effect of crystallization on these material properties. In the following, some of these models are presented for describing viscosity and specific volume. For a more detailed look into the effect of crystallization on the thermal capacity and the thermal conductivity refer to [3].

1.3.5.1 Viscosity

For semi-crystalline materials, an accurate prediction of the solidification of the material during processing is imperative to achieving precise simulation results. However, as the solidification is mainly due to crystallization in such materials, specifying a single no-flow temperature is highly inaccurate especially since the crystallization is affected by both the thermal and flow history [3]. An alternative way to determine when solidification happens is by using a solidification criterion based on the viscosity. For that, it is then important to couple the viscosity and the relative crystallinity of the material to obtain more realistic results.

As it is difficult to measure the viscosity and the crystallinity simultaneously, separate testing methodologies are typically performed to couple these two phenomena. Rheological measurements are done to describe the viscosity evolution as a function of temperature and shear rate. Whereas, DSC measurements are carried out to obtain the crystallinity evolution with temperature. Special care is taken to assure that these measurements experience the same thermal histories [71]. The experimental data obtained from the previously mentioned methods are used to obtain models describing the viscosity enhancement due to crystallization. These models or coupling functions are mainly based on two different approaches:

- derived from models developed in the field of suspension rheology,
- empirical equations recreating the abrupt increase in viscosity due to crystallization.

Table 1.2 presents some of the commonly used models to couple the viscosity and the crystallization using the following normalized rheological function:

$$\Gamma(\alpha) = \frac{\eta}{\eta_0} \tag{1.27}$$

where η is the melt viscosity and η_0 is the zero-shear-rate viscosity. The list is not comprehensive, refer to [15] and [71] for more details concerning this subject.

1.3.5.2 Specific volume

During polymer processing, the specific volume is mainly affected by the temperature, pressure and flow history of the material which in turn influences the produced part's shrinkage behavior [22]. For semi-crystalline polymers, the specific volume is additionally dependent on the cooling rate and the crystallinity evolution as they affect the shifting of the transition zone. This is represented in Figure 1.3 using a self-produced plot by showing the difference in the specific volume predictions using a cooling rate or crystallization dependent pressure-volume-temperature (PVT) model in comparison to the widely used Tait model. As the cooling rate changes between 1 and 50 °C/min, the modified Tait model predicts different transition zone depending on the cooling rate whereas the Tait model estimates the same specific volume profile for all cooling rates.

Therefore, it is essential to model accurately the specific volume using PVT models that take these dependencies into account. Some efforts have been made in this regard by Luyé et al. [72], Fulchiron et al. [73], Zheng et al. [30] and Zhao et al. [74]. They included the relative crystallinity into the calculation of the specific volume v by assuming a simple mixing rule of the molten and solidified phases' specific volumes, represented respectively as v_m and v_s. This law is written as:

$$v = \alpha v_s + (1 - \alpha) v_m. \tag{1.28}$$

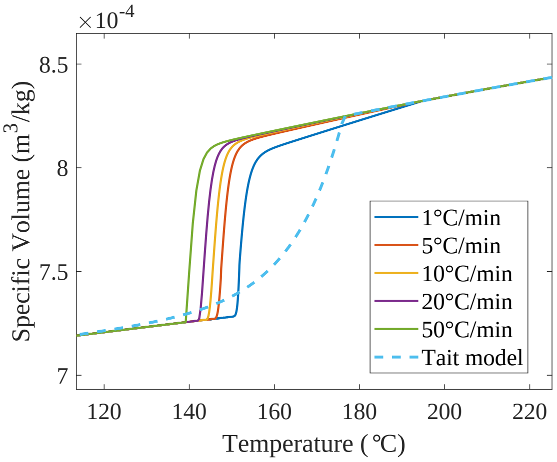

Figure 1.3 – An illustrative example plot of the specific volume as a function of temperature at a fixed pressure using a crystallinity-dependent Tait model for five different cooling rates $\dot{T} = 1, 5, 10, 20, 50$ °C/min (solid lines) in comparison to using the Tait model (dashed line).

The specific volumes v_m and v_s are described using the empirical Tait equation, such as:

$$V_x(T, P) = v_0(T)\left[1 - C\ln\left(1 + \frac{P}{B(T)}\right)\right] \tag{1.29}$$

with $x \in m, s$. In equation 1.29, C is a universal constant equal to 0.0894, $v_0(T)$ is the specific volume at zero gauge pressure and $B(T)$ describes the pressure sensitivity of the studied material. These temperature-dependent functions are defined as follows:

$$v_0(T) = b_{1x} + b_{2x}(T - b_5), \tag{1.30}$$

$$B(T) = b_{3x}\exp\left(-b_{4x}(T - b_5)\right) \tag{1.31}$$

where b_{1x}, b_{2x}, b_{3x}, b_{4x} and b_5 are data-fitted coefficients usually obtained using dilatometry measurements [32, 60, 61].

Another approach to improve the specific volume predictions is to include the cooling rate $\dot{T}$ into the PVT model as well as the transition temperature calculations, as developed by Cook et al. [75], such as:

$$T_t(P, \dot{T}) = b_5 + b_6 P + c\log\left(\frac{\dot{T}}{\dot{T}_0}\right) \tag{1.32}$$

where b_6 and c are material parameters and $\dot{T}_0$ is a low cooling rate for which the polymer maintains an equilibrium state. Other authors such as Wang et al. [76] and Hopmann et al. [77] proposed more complex cooling rate dependencies for the PVT modeling, for more details refer to [76, 77].

1.4 Surrogate Modeling

Currently, in science and engineering, there still exists a large number of physical problems that high performance modern computing is not able to accurately solve despite the advances made in modeling, numerical and discretization techniques [78]. This is mainly due to the high complexity and multi-dimensionality of such physical models [79]. Therefore, in the last couple of decades, there has been a growing interest in surrogate modeling techniques in order to address these challenges. Such methods approximate the response of complex models using a surrogate model also known as a metamodel after being trained with a limited number of input and output results. This makes surrogate models cheaper to run and are thus used instead of the complex model in various fields such as engineering design optimization, uncertainty quantification, sensitivity analysis ...

1.4.1 General Overview

The construction of a surrogate model consists of multiple steps. The basic process can be summarized as follows [80–82]:

1. *Design Variables Choice*: Selection of variables, which presumably have a non-negligible impact on the model output, this choice is usually supported by preliminary experiments, whether physical or numerical experiments.
2. *Design Space Sampling*: Definition of a sampling plan also referred to as design of experiments and evaluation of the respective design points by means of a high-fidelity simulation or actual experiments.
3. *Surrogate Model Generation*: Selection of a type of surrogate model in accordance with the problem at hand and the construction of the model by fitting the data obtained at the chosen points in the design space.
4. *Model Validation*: Checking the accuracy of the generated model according to a predefined statistical criteria, in case of unsatisfactory results, identification of new design points for further model enrichment.
5. *(Optional) Model Updating*: Building an updated surrogate model using additional design points along with the previous ones.
6. *Model Exploitation*: Use of the generated surrogate model for further analyses such as parameter

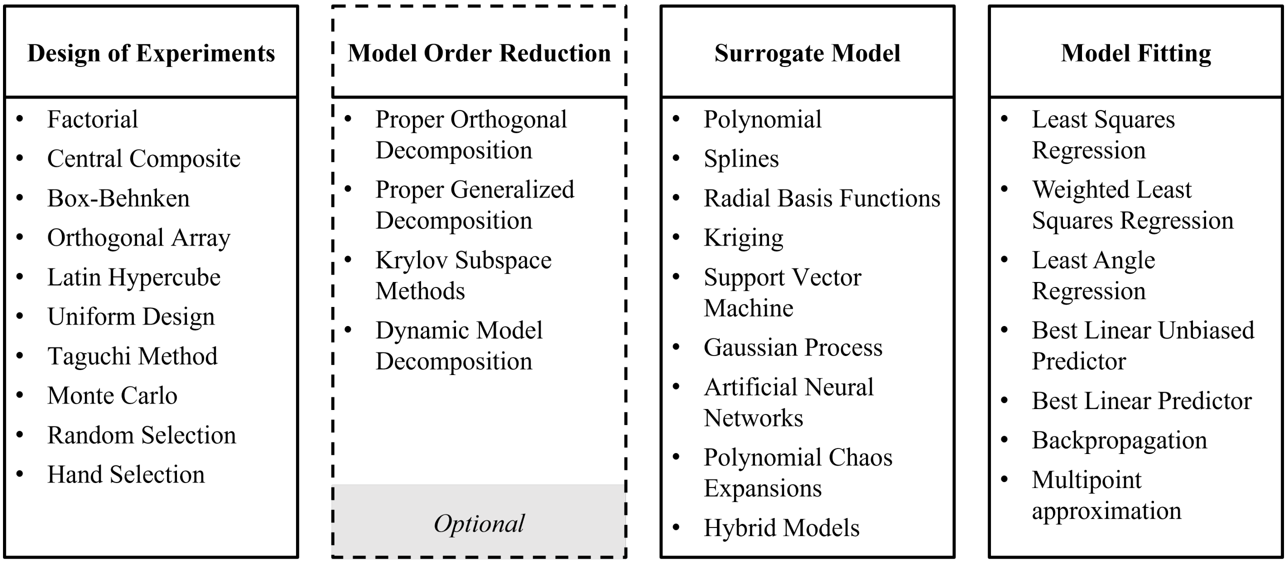

Figure 1.4 – Overview of the most commonly used methods during the generation of a surrogate model [6, 83].

sensitivity analysis, optimizations or uncertainty quantification.

Figure 1.4 provides a more detailed look into the most commonly used techniques to perform the second and third steps in the surrogate model generation process presented above. After defining the design space, an additional optional step is to perform a model order reduction on the output result(s) needing to be approximated by the surrogate model. Following this, the surrogate model is chosen along with the appropriate fitting method. In the following sections, a closer look is taken into each of the four steps shown in Figure 1.4.

1.4.2 Design of Experiments

Design of experiments (DoE) or sampling plan are terms used to represent the physical or computational experiments needed to be run in order to capture the behavior of an underlying system over a limited number of variables [81, 84]. To build a surrogate model of a system, it is crucial to cleverly select the design points in order to cover the complete design space using the least possible number of samples. There exist two main categories of DoEs:

- Classical DoE methods: used typically for physical experiments since these experiments are non-repetitive due to the presence of random error sources (full/fractional factorial, Box-Behnken, central composite...)

- Modern DoE methods: applied to deterministic computer experiments where systematic errors are mostly involved (Taguchi method, Latin hypercube, uniform designs, Monte Carlo...).

There exists a high number of DoE methods present in literature, however, in this thesis, Latin Hypercube sampling and Quasi-Monte Carlo sampling are used and are presented in detail in the following sections. For more information concerning the other DoE techniques, refer to [9, 83, 85].

1.4.2.1 Latin Hypercube Sampling

The Latin hypercube sampling (LHS) technique is widely used in computational applications as it can work with any sample size which gives the user the freedom to choose the number of samples according to the available computational resources [85, 86]. LHS is a space-filling method, as it tries to find a design that fills the design space given a specific number of samples. To demonstrate the technique, let us consider a 2-dimensional design space $\Omega = [0,1]^2$ with variables having uniform probability distribution functions. If the desired number of sample points is, for example, $N = 4$, then the design space is divided into 4^2 equally sized cells. Next, values from 1 through N are placed in each row so that no two columns have an integer repeating, similar to Sudoku [85, 86]. Figure 1.5 shows two of the many possible arrangements. Next, a random integer between 1 and N is selected to specify the N cells in which a sample point is randomly picked. In the examples shown in Figure 1.5, the chosen integer is 2 such as the shaded cells representing the sampling sites.

The Latin square presented in Figure 1.5 generalizes to a Latin hypercube for higher dimensional $(n > 2)$ design spaces. For instance, a design space with $n = p$ design variables requiring N sample points will form N^p hypercubes [86]. It is also worth noting that there can exist some cases, such as diagonal arrangements, for which the chosen sample sites are not optimally positioned and do not fill the design space. One way to eliminate such an arrangement is by introducing additional conditions to check the minimum distance between the design points and selecting the largest one [86].

1.4.2.2 Quasi-Monte Carlo Sampling

Quasi-Monte Carlo (QMC) sampling is the deterministic counterpart of the classical Monte Carlo (MC) sampling method [87]. In classical MC, sample points are randomly selected in the design space for a given interval which can lead to having some regions of the design space unexplored [88].

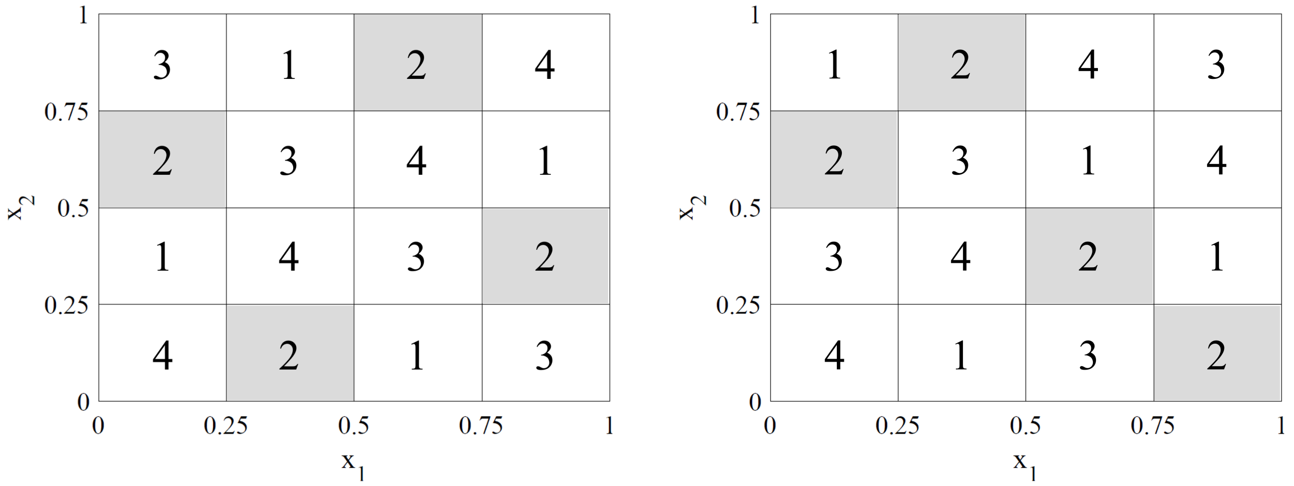

(a) LHS example arrangement 1

(b) LHS example arrangement 2

Figure 1.5 – Latin Hypercube sampling in a 2-dimensional design space $\Omega = [0, 1]^2$ with a set of sampling sites denoted by integers from which the shaded cells are the selected sampling sites.

Therefore, to overcome this shortcoming, QMC methods were developed to provide deterministic sample points with the optimal spread over the design space. These methods are also known as low-discrepancy sequences since they fill the space with some uniformity in order not to leave big gaps [86]. There exist various numbers of such sequences such as the Halton sequence [89], the Niederreiter sequence [90], the Sobol sequence [91]...

Many of the mentioned sequences are based on the van der Corput one, which is the simplest one-dimensional low-discrepancy sequence. One can refer to [92] for a detailed explanation concerning this sequence and its generalizations. For this work, the Sobol sequence is mainly used to obtain quasi-random DoE samples. In this type of sequence, the prime number 2 is used as the base for all the dimensions of the sequence. The first dimension is the van der Corput sequence with a base of 2 and the higher dimensions are permutations of this first dimension [86, 91]. Figure 1.6a shows an example of 1000 sample points obtained using QMC with the Sobol sequencing method in comparison to those gotten using LHS in Figure 1.6b for a 2-dimensional design space $\Omega = [0, 1]^2$ with variables having uniform probability distribution functions.

1.4.3 Model Order Reduction

Model order reduction (MOR) techniques provide a way to reduce the complexity of high-fidelity models by representing them in a reduced form. This allows for a more efficient model evaluation

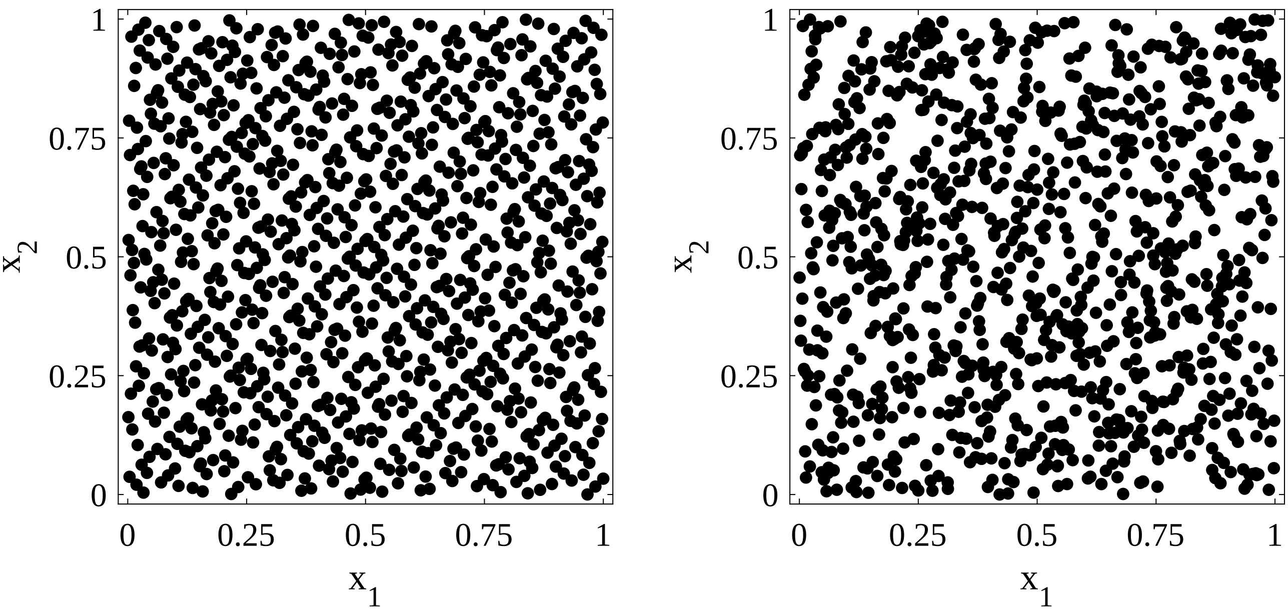

(a) Quasi-Monte Carlo Sampling

(b) Latin Hypercube Sampling

Figure 1.6 – Comparison of 2-dimensional design spaces $\Omega = [0,1]^2$ with 1000 sample points obtained using (a) QMC, (b) LHS.

for offline and online applications. MOR methods work on the discretization of a state equation's dimensionality instead of on its design space which differentiates them from data fitting methods [82].

There exist multiple MOR techniques in the literature such as Proper Orthogonal Decomposition (POD), Proper Generalized Decomposition (PGD), Krylov subspace methods... In the following, the discussion is limited to describing the POD method for the case of a time-dependent problem. For this discussion, let us consider Y to be one model output and $\mathbf{X} = (X_1, \cdots, X_p)$ the set of input parameters defined in the design space D_{X_i} such as:

$$Y = f(\mathbf{X}) = f(X_1, \cdots, X_p) \approx F(X_1, \cdots, X_p) \tag{1.33}$$

where the function $f(\mathbf{X})$ represents the system or simulation output that is being approximated using a surrogate model $F(\mathbf{X})$ and p the parameter space design size. These notations are used to describe the methods presented in the following sections for the case of one output result which can be extended to the multi-output case.

1.4.3.1 Proper Orthogonal Decomposition

The POD technique is one of the most commonly used model order reduction method. It is known by different names such as the Karhumen-Loève (KL) expansion as well as Principle Component Analysis (PCA) and an extension of the Singular Value Decomposition [93]. POD is a mathematical procedure that provides orthonormal basis functions, known as empirical eigenvectors, in order to obtain a simplified representation of a set of data or a state's evolution [82, 94]. These obtained eigenvectors correspond to the highest eigenvalues and they represent the basis functions that are able to describe the main modes or events involved in a certain state evolution [94]. Let $\mathbf{M}$ be a model state variable considered in a specific system. The variable can be represented at specific time steps and for the different nodes present using a matrix $\mathbf{A_M}$ such as:

$$\mathbf{A_M} = \begin{pmatrix} M_1^1 & M_1^2 & \cdots & M_1^{\kappa} \\ M_2^1 & M_2^2 & \cdots & M_2^{\kappa} \\ \vdots & \vdots & \vdots & \vdots \\ M_{\nu}^1 & M_{\nu}^2 & \cdots & M_{\nu}^{\kappa} \end{pmatrix} \tag{1.34}$$

where κ is the number of time steps and ν is the number of nodes. The main objective of the POD technique is to find a set of orthogonal basis functions ϕ_i $(i = 1, \cdots, \kappa)$ able to describe the deviation $\hat{M}_i$ of the model variables from their mean $\bar{M}_i$.

These basis functions can be represented through a linear relation with the deviation of the model variables as follows:

$$\phi = \sum_{i=1}^{\kappa} a_i \hat{M}_i. \tag{1.35}$$

To obtain the POD basis vectors, also known as POD modes, the following eigenproblem needs be solved to obtain a subspace with a low dimension m able to provide a good approximation of the true data:

$$\mathbf{A}\mathbf{A}^T \phi = \lambda_i \phi \tag{1.36}$$

with λ_i as the eigenvalues. The state variable M can be then represented using a linear combination of the calculated POD basis functions with the following relation:

$$M(x,t) = \bar{M} + \sum_{i=1}^{m} \alpha_i(t) \phi_i(x) \tag{1.37}$$

where $\alpha_i(t)$ are the POD coefficients [95]. More in-depth information concerning POD and model order reduction can be found in [82, 93, 95].

The POD model by itself is unable to approximate the state variable at sites not included in the original data set [82]. Therefore, the next step is to generate a surrogate model to predict the POD coefficients. For this, the calculated coefficients are used to train a surrogate model. This is done by first choosing a model to fit the POD parameters such as Kriging, radial basis functions, polynomial functions then use an appropriate fitting method to determine the surrogate model's coefficients. As such, one can obtain a POD-based surrogate model.

1.4.4 Surrogate Modeling Methods

The first approximation methods such as polynomial response surface models and neural networks appeared prior to 1990 and were mainly applied to structural design problems [96]. Later on in the 1990's, interest in such surrogate modeling and approximation techniques increasingly grew. Researchers started investigating additional methods such as higher order response surface models, polynomial models [96]. At the beginning of the 21$^{\text{st}}$ century, alternative surrogate modeling techniques emerged such as Kriging, splines, radial basis functions, support vector machine, polynomial chaos expansions...

Response surface methodology (RSM) represents the high-fidelity model response as:

$$Y = g(\mathbf{X}) + \epsilon \tag{1.38}$$

where ϵ is the normally distributed random error with zero mean and standard deviation [97] and $g(\mathbf{X})$ is a polynomial function used to approximate the response. Typically low-order polynomials are used to express $g(\mathbf{X})$ [83].

Kriging is an interpolation-based method derived from statistical theory [98]. A Kriging surrogate model is defined as a combination of a polynomial part and a random error part such as:

$$Y = g(\mathbf{X}) + Z(\mathbf{X}) \tag{1.39}$$

where $Z(\mathbf{X})$ is a normally distributed Gaussian random process with a zero mean, variance σ^2 and a nonzero covariance [6,83]. The function $g(\mathbf{X})$ is similarly to RSM defined using a polynomial expression of the design variables $\mathbf{X}$.

Radial basis functions (RBF) provide an approximation $F(\mathbf{X})$ for an output response such as:

$$F(\mathbf{X}) = \sum_{i=1}^{p} w_i \varrho(\parallel X - X_i \parallel) \tag{1.40}$$

where w_i is a weight coefficient, ϱ is a nonlinear basis function and $|| \cdot ||$ represents the Euclidean distance [7].

Artificial neural networks (ANN) constitute a special architecture of neurons that are each defined by linear regression models along with a nonlinear transform to approximate Y [83]. They learn the output response through the training process while adjusting their weights until an error threshold is reached [99].

Simpson et al. [83] as well as Wang and Shan [80] provide additional details on the various surrogate modeling methods available in the literature. In the following section, the polynomial chaos expansions are presented more in detail.

1.4.4.1 Polynomial Chaos Expansion

Polynomial chaos expansions (PCE) are surrogate modeling techniques that expand $Y = f(\mathbf{X})$ using a series of multivariate basis functions orthogonal to the probability density function g_{X_i} of an input variable X_i [100]. In general, polynomial chaos expansions can be considered as a special case of KL or PCA since orthogonal polynomial families are used to describe the basis functions instead of eigenvectors. The resulting random model response Y is assumed to have a finite variance and thus belonging to the so-called Hilbert space, allowing for the following spectral representation [101]:

$$Y = \sum_{j=0}^{\infty} c_j \psi_j. \tag{1.41}$$

The random variable Y is an infinite series, where $\{\psi_j\}_{j=0}^{\infty}$ are a set of countable random variables forming the basis of the Hilbert space and $\{c_j\}_{j=0}^{\infty}$ are the coefficients representing the coordinates of Y in this basis [101]. With the assumption that the input variables are independent, an inner product can be defined for each variable X_i with any two functions φ_1, φ_2 such as:

$$\langle \varphi_1, \varphi_2 \rangle_i = \int_{D_{X_i}} \varphi_1(x)\varphi_2(x) g_{X_i}(x) dx. \tag{1.42}$$

When replacing the arbitrary functions in equation 1.42 with orthogonal polynomials $P_k^{(i)}$:

$$\langle P_j^{(i)}, P_k^{(i)} \rangle_i = \int_{D_{X_i}} P_j^{(i)}(x) P_k^{(i)}(x) g_{X_i}(x) dx = a_j^{(i)} \delta_{jk} \tag{1.43}$$

where k is the polynomial degree and δ_{jk} is the Kronecker symbol equal to 1 for $j = k$ and 0 otherwise. As for the term $a_j^{(i)}$, it is the squared norm of $P_j^{(i)}$ and is equal to 1 for orthonormal polynomials:

$$a_j^{(i)} = ||P_j^{(i)}||_i^2 = \langle P_j^{(i)}, P_j^{(i)} \rangle_i. \tag{1.44}$$

The family of orthonormal polynomials $\{\psi_j^{(i)}\}$ is obtained by normalizing the $P_j^{(i)}$ functions :

$$\psi_j^{(i)} = P_j^{(i)} / \sqrt{a_j^{(i)}}, \quad i = 1, 2, \cdots, p. \tag{1.45}$$

Depending on the distribution of the input variables, there exist well-known orthogonal polynomial families. For example, if X_i has a uniform distribution, the corresponding family is the Legendre polynomials or if X_i has a Beta distribution then the Jacobi polynomials constitute the basis functions for PCE [102].

In order to estimate the polynomial chaos coefficients, there exists various intrusive (Galerkin projection) and non-intrusive methods. Popular non-intrusive techniques are error minimization ones which solve a least squares (LS) or least angle regression (LAR) problem [86]. For a more detailed description concerning PCE, the reader is advised to refer to [100–102].

1.4.5 Fitting Techniques

The different methods presented in Sections 1.4.3 and 1.4.4 provide a way to approximate a model's response through various mathematical relations. To be able to use these equations to calculate this approximated response, the parameters or bases need to be determined. This is done by a variety of fitting techniques some of which are listed in Figure 1.4.

A commonly used fitting technique for polynomial functions is the least-squares method with which the needed parameters are obtained by minimizing the difference between the approximated response and the high-fidelity one [97]. Another highly utilized method is back-propagation usually used to fit data for an ANN. Whereas, when generating a model using Kriging, the best linear unbiased predictor is typically used [83].

1.4.6 Some Applications

1.4.6.1 Variance-Based Sensitivity Analysis

A surrogate model can be easily utilized to efficiently perform sensitivity analysis on the chosen design variables. One type of such analyses is variance-based ones which are used to quantify the variance contribution of an input parameter to the unconditional variance of the model output [103]. A commonly utilized method in this field is the Sobol method [104]. An attractive feature of this technique is its ability to not only measure the amount of variance caused by one input but also the interaction of two or more inputs and their contribution to the output. These are known as the Sobol sensitivity indices. The method utilizes approximate Monte Carlo integration to calculate the different indices [105].

The Sobol approach decomposes the function f into terms of increasing dimensionality [103]

$$f(\mathbf{X}) = f_0 + \sum_{i=1}^{p} f_i(X_i) + \sum_{i=1}^{p} \sum_{j=i+1}^{p} f_{ij}(X_i, X_j) + \cdots + f_{1,\cdots,p}(X_1, \cdots, X_p) \tag{1.46}$$

such as each successive term represents the increasing degrees of interactions between the various parameters. The total variance $V(Y)$ can be then defined using the sum of the partial variances through a similar decomposition to equation 1.46 with the assumption that the parameters are mutually orthogonal:

$$V(Y) = \sum_{i=1}^{p} V_i + \sum_{i=1}^{p-1} \sum_{j=i+1}^{p} V_{ij} + \cdots + V_{1,\cdots,p}. \tag{1.47}$$

As such, the Sobol sensitivity indices can be formulated as follows:

$$S_i = \frac{V_i}{V} \tag{1.48}$$

for the first order sensitivity indices and

$$S_{ij} = \frac{V_{ij}}{V} \tag{1.49}$$

for the second order sensitivity indices.

1.4.6.2 Optimization

Many engineering problems revolve around optimization routines whether it is to obtain a better geometrical design for a part or to improve the production of that part by finding the optimal process parameters or to better predict the production process using a simulation with accurate model parameters... Surrogate models provide a means to perform these optimizations in the order of seconds instead of hours or even days. A typical surrogate model based optimization problem can be represented as:

$$\begin{aligned} \min \quad & \tilde{f}(\mathbf{X}) \\ \text{s.t.} \quad & \tilde{m}_i(\mathbf{X}) \leq 0 \quad (i = 1, ..., p) \\ & \mathbf{X} \in [\mathbf{X}_L, \mathbf{X}_U] \end{aligned}$$

where the tilde symbol signifies the surrogate model of a function, $\mathbf{X}_L$ and $\mathbf{X}_U$ are the lower and upper bounds of the design variables, respectively [80].

1.4.6.3 Uncertainty Quantification

In every numerical simulation, there exist uncertainties in the input. These can be anything from dimensional errors, constitutive material properties to parameter uncertainties [86]. Uncertainty quantification (UQ) is the study of how these uncertainties affect the simulation output. To perform such a study, it is necessary to run a high number of simulations while varying the selected quantities of interest (QoI). This step is highly challenging since it is computationally very expensive. To overcome this challenge, surrogate modeling is used to represent the simulation output using the chosen QoI. The generated surrogate model is then used to study the propagation of the input uncertainties to the simulation results using various statistical methods.

1.5 Surrogate Modeling in Injection Molding Simulation

In the last two decades, the use of surrogate models to approximate outputs from the injection molding simulation has been growing steadily especially in the field of process parameter optimization to enhance product quality and molding efficiency. Gao and Wang [5] employed a Kriging approximation model along with an adaptive optimization technique to minimize the warpage in produced parts by varying process parameters such as the mold and melt temperature, injection time as well as the holding pressure and time. Similar works were performed by Chen et al. [6], Wang et al. [106] and Kang et al. [107]. Others used radial basis function [2, 7, 108], artificial neural networks [8, 10], Gaussian process [109] as surrogate modeling technique to optimize process parameters for controlling shrinkage and warpage in the final part. Additional applications for surrogate models seen in the literature were used for the optimization of cycle time [108] and part weight [110].

All of the above-mentioned publications use a surrogate model to perform an optimization to determine optimal process parameters. However, another interesting utilization of surrogate modeling in injection molding was recently published by Ivan et al. [11] where the surrogate model is used to identify two fiber orientation model parameters. The authors used experimental fiber orientation data obtained by micro-computed tomography to calibrate the fiber orientation model defined in their injection molding simulation. This was done by generating an ANN-based surrogate model representing the fiber orientation evolution result while varying the two model parameters using a full factorial design space.

Table 1.3 provides an overview of some of the literature available in the field of surrogate modeling in injection molding simulation. More comprehensive reviews can be found in [8,9].

Table 1.3 – Overview of the literature in the field of surrogate modeling based optimization in injection molding simulation.

Author(s)	**DoE Method**	**Surrogate Modeling Method**	**Optimization Objective**	**Design Variables**
Gao and Wang [5]	Optimal midpoint Latin Hypercube	Kriging	Minimize warpage	Mold and melt temperatures, injection and packing times, packing pressure
Chen et al. [6]	Latin Hypercube	Kriging	Minimize deflection along length direction and the maximum injection pressure	Mold and melt temperatures, packing time, packing pressure
Li et al. [7]	Latin Hypercube	RBF	Minimize shrinkage	Packing and cooling times, packing pressure profile
Cheng et al. [8]	Adaptive DoE	ANN	Minimize shrinkage, cycle time, runner volume	Runner diameters, packing and cooling times, packing pressure
Villarreal-Marroquin et al. [110]	Central composite, maximin, Latin Hypercube	Linear Regression, Gaussian Process	Minimize shrinkage and part weight	Mold temperature, packing time
Shi et al. [10]	Latin Hypercube	ANN	Minimize warpage	Mold and melt temperatures, injection, packing and cooling times, packing pressure
Xu and Yang [111]	Taguchi	ANN	Minimize shrinkage, part weight, flash	Mold and melt temperatures, injection, packing and cooling times, packing pressure
Wang et al. [106]	Adaptive DoE	Kriging	Minimize warpage and optimize gate design	Mold temperature, ram speed, packing time and pressure
Kang et al. [107]	Optimal Latin Hypercube	Kriging	Minimize warpage	12 process settings
Kitayama et al. [108]	Latin Hypercube	RBF	Minimize warpage	Cooling temperature, injection, packing and cooling times, packing pressure
Feng and Zhou [2]	Orthogonal Array Latin Hypercube	ANN-RBF	Minimize warpage, shrinkage and weldline	Mold and melt temperatures, injection, packing and cooling times, packing pressure
Mukras et al. [112]	Central composite	Kriging	Minimize warpage and shrinkage	Mold and melt temperatures, injection, packing and cooling times, packing pressure, injection velocity
Ivan et al. [11]	Full factorial	ANN	Minimize fiber orientation distribution prediction error	Two fiber orientation model parameters

1.6 Summary and Thesis Structure

As already stated in Section 1.2, injection molding simulation provides a cost-efficient means to design and improve part quality before producing a mold as well as to identify optimal process settings for the production. However, to be able to achieve that, simulations have to be highly accurate and include less and less approximations. In the case of semi-crystalline thermoplastics, this means taking into account the complex crystallization process taking place during the processing of the material along with its effect on other properties such as viscosity and specific volume. Additionally, in order to improve the overall fill predictions as well as the warpage and shrinkage estimations, the solidification criterion needs to be coupled to the crystallization instead of using a constant no-flow temperature value to determine solidification. Nevertheless, as seen in Section 1.3, the crystallization process under flow conditions is complex and the physics behind it is still not yet fully understood making this problem not straightforward to solve. Also, most of the available models are phenomenological ones with a high number of parameters that are difficult to determine experimentally due to the inability of recreating the extreme conditions experienced during the injection molding process using current experimental devices. One way to overcome this drawback is by using a surrogate model to represent a simulation output which can be measured experimentally on the injection molding machine and using it to identify the model parameters such as Ivan et al. [11] did for the fiber orientation model parameters.

Therefore, in this thesis, the main aim is to implement a crystallization model into a 3D injection simulation routine while taking into consideration the effect of crystallization on the viscosity, PVT and solidification models. In order to identify the experimentally-challenging-to-determine parameters, surrogate models are generated to represent the pressure results obtained by the simulation and to perform a calibration using experimental pressure signal measurements obtained during injection molding trials.

To reach this goal, the theory and the current state of the art in the field of injection molding, polymer crystallization and surrogate modeling were first presented in this chapter. Chapter 1 finished off by introducing some works from the literature that utilized surrogate modeling to represent injection molding simulation results similar to what will be presented in this work.

Following this, the material characterization along with the performed injection molding trials are described in Chapter 2. Additionally, in this chapter, some of the experimental pressure signals are analyzed for the different geometries considered in this thesis as well as some micrographs produced to observe the crytalline morphology along the thickness of the produced parts.

In Chapter 3, a feasibility study is performed to test the use of surrogate modeling for the purpose of calibrating some modeling parameters in the injection molding simulation. This study compares three different surrogate modeling approaches and tests the effect of the number of training simulations on the accuracy of the predicted pressure results.

And, finally, in Chapter 4, the implementation of a thermo-mechanical based crystallization model is described along with crystallization-dependent viscosity, PVT and solidification models in Moldflow® to simulate the injection molding of an unreinforced thermoplastic material. Five modeling parameters are identified using three generated surrogate models by a multi-objective optimization routine. The simulation results using the calibrated models are then analyzed for different processing conditions and mold geometries.

Chapter 2

Material Characterization and Injection Molding Trials

Content

2.1 Material Description

The polymer material used in this work is an industrial grade of an unreinforced polyoxymethylene (POM) homopolymer $(—CH_2—\mathrm{O}—)_n$ in its granular form with a density of 1.42 g/cm^3. The polymer is also known as polyacetal and is an engineering semi-crytalline thermoplastic material widely used in the automotive industry due to its high stiffness, low friction and excellent anti-wear properties [21, 113]. Additionally, in comparison to other semi-crystalline polymers, POM presents with a high degree of crystallinity around 75 to 85 % [21, 114].

2.2 Differential Scanning Calorimetry

2.2.1 Technique Overview

Differential scanning calorimetry (DSC) is a thermal analysis technique used to measure a thermophysical property of a material as a function of temperature [115]. A studied sample along with a reference are subjected to a predetermined temperature profile during which the difference in heat input between the samples is measured [116]. From these measurements, various physical characteristics of the polymer can be quantified, such as the melting enthalpy and the melting temperature... Additionally, the measured enthalpy changes can be utilized to evaluate the relative crystallinity evolution as a function of temperature and time then crystallization kinetics.

2.2.2 Experimental Set-up

The DSC measurements are performed using a *TA Instruments, Inc. DSC Q1000* machine with nitrogen as purge gas with a flow rate of 50 mL/min. The granular form of POM is used for the experiments. The prepared samples are encapsulated in Aluminum pans and lids after being weighed. Ten runs are performed with five different applied cooling rates (1, 3, 5, 10, 40 °C/min) as summarized in Table 2.1. As can be seen in Table 2.1, the sample weights vary for the different cooling rates. This is done as a compromise between the heat flux measurement sensitivity and the low temperature gradient in the samples. Before starting the measurement runs, the DSC machine is calibrated using an Indium sample having a weight of 10.36 mg. In total, three calibration runs are performed:

1. at 1 °C/min for the measurement run with a cooling rate of 1 °C/min,

2. at 10 °C/min for the measurement runs with cooling rates of 3, 5, 10 °C/min,
3. at 40 °C/min for the measurement run with a cooling rate of 40 °C/min.

To set-up the different runs, the following steps are followed:

1. Equilibrate at 25 °C.
2. Isothermal for 2 min.
3. Ramp 10 °C/min to 220 °C.
4. Isothermal for 2 min.
5. Ramp x °C/min to 25 °C with x = 1, 3, 5, 10, 40 °C/min.

Table 2.1 – Overview of the DSC measurement runs and the studied samples' weight.

Run	**Cooling rate** $\dot{T}$ (°C/min)	**Sample weight** m (mg)
1	1	20.67
2		20.74
3	3	10.34
4		10.93
5	5	10.99
6		9.38
7	10	5.06
8		5.93
9	40	3.79
10		3.69

2.2.3 Results

The measured heat flows of the DSC runs summarized in Table 2.1 are analyzed in order to quantify important physical and kinetic characteristics of the crystallization of the studied POM material. Figure 2.1 shows the DSC thermograms that were obtained for the five different cooling rates. The main focus of the performed DSC experiments is to study the crystallization of the polymer and determine the evolution of the crystallinity as a function of time and temperature. Therefore, Figure 2.2 presents the crystallization peaks for the different cooling rates evaluated. It can be seen that as the cooling rate increases the peak and area underneath it increase while shifting to lower temperatures.

From the peaks shown in Figure 2.2, it is possible to determine the crystallization temperature (T_c), the crystallization onset temperature ($T_{c,onset}$) and the crystallization enthalpy (ΔH_c). Additionally,

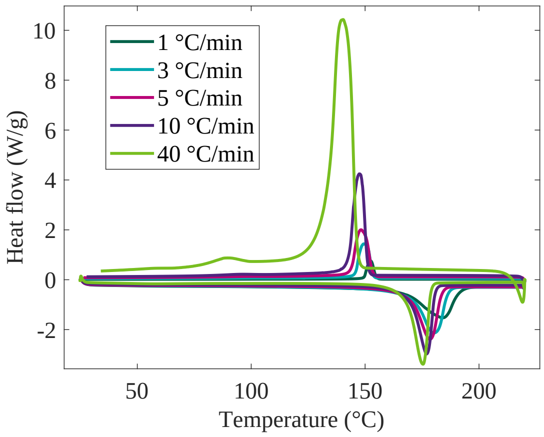

Figure 2.1 – DSC thermograms using five different cooling rates.

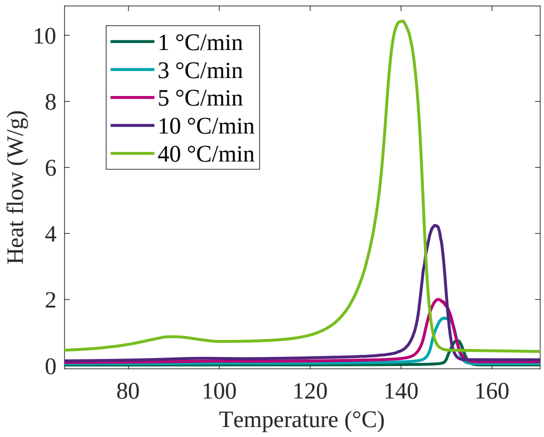

Figure 2.2 – Crystallization peaks of the different DSC measurements.

from the heating cycles of the DSC measurements, the melting temperature (T_m) of the material is determined. Table 2.2 summarizes these quantities obtained from the DSC data. In practice, the crystallization onset temperature depends linearly to the logarithm of its corresponding cooling rate. Therefore, in Figure 2.3, the mean onset temperature of each studied cooling rate ($\dot{T}$) is plotted as a function of $ln(\dot{T})$. However, as can be seen in this figure, the Linear fit 1 used to fit all five data points is not optimal as that of Linear fit 2 which fits only the first four points. This shows the possibility of having inaccurate DSC results especially with the 40 °C/min cooling rate run. Therefore, to determine the crystallization temperature and enthalpy of the studied POM material, Runs 9 and 10 are not taken into consideration as they showed the previously described deviation. Whereas for the determination of the melting temperature, all runs are considered as the heating rate was constant at 10 °C/min for all of the performed runs.

To get the relative crystallinity evolution from the DSC runs, it is imperative to determine an accurate baseline from which the area under the crystallization peak is calculated. This is done using a MATLAB R2019b code with an example illustration presented in Figure 2.4. After running the MATLAB script, the user is asked to specify four points; two before and two after the crystallization peak (turquoise crosses in Figures 2.4a and 2.4b). These points are used to fit two different lines before and after the peak (pink dotted lines). The user is then asked to specify the start and end of the peak (purple circles). In between these two points, a first approximation of the relative crystallinity is calculated and used to correct the purple baseline by the turquoise one in Figure 2.4 below the

Table 2.2 – Overview of the material characteristics of the studied POM determined using the DSC measurements.

Run	$\dot{T}$ **(°C/min)**	$T_{c,onset}$ (°C)	T_c (°C)	T_m (°C)	ΔH_c **(J/g)**
1	1	154.1	152.3	184.0	158.0
2		154.1	152.7	183.3	152.6
3	3	152.6	149.8	180.9	152.1
4		152.2	149.5	180.3	155.9
5	5	151.7	148.2	178.4	155.9
6		151.8	148.9	177.8	158.4
7	10	149.8	147.4	176.9	153.5
8		149.9	146.9	176.9	156.4
9	40	144.0	139.7	174.9	164.8
10		144.1	140.3	175.4	165.6

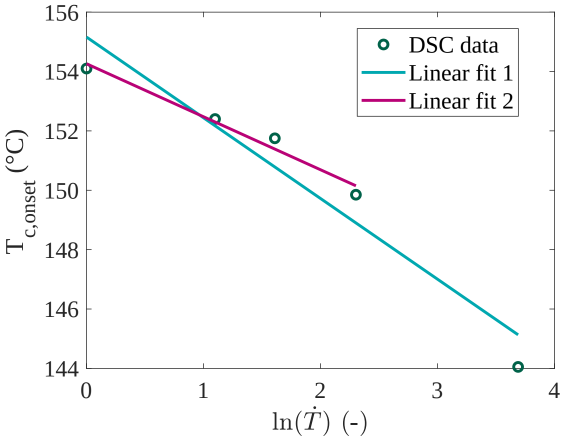

Figure 2.3 – The dependency of the crystallization onset temperature $T_{c,onset}$ as a function of the different cooling rates $\dot{T}$ along with two linear fits, Linear fit 1: data from $\dot{T} = 1, 3, 5, 10, 40$ °C/min, Linear fit 2: data from $\dot{T} = 1, 3, 5, 10$ °C/min.

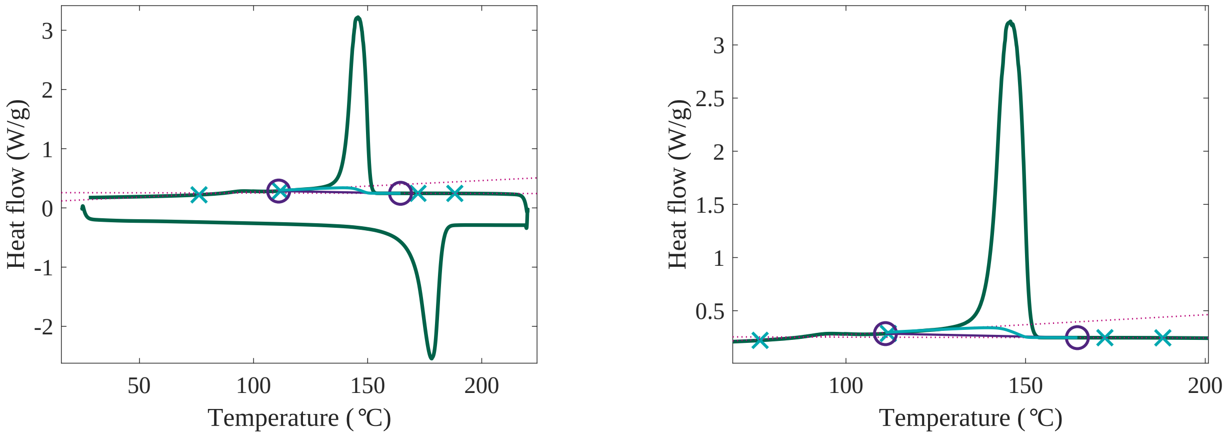

(a) DSC thermogram for a cooling rate of 10 °C/min (Run 8) after running the MATLAB script.

(b) Closer look at the crystallization peak and the baseline determination technique.

Figure 2.4 – DSC thermogram obtained for *POM* using a cooling rate of 10 °C/min showing the 4-points baseline determination technique used to calculate the relative crystallinity evolution.

crystallization peak.

To compute the relative crystallinity evolution for the different cooling rates, one run is chosen to represent each cooling rate since the error between the different runs at the same cooling rate was considered negligible. The relative crystallinity α is computed using the corrected baseline by:

$$\alpha(t \text{ or } T) = \frac{\text{Area below the curve at } t \text{ or } T}{\text{Total area below the curve}}. \tag{2.1}$$

Figures 2.5 and 2.6 show the relative crystallinity evolution for the performed DSC measurements versus temperature and time, respectively. These α results are used in Chapter 4 to determine some parameters to describe the quiescent crystallization kinetics of POM.

2.3 Dynamic Temperature Ramp Tests

2.3.1 Technique Overview

Dynamic temperature ramp tests are rheological measurements used to study the behavior of a viscoelastic material undergoing a temperature change. A constant strain and frequency are specified and the material's response is measured in order to determine its temperature dependence under these conditions.

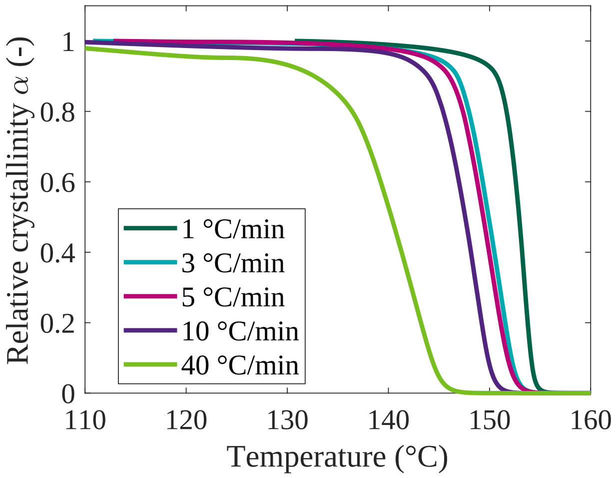

Figure 2.5 – The calculated relative crystallinity α versus temperature for the five cooling rates used in the DSC measurements.

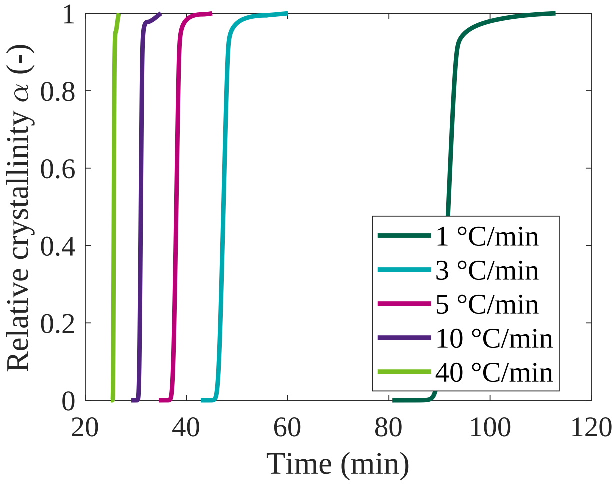

Figure 2.6 – The calculated relative crystallinity α versus time for the five cooling rates used in the DSC measurements.

2.3.2 Experimental Set-up

The dynamic temperature ramp tests are performed using an *ARES* rheometer from *TA Instruments, Inc.* with a plate-plate geometry. Two ramp tests are carried out one with a constant frequency of 1 rad/s and a 0.3 % strain and another with a frequency of 3 rad/s and a 0.03 % strain. The heating/cooling rate used is 3 °C/min. To set-up the test, the following steps are followed:

1. Heat up the apparatus to 210 °C.
2. Set the zero gap between the plates.
3. Open the furnace, increase the gap and place the *POM* granules on the lower plate.
4. Reheat the apparatus.
5. Decrease the gap to 0.7 mm and clean-up in case of polymer overflow.
6. Run the test using the software interface.

2.3.3 Results

Figure 2.7 presents the results of the dynamic temperature ramp tests described in the previous section. By observing the two curves, it is apparent that as the samples cool down from 210 °C until the onset of crystallization their viscosity gradually increases. Whereas, after the start of crystallization, a singularity appears and the viscosity increases more than two orders of magnitudes between 152

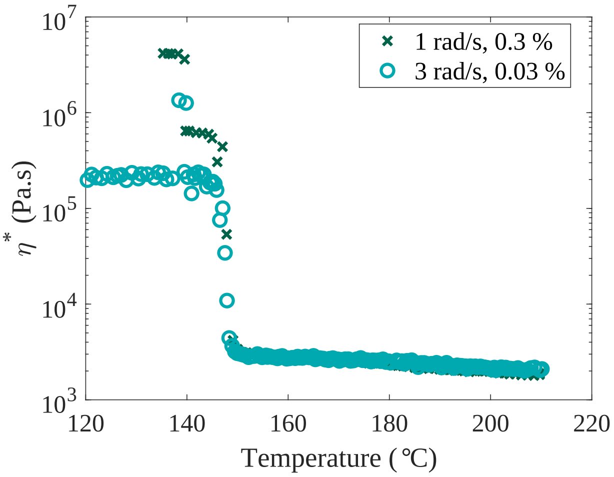

Figure 2.7 – The complex viscosity measured during two dynamic temperature ramp tests as a function of temperature under constant frequency specified in rad/s and constant strain given in %.

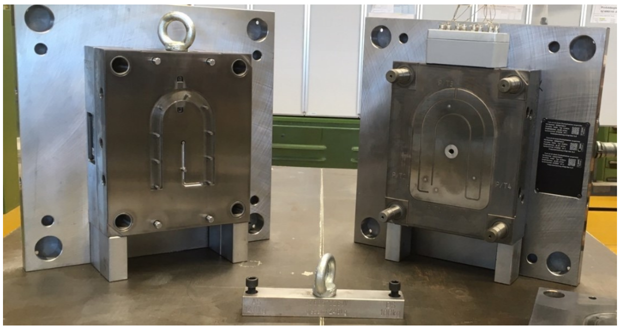

Figure 2.8 – The mold produced to carry out the injection molding trials.

°C and 147 °C. Since these measurements were performed with a cooling rate of 3 °C/min, the crystallization onset temperature can be deduced from the DSC measurements done at this cooling rate and as summarized in Table 2.2, this temperature is around 152.4 °C. These rheological data are used in Chapter 4 to identify the parameters of the viscosity model utilized in the simulation.

2.4 Injection Molding Experiments

2.4.1 Mold Description

A simple mold geometry is used to perform injection molding trials to obtain experimental data that are needed to calibrate model parameters in the injection molding simulation presented in the next chapters. The mold is designed to fulfill the following requirements:

- a long curved channel with the possibility of producing short shots,
- two different mold thicknesses (3 mm & 1.5 mm) and lengths.

To obtain the final design, numerical DoEs are carried out in Moldflow® where results such as the freezing time of the gate and the pressure at multiple locations are compared and deemed acceptable for the presented design. The produced mold is shown in Figure 2.8 whereas Figure 2.9 shows a sketch

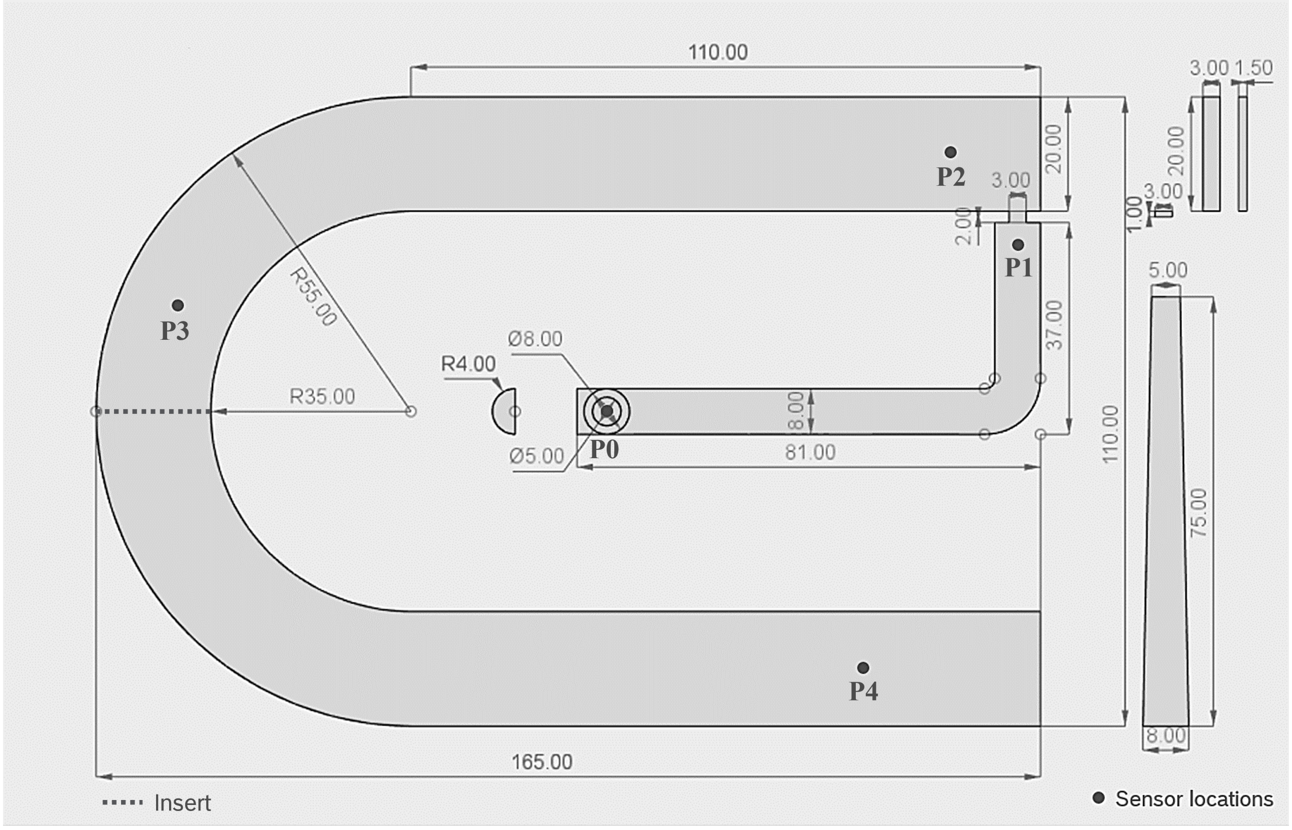

Figure 2.9 – Sketch of the injection-molded part including some characteristic dimensions in mm and the location of the three pressure and temperature combination sensors (p-T-sensors) as well as the insert's location.

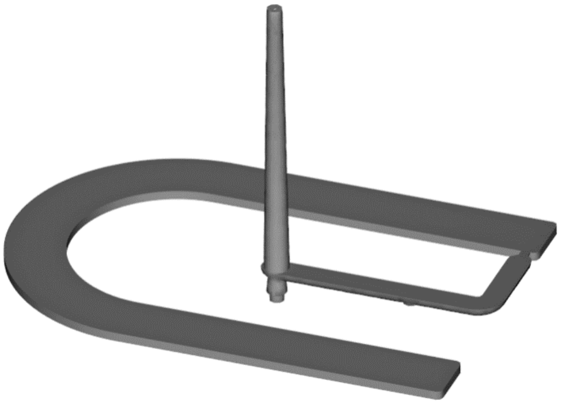

Figure 2.10 – 3D-view of the full length 3 mm thick part.

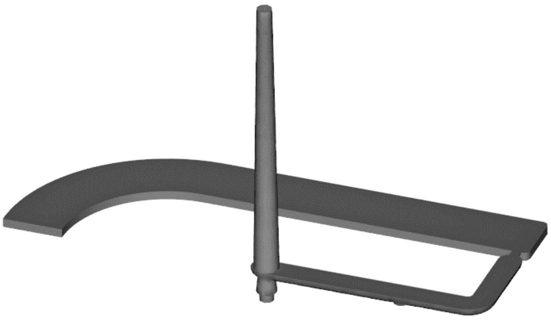

Figure 2.11 – 3D-view of the half length 3 mm thick part.

of it with the design dimensions. In order to meet the requirements listed above, two mold cavities are produced; one with a 3 mm thickness and another with 1.5 mm. Additionally, an insert is produced in order to produce parts with half of the channel's length. The insert's position is represented in Figure 2.9 by the dotted gray line. As for the gray circles in Figure 2.9, they represent the four p-T-sensors used to measure the pressure and temperature signals during the injection molding process. A 3D-view of the 3 mm thick parts that can be produced by the presented mold are presented in Figures 2.10 and 2.11, showing the full length geometry and the half length one, respectively.

2.4.2 Filling and Packing Studies

Before starting the official experimental runs, filling and packing studies are performed on the four different geometries of the produced mold. A filling study is done to determine the shot volume for each geometry by trying to fill the cavity up to 99% without applying any holding pressure. Whereas a packing study, it is used to find the appropriate holding time by specifying a suitable packing pressure and varying the holding time until the weight of the part becomes constant indicating the freezing of the gate.

For this work, the studies are made on an electrical injection molding machine (ENGEL E-Motion 440/220 T) with a material melt temperature of 220 °C. For the filling studies, a mold temperature of 80 °C is specified and for the packing studies the mold temperature is set at 110 °C and the holding pressure at 80 MPa. A summary of the determined values is given in Table 2.3. One important thing

Table 2.3 – Determined shot volumes and holding times from the performed filling and packing studies.

Geometry (abbrev.)	**Shot Volume** (cm^3)	**Holding time** (s)
Full length, 3 mm thick (FL3)	42.0	16
Half length, 3 mm thick (HL3)	28.3	16
Full length, 1.5 mm thick (FL15)	-	10
Half length, 1.5 mm thick (HL15)	26.8	10

to note is that for the full length part with a 1.5 mm thickness, it is not possible to fill the cavity completely with the studied POM material under the recommended processing conditions. Therefore, for this geometry a shot volume of 32 cm^3 is used for the trials but it does not represent the cavity's volume.

2.4.3 Design of Experiments

The same electrical injection molding machine is used to run the experiments used in this work. For all the performed runs, a melt temperature of 220 °C is chosen and the switch-over condition is set by a volume of 10 cm^3. The mold temperature, the injection velocity and the holding pressure are varied in these runs. The upper and lower bounds of these process settings are different for the four available mold geometries. This is due to the geometrical changes affecting the injection pressure and solidification of the material. Table 2.4 summarizes the bounds of these variables. A design of experiments (DoE) is defined for each geometry where the process settings are varied between their upper and lower bounds as well as the middle values. These DoE are presented in Tables 2.5 to 2.8. Fewer runs are performed for the 3 mm full length part due to the small injection velocity range (5 to 15 cm^3/s) for which the injection process can happen without crossing the machine's maximum pressure limit of 240 MPa.

2.4.4 Pressure Signals

As mentioned in Section 2.4.1, pressure and temperature sensors are located at four different positions in the mold. In this work, the main focus is on the pressure signal results measuring the pressure in the cavity before the gate (P1), after the gate (P2), before half the length of the channel (P3) and near the end of the channel (P4). Figures 2.12, 2.13 and 2.14 show some example pressure

Table 2.4 – The upper and lower bounds of the variable process settings used in the injection molding trials.

Process Settings	**Lower Bound**				**Upper Bound**			
	FL3	HL3	FL15	HL15	FL3	HL3	FL15	HL15
Injection Velocity, V_{inj} (cm^3/s)	5	10	10	10	15	50	50	50
Mold Temperature, T_{mold} (°C)	80	80	80	80	110	110	110	110
Holding Pressure, P_{hold} (MPa)	80	20	50	50	110	80	110	110

Table 2.5 – DoE of the injection molding experiments for the full length 3 mm thick part.

DoE	T_{mold} (°C)	V_{inj} (cm^3/s)	P_{hold} (MPa)
S1	80	5	80
S2	80	15	110
S3	95	5	80
S4	95	15	110
S5	110	5	80
S6	110	15	110

Table 2.6 – DoE of the injection molding experiments for the half length 3 mm thick part.

DoE	T_{mold} (°C)	V_{inj} (cm^3/s)	P_{hold} (MPa)
V1	80	10	20
V2	80	30	20
V3	80	50	20
V4	80	10	50
V5	80	30	50
V6	80	50	50
V7	80	10	80
V8	80	30	80
V9	80	50	80
V10	95	10	20
V11	95	30	20
V12	95	50	20
V13	95	10	50
V14	95	30	50
V15	95	50	50
V16	95	10	80
V17	95	30	80
V18	95	50	80
V19	110	10	20
V20	110	30	20
V21	110	50	20
V22	110	10	50
V23	110	30	50
V24	110	50	50
V25	110	10	80
V26	110	30	80
V27	110	50	80

Table 2.7 – DoE of the injection molding experiments for the full length 1.5 mm thick part.

DoE	T_{mold} (°C)	V_{inj} (cm^3/s)	P_{hold} (MPa)
W1	80	10	50
W2	80	30	50
W3	80	50	50
W4	80	10	80
W5	80	30	80
W6	80	50	80
W7	80	10	110
W8	80	30	110
W9	80	50	110
W10	95	10	50
W11	95	30	50
W12	95	50	50
W13	95	10	80
W14	95	30	80
W15	95	50	80
W16	95	10	110
W17	95	30	110
W18	95	50	110
W19	110	10	50
W20	110	30	50
W21	110	50	50
W22	110	10	80
W23	110	30	80
W24	110	50	80
W25	110	10	110
W26	110	30	110
W27	110	50	110

Table 2.8 – DoE of the injection molding experiments for the half length 1.5 mm thick part.

DoE	T_{mold} (°C)	V_{inj} (cm^3/s)	P_{hold} (MPa)
T1	80	10	50
T2	80	20	50
T3	80	30	50
T4	80	10	80
T5	80	20	80
T6	80	30	80
T7	80	10	110
T8	80	20	110
T9	80	30	110
T10	95	10	50
T11	95	30	50
T12	95	50	50
T13	95	10	80
T14	95	30	80
T15	95	50	80
T16	95	10	110
T17	95	30	110
T18	95	50	110
T19	110	10	50
T20	110	30	50
T21	110	50	50
T22	110	10	80
T23	110	30	80
T24	110	50	80
T25	110	10	110
T26	110	30	110
T27	110	50	110

signals measured during the injection molding trials using the four different geometries. By observing these plots, one can distinguish four different phases taking place during the injection molding process by some characteristic pressure responses:

1. Velocity-controlled filling phase: the pressure increases linearly until the switch-over condition is reached.
2. Pressure-controlled filling phase: a sudden pressure drop due to the usually smaller specified holding pressure than the one experienced during the velocity-controlled filling phase.
3. Packing phase: a gradual increase of pressure as the packing starts, followed by a constant pressure observed before the gate whereas after the gate a gradual decrease is observed as the material solidifies.
4. End of packing phase: a sudden decrease in pressure before the gate due to a partially solidified material followed by a gradual decrease to reach zero pressure as seen also after the gate.

Figures 2.12a and 2.12b show two example pressure signals measured during the injection of the full length 3 mm thick cavity under the conditions S3 and S6 (refer to Table 2.5), respectively. It is apparent that the low injection velocity of 5 cm^3/s for the S3 run presented in Figure 2.12a led to a long part filling time of around 9 s. Additionally, for the S3 run, the pressure plateau seen after the switch-over highlights that the part was not fully filled before switching to the pressure-controlled phase and therefore the holding pressure is first used to complete the filling and afterward for the packing. This behavior is not observed in the S6 run presented in Figure 2.12b where the injection velocity is higher at 15 cm^3/s and the filling is nearly finished before switching over. In both examples, there is an expected 20 MPa pressure drop at P1 from the set holding pressure.

Figure 2.13 shows four representative results of the pressure signals observed during the injection of the half length 3 mm thick part. Figure 2.13a presents the pressure signals of the V1 run (refer to Table 2.6) for which the part shorted e.g. not filled fully. The resultant parts are presented in Figure 2.15a as well as another example of a short shot produced using the V11 process settings in Figure 2.15b. These short shots are due to the early freezing of the gate which takes place after the switch-over. The low holding pressure of 20 MPa which is applied after the switch-over to finish the filling of the part is not sufficient to produce a complete part. Figure 2.13b shows the pressure signals for the V9 run which produced a full part. An interesting phenomenon is observed in the presented V9

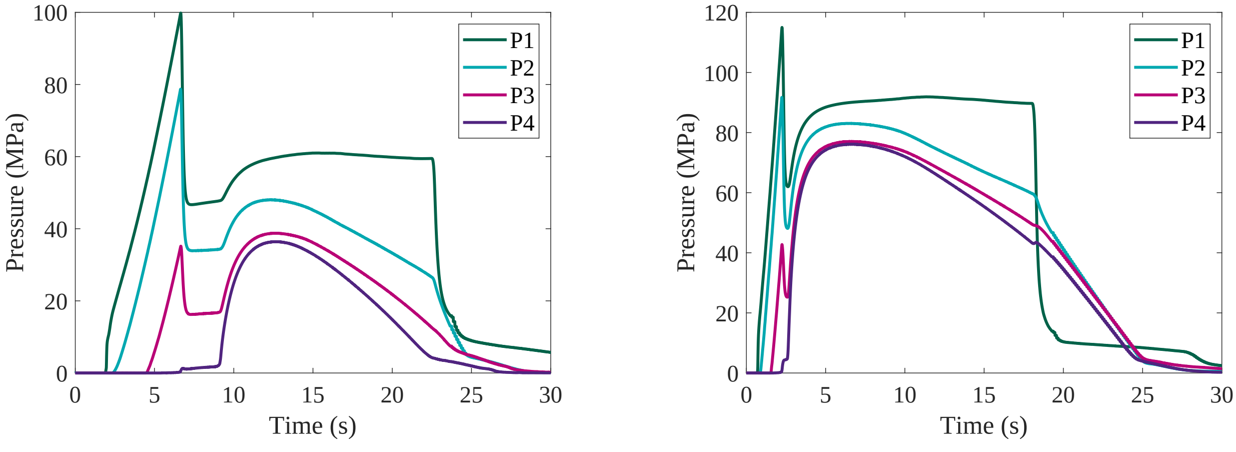

(a) S3 (b) S6

Figure 2.12 – The pressure signals measured during the injection molding of the full length 3 mm thick mold cavity for two different processing conditions: (a) S3, (b) S6.

signals around 10 s where the slope changes of the pressure drop in P2 and P3 could be an indication of a partial remelting of the gate leading more material to enter the cavity. Additionally, near the end of the packing phase, a slight increase in the P1 signal is observed in all example plots in Figure 2.13 affecting in turn the pressure decay slope in P2 and P3. This behavior can be explained by an over-compacting before the end of the packing phase. Similarly as seen in Figure 2.12, since we use a fixed switch-over condition for all experimental runs, a low injection velocity leads to having a less than fully filled part before switching and therefore the pressure plateau seen in Figure 2.13d for V22 in comparison to the smooth switch-over seen in Figure 2.13c for V15.

As already mentioned in Section 2.4.2, it is not possible to produce fully filled parts using the full length mold cavity with a 1.5 mm thickness. Therefore, all runs performed with this geometry under the conditions presented in Table 2.7 created short shoted U-shaped channels. One example pressure signal result is given in Figure 2.14a obtained during the W3 run. In this plot, P0 represents the specific injection pressure and as can be seen it reaches the machine's maximum injection pressure of 240 MPa without being able to fill the part. However, when using the insert to cut the channel length by half, it became possible to fill the cavity for most of the process settings summarized in Table 2.8. One representative result is presented in Figure 2.14b for the T20 run. One can observe the immense loss of pressure in the cavity by observing the P3 signal. This is due to the thinness of the cavity leading to faster polymer solidification.

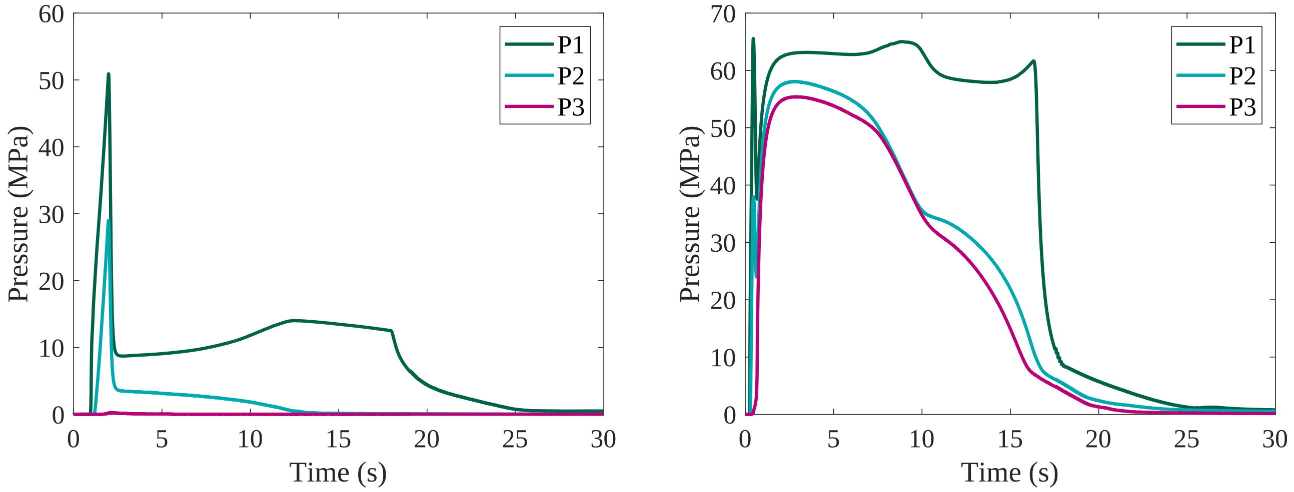

(a) V1

(b) V9

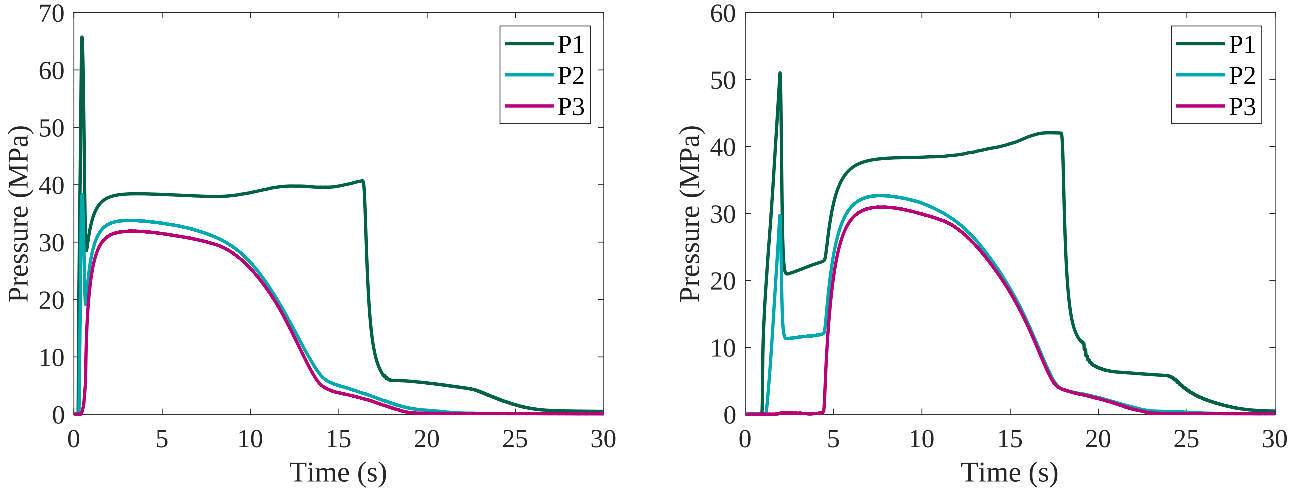

(c) V15

(d) V22

Figure 2.13 – The pressure signals measured during the injection molding of the half length 3 mm thick mold cavity for four different processing conditions: (a) V1, (b) V9, (c) V15, (d) V22.

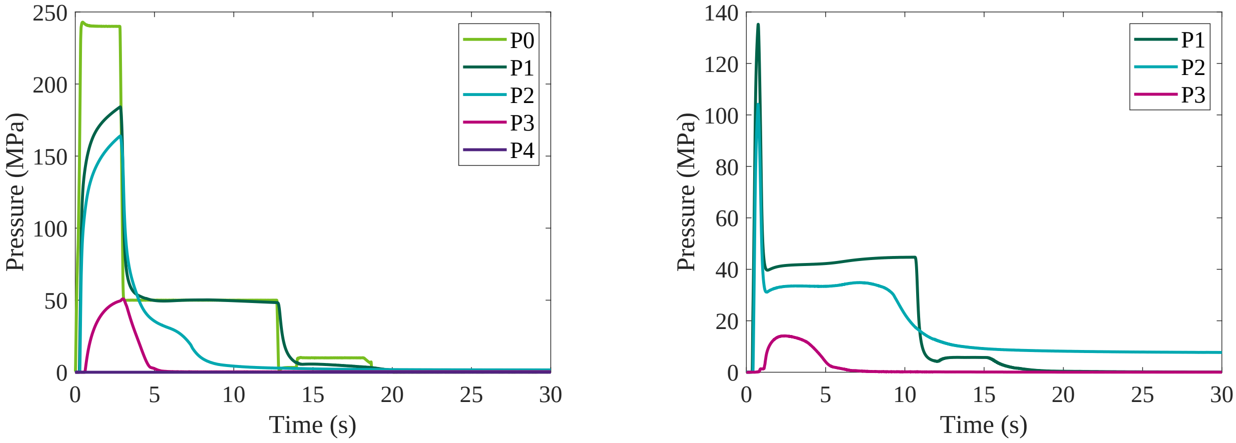

(a) W3 (b) T20

Figure 2.14 – The pressure signals measured during the injection molding of the 1.5 mm thick mold cavity: (a) using the full length geometry for condition W3, (b) using the half length geometry for condition T20.

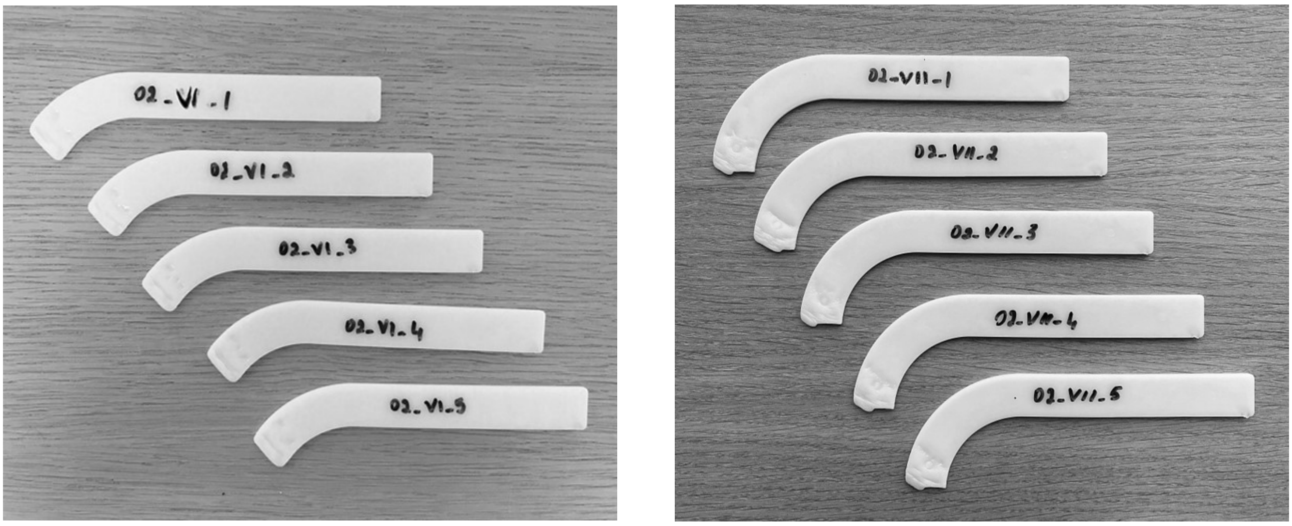

(a) V1 (b) V11

Figure 2.15 – Short shoted parts produced during the injection molding of the c mold cavity under two processing conditions: (a) V1, (b) V11.

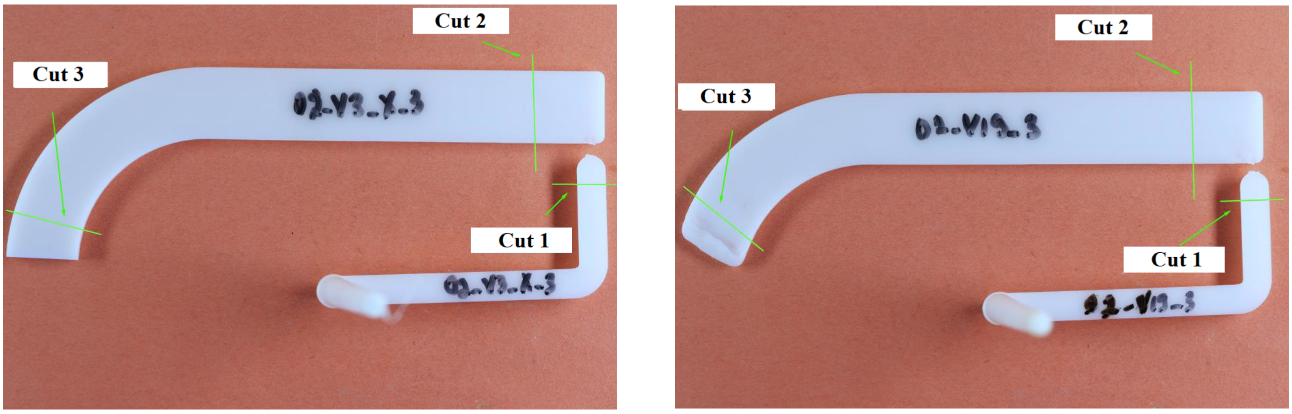

(a) V3

(b) V19

Figure 2.16 – The location of the microtome cuts used to observe the crystal morphology using polarized optical microscopy in the half length 3 mm thick parts: (a) in the case of a short shoted part, (b) in the case of a fully filled part.

2.4.5 Polarized Optical Microscopy

In order to visualize the different crystal morphologies that developed during the injection molding process, microtome cuts are made at the sensor locations from four produced samples and analyzed by polarized optical microscopy. The samples are taken from the injection of the half length 3 mm thick cavity having V1, V3, V19 and V21 as process settings (refer to Table 2.6). Figure 2.16a shows the location of the microtome cuts in the case of a fully filled part. Whereas, in the case of a short shot such as for V1 and V19, the third cut is made near the end of the part as shown in Figure 2.16b and annotated as Cut 3.

Figure 2.17 shows the results for V1 at the second pressure sensor located after the gate (P2) for three different magnifications (Figure 2.17a: 25x, Figure 2.17b: 50x, Figure 2.17c: 100x). As a first observation, it is apparent that as we move away from the wall to the core of the part the spherulites' size increases since the crystals have time to form and grow under no shear conditions. Another observation is the presence of a translucent skin layer indicating that the crystallites in this region are smaller than the wavelength of the utilized light. These small crystallites in this layer are postulated to have been formed under high shear conditions during the filling stage. In Figure 2.17, this layer's thickness is around 0.2 to 0.3 mm. Table 2.9 presents a summary of the approximately measured thicknesses for the different samples and cuts.

In addition to having Table 2.9, Figures 2.18, 2.19 and 2.20 present the micrographs of all mi-

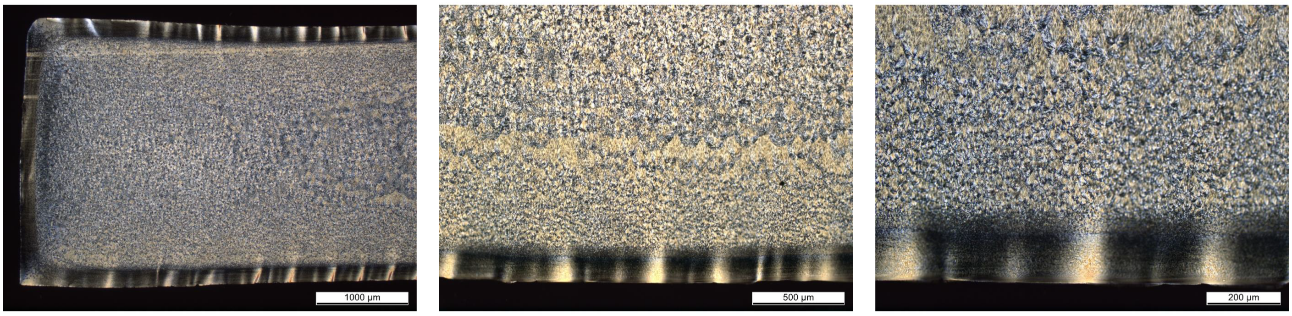

(a) 25x (b) 50x (c) 100x

Figure 2.17 – Micrographs of the microtome cut made at the second pressure sensor located after the gate (Cut 2) for the V1 processing condition under three different magnifications.

Table 2.9 – The measured skin layer thickness obtained from analyzing the micrographs from the polarized optical microscope.

	Skin Layer Thickness (mm)			
	V1	V3	V19	V21
Cut 1	0.2-0.4	0.1-0.2	0.14-0.2	0.06-0.16
Cut 2	0.2-0.3	0.11-0.13	0.12	0.09
Cut 3	0.1	0.07-0.09	-	0.04

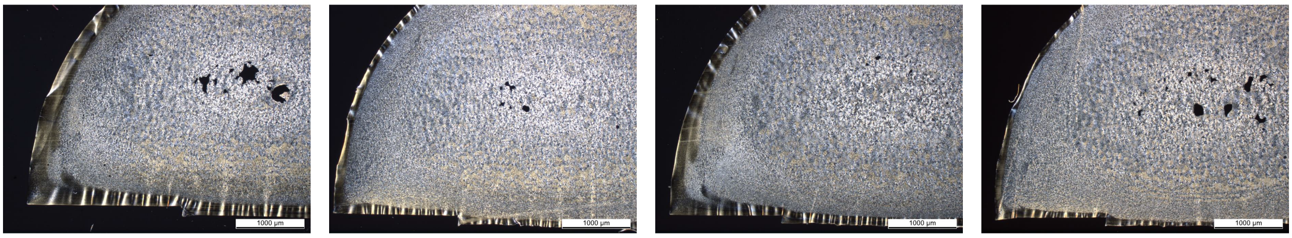

(a) V1 (b) V3 (c) V19 (d) V21

Figure 2.18 – Micrographs of Cut 1 using the same magnification of 25x for the four studied processing conditions: (a) V1, (b) V3, (c) V19, (d) V21.

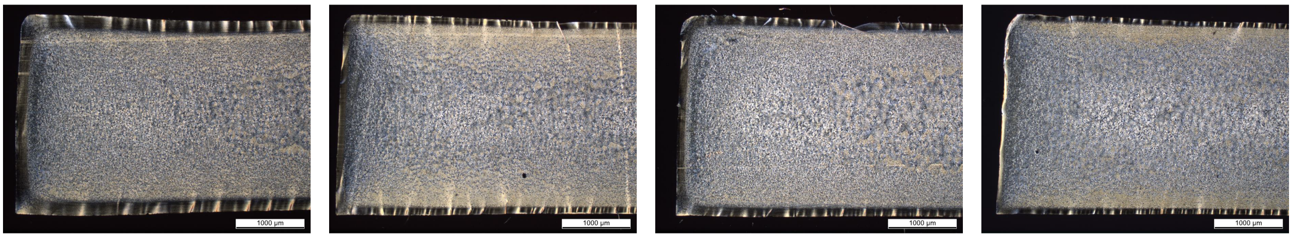

(a) V1 (b) V3 (c) V19 (d) V21

Figure 2.19 – Micrographs of Cut 2 using the same magnification of 25x for the four studied processing conditions: (a) V1, (b) V3, (c) V19, (d) V21.

crotome cuts with a magnification of 25x. By analyzing the figures and the data in the table, it is possible to study the effect of the mold temperature and the injection velocity on the thickness of the skin layer. As the mold temperature increases from 80 °C in V1 and V3 to 110 °C in V19 and V21, the skin layer is slimmer. This is to be expected as a higher mold temperature leads to a slower solidification of the polymer melt and therefore a smaller skin layer. Similarly, increasing the injection velocity from 10 cm^3/s in V1 and V19 to 50 cm^3/s in V3 and V21 leads to a thinner skin layer as the molten material has less time to fully crystallize and solidify near the mold surface. Additionally, the skin layer thickness becomes thinner the further it is from the injection location. This is highlighted by comparing the different cuts made at the same process condition. The cuts made before the gate shown in Figure 2.18 have a skin layer around two times thicker than the ones made near the end of the part presented in Figure 2.20.

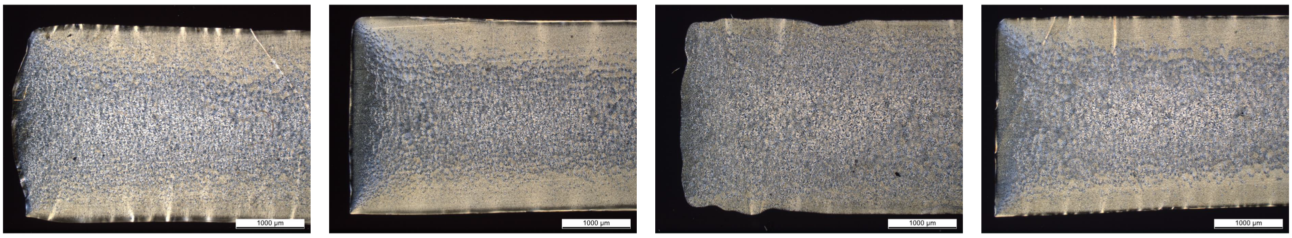

(a) V1 (b) V3 (c) V19 (d) V21

Figure 2.20 – Micrographs of Cut 3 using the same magnification of 25x for the four studied processing conditions: (a) V1, (b) V3, (c) V19, (d) V21.

2.5 Conclusion

In this chapter, the material used in this work was presented along with two types of material characterization experiments. The first type was the DSC measurements which provided information about the material's crystallization behavior under different cooling rates. This made it possible to determine the melting temperature of the material at 178.88 °C and the crystallization enthalpy of 155.35 J/g. The relative crystallinity evolution with temperature and time under the various cooling rates was also determined and will be used to quantify the crystallization kinetics of POM in Chapter 4. The second type of experiment is a dynamic temperature ramp test used to identify the temperature-dependency of the viscosity and observe its behavior after the onset of crystallization. This data will similarly be used to determine the viscosity model parameters later on in the work.

A mold was designed to provide the possibility to produce four different geometries varying by length and/or thickness in addition to measuring the pressure signals during the injection molding process at four locations in the cavity. To set-up the injection molding trials, filling and packing studies were performed followed by the official trials where for each geometry three process settings are varied. The variable settings are the mold temperature, the injection velocity and the holding pressure. Some characteristic pressure signals were analyzed in this chapter to give an overview of the obtained results that are used in this work for the calibration of model parameters.

Some of the injection molded samples were studied using a polarized optical microscope to get a deeper insight into the crystal morphologies and the different layers that form during the process. Microtome cuts were made at the sensor locations for different process settings to study the effect of mold temperature and injection velocity on the morphology and skin layer thickness. By observing the various micrographs, it became apparent that the higher the mold temperature and the injection velocity the thinner the skin layer is.

Chapter 3

Feasibility Study: Use of Surrogate Modeling for Modeling Parameter Calibration

Content

3.1 Introduction

In this chapter, the feasibility of using surrogate modeling to calibrate parameters in an injection molding simulation is studied. Three modeling parameters are chosen for the calibration in this study. These are the heat transfer coefficients during filling and packing as well as the pressure-dependency coefficient in the Cross-WLF viscosity model [117, 118]. The before-mentioned parameters are known to affect the pressure results in the simulation and their experimental determination is challenging and time-consuming [119–121]. For this calibration, the half length 3 mm thick geometry presented in Figure 2.11 is utilized and the three modeling parameters are calibrated using the experimental P2 pressure sensor data (refer to Figure 2.9).

In this feasibility study, the accuracy of three regression-based surrogate modeling techniques and two design of experiment methods in their ability to approximate the pressure signal at a single node in the simulation is studied. The proposed modeling approaches are the following:

1. a non-linear regression model of proper orthogonal decomposition coefficients trained using a fixed Latin Hypercube sampling (POD-NLR),
2. a polynomial chaos expansion model fitted with a least-squares optimization technique using the same fixed Latin Hypercube sampling points (Regular-PCE-LS), and
3. a polynomial chaos expansion model fitted with a least-squares optimization technique but using an adaptive DoE that is enriched while generating the model (Adaptive-PCE-LS).

The models are trained using 30, 60 and 120 simulation runs and their predictions are assessed accordingly. The three models are built by varying a total of six input parameters, including process settings and modeling variables. The process parameters are the injection velocity, coolant inlet temperature, holding pressure and the modeling parameters, as already mentioned, are the heat transfer coefficients during filling and packing as well as the pressure-dependent coefficient in the Cross-WLF viscosity model. After obtaining the surrogate models, a sensitivity analysis is performed to study the contribution of each varied parameter to the pressure signal as well as their interaction with each other. Finally, using the measured experimental pressure data and one of the generated surrogate models, the modeling parameters are calibrated and the error between the optimized simulation and the default one is compared.

3.2 Software Tools

3.2.1 Injection Molding Simulation

The injection molding simulations are performed using Autodesk® Moldflow® Insight 2021.1 (AMI2021.1). The simulations are automated with the help of the three command line control functions. This set of utilities allow the use of third-party software in tandem with the simulation runs in order to automatize extensive studies such as optimizations and sensitivity analyses... The main functions are editing, running, and retrieving results from a user-customized Moldflow® analysis automatically through a command line interface. The following are the available utilities:

1. *studymod*: This command generates a modified simulation study from a base study using an XML format modifier file (modified geometry, boundary condition, process/model parameters).
2. *runstudy*: This command launches a new simulation analysis.
3. *studyrlt*: This command extracts simulation results from a finalized analysis in simple text or XML file format.

3.2.2 Python Uncertainty Quantification Library

The Python Uncertainty Quantification (pyUQ) library is a Bosch proprietary Python tool providing the user the ability to perform uncertainty quantification (UQ) on simulation models using state-of-the-art UQ models and methods. The methods cover the design of experiments, surrogate modeling, sensitivity analysis and statistical analysis. The pyUQ module provides functions that can be modified or extended to act as an interface between simulation tools and UQ methods. Parameter uncertainties are defined in this tool using standard distributions (uniform, normal, Gamma, Beta) by stating the parameter's upper and lower limits. The module offers four basic modern DoEs such as Standard-Monte Carlo, Quasi-Monte Carlo, Latin Hypercube sampling and more refined sparse grid experimental methods like Non-Intrusive Spectral Projection. There are five different surrogate modeling techniques that this library supports:

1. Polynomial Chaos Expansion (PCE) using least square (LS) as optimization methods,
2. PCE using least angle regression (LAR) as optimization method,
3. Gaussian Process Regression (GPR),

4. Pseudo Spectral Projection method (PSP),
5. Stochastic Collocation method.

The simulation results are stored in a Hierarchical Data Format (HDF5) to be able to efficiently perform statistical analysis or surrogate model generation using this tool. HDF5 is a folder-like storage structure, which saves data in compressed format and allows data slicing leading to efficient memory usage. Apart from these features, the main highlight of this tool is its active learning algorithm with an adaptive DoE generation which is one of the methods evaluated in this work.

3.2.3 MATLAB

The POD model order reduction and the non-linear regression of the respective POD-based coefficients are implemented in MATLAB R2019b. The fmincon built-in function of the optimization toolbox is used for the optimization of the POD-based surrogate model.

3.3 Simulation Environment

The 3D high-fidelity simulation model is set-up in AMI2021.1 using the respective POM material card given in the Moldflow® database. The simulations are recreating the injection molding experiments for the half length 3 mm thick part presented in Section 2.4 along with example pressure signals in Figure 2.13. The simulation consists of a cooling, fill and pack analyses. Therefore, the simulation model included cooling channels meshed as beam elements and the part as well as the feed system (nozzle & flange) meshed using tetrahedral elements with 24 layers through the thickness. The feed system is defined as hot runner in the simulation model. Lateral and top views from the meshed model are shown in Figure 3.1a and Figure 3.1b, respectively. The process settings of the base simulation are defined according to imported data from the ENGEL sim link software tool. These include the filling and packing profiles along with the switch-over ram position and the machine settings. A single simulation requires around 75 minutes to be completed on a workstation with a 4.10 GHz processor and 32 GB RAM.

The various surrogate models are obtained by modifying six parameters in the simulation. Three of which are the process parameters changed during the experimental trials as presented in Table 2.4 for the half length 3 mm thick part (HL3). Since a cooling analysis is performed in the simulations,

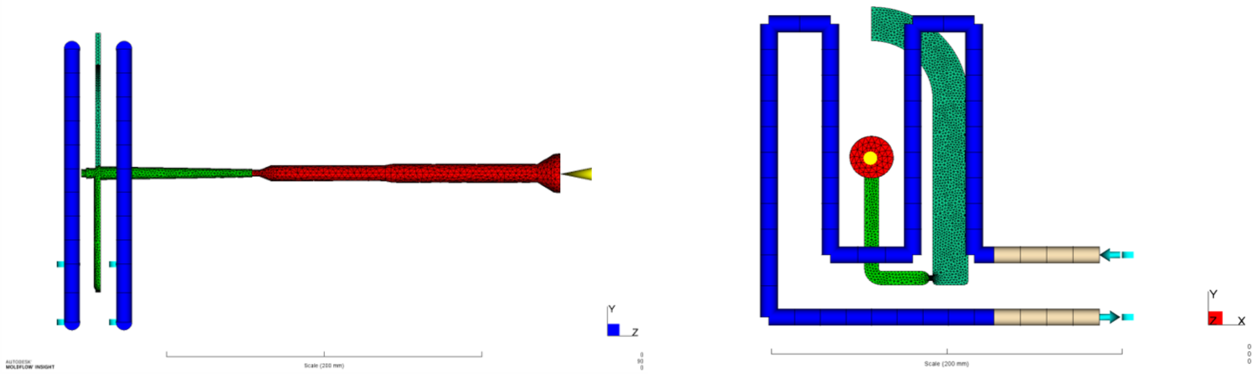

(a) Lateral view

(b) Top view

Figure 3.1 – The meshed simulation model including the part (dark green), runner and sprue (light green), cooling channels (blue) and feed system (red).

Table 3.1 – Varied parameters in the simulation runs used to generate the surrogate models along with their upper and lower bounds.

Surrogate Model Variables	**Lower Bound**	**Upper Bound**
Injection Velocity, V_{inj} (cm^3/s)	10	50
Coolant Inlet Temperature, $T_{c,in}$ (°C)	84	114
Holding Pressure, P_{hold} (MPa)	20	80
Heat transfer coefficient (filling), $HTC_{filling}$ (W/m^2°C)	5000	10000
Heat transfer coefficient (packing), $HTC_{packing}$ (W/m^2°C)	1000	5000
Viscosity model parameter, D_3 (K/MPa)	0	0.4

the inlet cooling temperature $T_{c,in}$ is varied such as $T_{c,in} = T_{mold} + 4$ of the T_{mold} set experimentally. The other three varied parameters are the heat transfer coefficient during filling ($HTC_{filling}$) and during packing ($HTC_{packing}$) as well as the pressure-dependency coefficient (D_3) of the Cross-WLF viscosity model (refer to Appendix A). Table 3.1 summarizes the surrogate models' variables and their bounds. The HTC ranges are chosen in reference to the default Moldflow® values ($HTC_{filling} = 5000$ W/m^2°C, $HTC_{packing} = 2500$ W/m^2°C). As for the pressure-dependent viscosity model parameter, the variation range goes from 0 up to 0.4 K/MPa in order to cover the actual behavior of POM and other typical semi-crystalline thermoplastics such as PP [122].

Table 3.2 – Definition of the testing simulations for evaluating the performance of the surrogate models.

DoE Name	V_{inj} (cm^3/s)	$T_{c,in}$ (°C)	P_{hold} (MPa)	$HTC_{filling}$ (W/m^2°C)	$HTC_{packing}$ (W/m^2°C)	D_3 (K/MPa)
Test 1	36.0	98.2	55.1	5175	4522	0.33
Test 2	15.5	87.3	74.7	9751	2143	0.07
Test 3	45.6	109.4	47.5	8092	3945	0.21
Test 4	27.2	106.2	25.9	7338	1640	0.12

3.4 Proposed DoE and Surrogate Modeling Techniques

In this study, three different combinations of DoEs and surrogate modeling methods are used in order to compare their performance in predicting the pressure signal results at one surface node corresponding to the location of the second sensor in Figure 2.9. Additionally, the total number of simulations used for the training phase is varied such as 30, 60 and 120 simulation runs are considered and their performance is tested using four additional runs. The testing simulations are summarized in Table 3.2.

3.4.1 POD-NLR

The POD-based surrogate model whose parameters are fitted using non-linear regression (NLR) is referred to as POD-NLR. To generate this model, LHS is used to obtain the DoEs according to the needed total number of training simulations S. The obtaining of the final model requires the following steps after running all the simulations according to the DoE:

1. *Pre-processing*: the various nodal pressure results P_i $(i = 1, \cdots, S)$ are pre-processed by shifting all corresponding time series by t_{start} so that all non-zero signals start at $t_0 = 0$ s and followed by the resampling of the pressure data using a common time vector from 0 to 50 s with 0.02 s time steps. This step is important given that the different simulation settings lead to different times at which the flow front reaches the sensor node and produces a non-zero pressure signal.

2. *Model order reduction*: the POD basis functions ϕ are calculated by solving the eigenvalue problem $PP^TV = \lambda V$ where the eigenvectors V corresponding to the most influential eigenvalues

λ constitute the basis functions able to reconstruct the pressure signal by:

$$P^{(s)}_{reconstructed} = \sum_{i=1}^{n} \Gamma^{(s)}_{n} \phi_n \tag{3.1}$$

where s is the simulation number, n is the number of modes or basis obtained according to a specified error value and $\Gamma^{(s)}_n$ is the POD parameter for a specific mode n and simulation s. The truncation criterion is done according to an error value of $\epsilon = 10^{-3}$ which only selects the modes corresponding to eigenvalues that fulfill the condition $\frac{\lambda}{\lambda_{max}} \geq \epsilon$.

3. *Model fitting*: a least-squares regression of a second-order polynomial is used to train a model to predict the POD parameters Γ and the time shift value t_{start} as follows:

$$\Gamma^{(s)}_n = a^{(n)} + b^{(n)}_i X^{(s)}_i + c^{(n)}_{ij} X^{(s)}_i X^{(s)}_j \tag{3.2}$$

$$t^{(s)}_{start} = d + e_i X^{(s)}_i + f_{ij} X^{(s)}_i X^{(s)}_j \tag{3.3}$$

where X_i and X_j are the surrogate model input variables with $i \neq j$ representing the number of variables $(1, \cdots, 6)$ and a, b, c, d, e, f are the surrogate parameters. In equations 3.2 and 3.3 the implicit Einstein summation convention is used for indexes i and j. This implementation is restricted to bilinear regression in order to mitigate overfitting the data.

3.4.2 Regular-PCE-LS

The same LHS DoEs used to train the POD-NLR model are employed as inputs to a second-order PCE-based surrogate model. The model parameters are trained using least-squares regression and thus referred to as regular-PCE-LS since the DoE is fully predefined. The PCE model is generated using the pyUQ library using the following steps:

1. *Pre-processing*: similar to POD-NLR, a resampling step is performed to have a unique time index starting with $t_0 = 0$ s and spanning to 50 s with 0.02 s time steps.

2. *Polynomial chaos expansion*: since the surrogate model input variables have a uniform distribution, after applying the Gram-Schmidt orthogonalization to equation 1.43, the Legendre polynomial family is obtained and thus used as basis functions to represent the pressure signal results from the simulation. A hyperbolic truncation of 1 is utilized to generate the model which

signifies that all interaction effects are considered in the PCE basis. Additionally, the PCE regression order is estimated by pyUQ using heuristics and in this case a second-order regression is used.

3. *Model fitting*: the algorithm uses the pressure time-dependent training data to solve an optimization problem which minimizes the squared residuals between the simulation's pressure signals and the predicted output of the PCE model. The solution of the least-squares optimization problem is the vector containing the polynomial coefficients.

3.4.3 Adaptive-PCE-LS

A sequential design of experiment (SDOE) is used to build iteratively a DoE from a big candidate DoE obtained with QMC according to the importance of the input variables. The surrogate model utilizes PCE and is trained using least-squares regression. This model is generated using the pyUQ library and is referred to as adaptive-PCE-LS since its DoE is enriched as the model is being generated making it an adaptive approach. Therefore, given a sample set, the surrogate model generation follows the same steps presented in regular-PCE-LS. The main difference between the two methods lies in the iterative steps needed to build the whole surrogate model by updating the DoE.

The algorithm starts with an initial small LHS DoE of 10 simulations and is enriched after each iteration with 5 additional sample points from a large QMC candidate DoE (1000 samples). The enrichment is done via the bootstrap method [123] which calculates the local variances of the surrogate model and chooses the new sample points that lead to the maximum variance. In other words, it performs a UQ analysis on the simulation results to estimate which parameters contribute most to the statistical fluctuations. This process is repeated until convergence in terms of maximum simulations S of 120 or a global error threshold E of 10^{-2} is achieved.

The surrogate model is assessed by cross-validation using the training data set with the leave-one-out error method such as the model is generated from $S-1$ simulations and evaluated on the remaining one simulation result. The standard error metric used to evaluate the surrogate model after each iteration is its global error. This error value is an average of a scalar model output predefined by the user. In this work, the selected scalar quantity corresponds to the mean value of the pressure vector at the studied node.

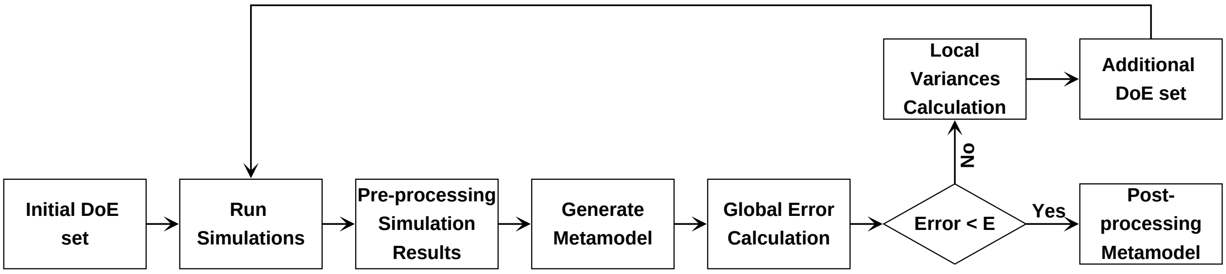

Figure 3.2 – Workflow for generating an adaptive surrogate model using the pyUQ active learning algorithm.

Table 3.3 – An overview of the proposed DoE and surrogate modeling techniques.

Surrogate model Acronym	**DoE Technique**	**Surrogate model Technique**	**Fitting Method**
POD-NLR	Latin Hypercube	Proper orthogonal decomposition	Least-squares regression
Regular-PCE-LS	Latin Hypercube	Polynomial chaos expansion	Least-squares regression
Adaptive-PCE-LS	Sequential DoE (LHS & QMC)	Polynomial chaos expansion	Least-squares regression

The flowchart in Figure 3.2 presents a summary of the steps followed while generating the adaptive-PCE-LS surrogate model using an active learning/adaptive approach.

For the sake of clarity, the characteristics of the three studied surrogate models are summarized in Table 3.3.

3.5 Evaluation Strategy

To evaluate and compare the various surrogate models, the root mean squared error (RMSE) is used. Let the surrogate model response and the true values of the high-fidelity simulation model or experiment be represented by $\hat{Y}$ and Y, respectively. Using these notations, the RMSE is computed by evaluating the surrogate model pointwise on a given test data set, such as:

$$RMSE(Y, \hat{Y}) = \sqrt{\frac{1}{n}\sum_{i=1}^{n}(Y^i - \hat{Y}^i)^2} \tag{3.4}$$

where n is the total number of data points. In this work, this error is normalized using the min-max normalization method to be able to compare the various surrogate modeling techniques:

$$Normalized\,RMSE(Y,\hat{Y}) = \frac{RMSE(Y,\hat{Y})}{Y_{max} - Y_{min}}. \tag{3.5}$$

3.6 Optimization

In this feasibility study, an optimization routine is performed to identify the uncertain simulation model parameters: $HTC_{filling}$, $HTC_{packing}$ and D_3. For these purposes, the sensor data from the 27 experimental runs presented in Table 2.6 are utilized. The optimization problem aims at minimizing the difference between the experimental results Y^{exp} and the surrogate model predictions $\hat{Y}$ by varying the respective uncertain input parameters of the surrogate model. It can be represented as follows:

$$\begin{aligned}
\text{find} \quad & Var = (HTC_{filling}, HTC_{packing}, D_3),\\
\text{argmin} \quad & \sum_{i=1}^{27} \|Y_i^{exp}(\mathbf{V}) - \hat{Y}_i(\mathbf{X})\|,\\
\text{with} \quad & \mathbf{V} = (V_{inj}, T_{c,in}, P_{hold}),\\
& \mathbf{X} = (V_{inj}, T_{c,in}, P_{hold}, HTC_{filling}, HTC_{packing}, D_3),\\
\text{s.t.} \quad & 5000 \leq HTC_{filling} \leq 10000 \quad (\text{W/m}^2{}^\circ\text{C}),\\
& 1000 \leq HTC_{packing} \leq 5000 \quad (\text{W/m}^2{}^\circ\text{C}),\\
& 0 \leq D_3 \leq 0.40 \quad (\text{K/MPa}).
\end{aligned}$$

3.7 Results and Discussion

3.7.1 Comparison of Surrogate Models

The performance of the three surrogate model techniques is assessed by their ability to predict the pressure signal at a surface node in simulations unseen by the model. In this work, those test simulations are presented in Table 3.2. Although the total simulated time is around 48 s, the main focus is on the pressure signal between 0 and 22 s. This interval includes the filling phase between 0 and ∼2 s, the packing phase till ∼18 s and the start of the cooling phase until the pressure goes to 0 MPa before 22 s. Therefore, all the error metrics and plots consider only this time interval.

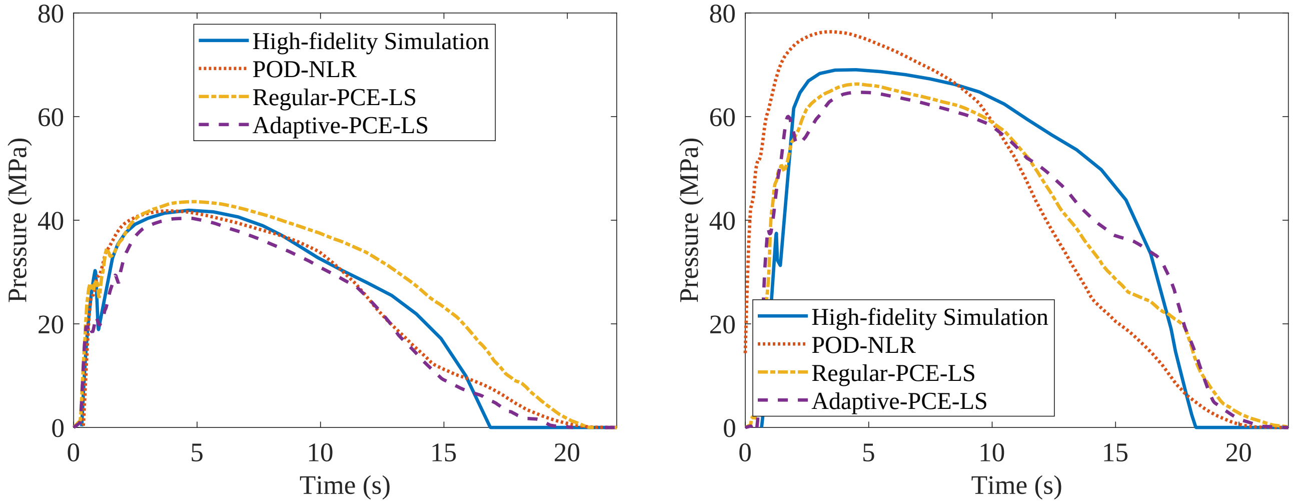

(a) Test 1 (b) Test 2

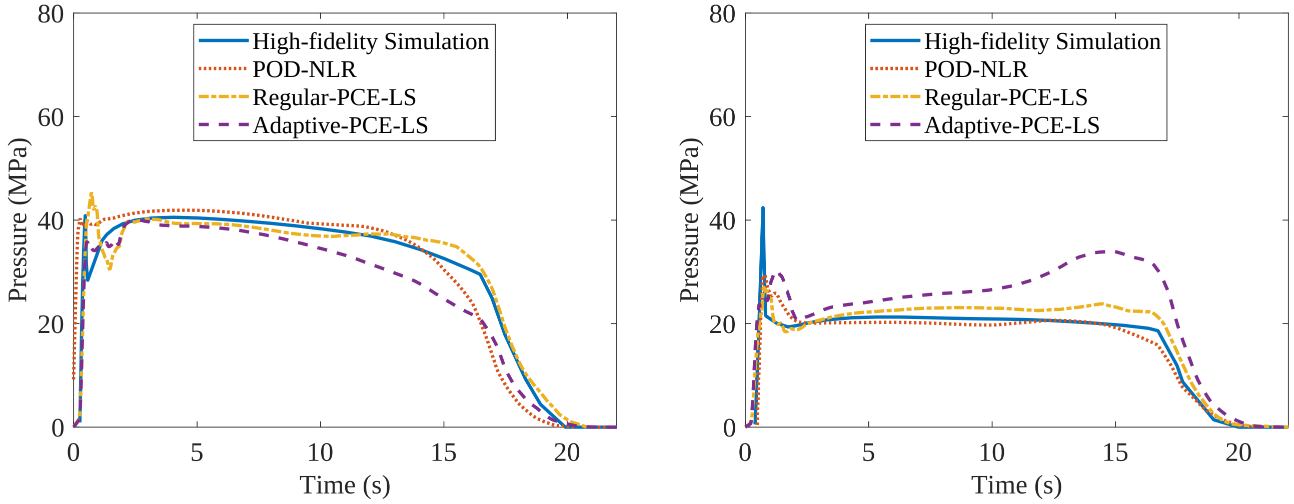

(c) Test 3 (d) Test 4

Figure 3.3 – Predicted pressure signals by the three proposed surrogate models after training with 30 simulations in comparison to the true high-fidelity simulation results for four test cases.

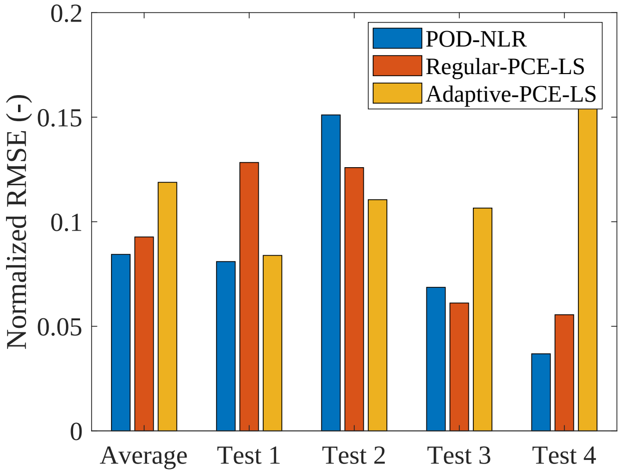

Figure 3.4 – RMSE of the three studied surrogate modeling methods after training with 30 simulation runs.

Figure 3.3 presents the models' predictions obtained after using 30 training simulation runs in comparison to the true high-fidelity simulation results. At first glance, it seems that all three surrogate models are able to capture the main features of the pressure signal after only 30 training simulations. However, one can distinguish some particular discrepancies such as the inability of the POD-based model to predict the t_{start} for Test 2 and error of the adaptive-PCE for estimating the pressure at the end of packing in Tests 3 and 4. Additionally, there are deviations by predicting the pressure peak at the end of the filling phase for all surrogate models.

A quantitative analysis of the performance of the different surrogate models is given in Figure 3.4, where the normalized RMSE is plotted for the four test simulations. The average normalized RMSEs of 0.084, 0.093 and 0.119 for POD-NLR, regular-PCE-LS and adaptive-PCE-LS, respectively, show that the POD-based surrogate model is slightly more accurate in recreating the simulation results after training with 30 high-fidelity simulations than the PCE-based models.

Looking to increase the prediction capability, the number of simulations used to train the surrogate models is doubled to 60. Overall, this increase in training simulations led to noticeable improvements in the pressure signal predictions of the test runs as shown in Figure 3.5. For example, by comparing Figures 3.3b and 3.5b, the POD-based model is now able to better predict the t_{start} for Test 2 as well as both PCE-based models can estimate the pressure result more accurately during the packing phase. In general, there is still room for improvements when estimating the pressure for Test 4 as well as predicting the pressure peak at the end of filling and the time at which the pressure goes to zero at the start of the cooling phase.

Figures 3.6 shows the normalized RMSE and for the three studied surrogate modeling methods after training them with 60 simulation runs. The increase in training points improved the accuracy of all models as shown by the average normalized RMSE of of 0.076, 0.082 and 0.10 for POD-NLR, regular-PCE-LS and adaptive-PCE-LS, respectively. Unexpectedly the RMSE for the POD-NLR and regular-PCE-LS in the Test 4 increased from 3.7 % to 9.2 % and from 5.5 % to 12.1 %, respectively, when increasing the number of training simulations. This could be due to a slight overfitting.

As final attempt to improve the surrogate models' performance,, especially for the case of Test 4, 120 simulations are used to train them. Figure 3.7 presents the pressure evolution as a function of time for all four test simulations. By comparing with Figure 3.3, it turns out that the performance of all surrogate models improved after 120 training simulations and they appear to converge to the same result. The models still struggle to predict the early pressure drop at the end of the packing phase in Test 1 and Test 2 as shown in Figures 3.7a and 3.7b, respectively. Additionally, the estimation of the pressure peak in the filling phase is a problematic location for all models and especially highlighted in Test 4 as seen in Figure 3.7d. The normalized RMSE is presented in Figure 3.8. The error of all surrogate models is lower than 8 % after training with 120 high-fidelity simulation runs. The model based on PCE-LS using an adaptive DoE exhibits the lowest average error of 5.8 %.

Based on the previous results, all three surrogate modeling methods improved gradually their performance with the increase of the number of training simulations. This fact is depicted in Figure 3.9, in which the average normalized RMSE of each model is plotted versus the number of simulations used to train it. Both the POD-NLR and regular-PCE-LS surrogate models reached an average RMSE below 10 % already after training with 30 simulations. Whereas the adaptive-PCE-LS model showed the highest average error after 30 training runs and only reached comparable low errors to the other two surrogate modeling techniques after 120 training simulations. For the two models using a fixed DoE, increasing the number of training simulations from 30 to 120 led to a relatively small decrement of the prediction error from 8.4 % to 6.3 % for the POD-based model and from 9.3 % to 6.3 % for the PCE-based one. As for the adaptive-PCE-LS model, the average RMSE decreased significantly from 11.9 % to 5.8 % after training with 120 runs leading to much improved predictions.

By comparing the results of the two surrogate models based on PCE-LS, it appears that not only the number of training simulations but the choice of DoE play an important role in determining the

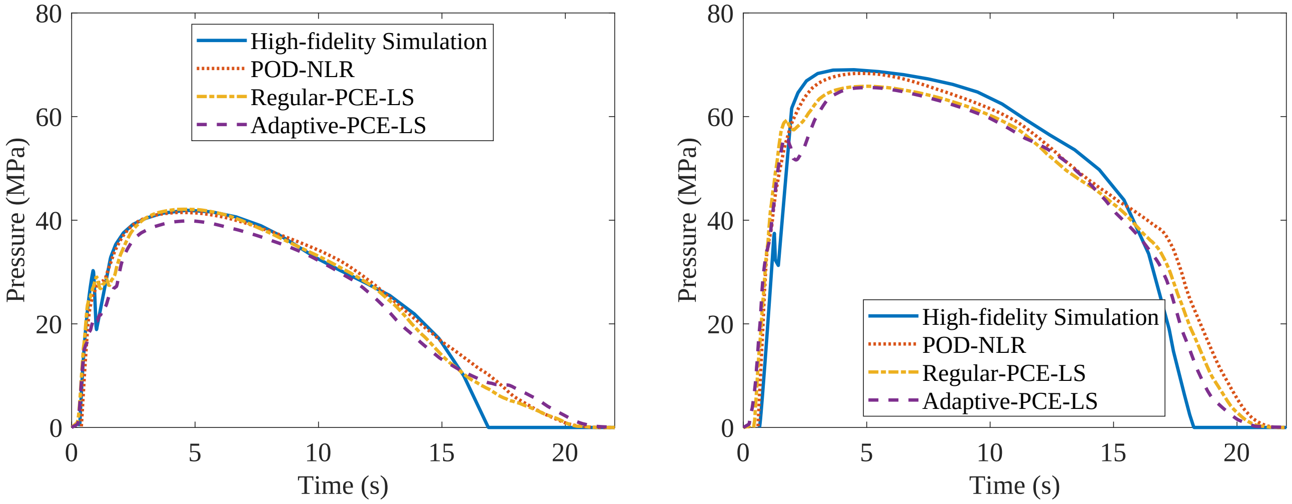

(a) Test 1 (b) Test 2

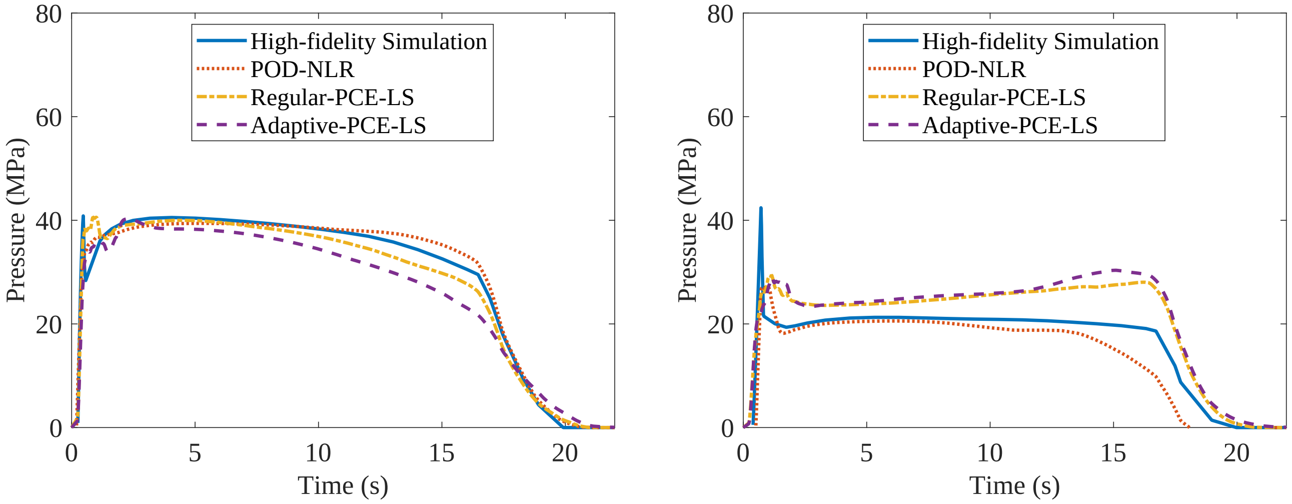

(c) Test 3 (d) Test 4

Figure 3.5 – Predicted pressure signals by the three proposed surrogate models after training with 60 simulations in comparison to the true high-fidelity simulation results for four test cases.

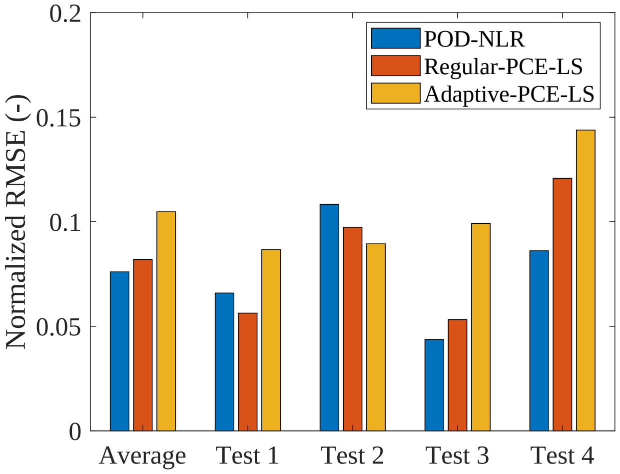

Figure 3.6 – RMSE of the three studied surrogate modeling methods after training with 60 simulation runs.

model performance. An adaptive DoE only leads to a better surrogate model performance when using a relatively high number of training runs in comparison to another which uses a fixed random DoE. In this particular work, running 120 high-fidelity simulations necessitates around 6 days and represents an acceptable computational cost for gaining higher accuracy in front of a surrogate model generated with a fixed random DoE. However, in case of a low number of available training simulation, a pre-defined DoE is a pertinent alternative for surrogate model generation as corroborated by the results of the POD- and PCE-based models with a fixed random DoE. In terms of global performance, the POD-based model is slightly more accurate than the PCE-based models when using low number of training simulations but as this number increases the difference between the two techniques becomes negligible.

3.7.2 Sensitivity Analysis

A Sobol sensitivity analysis is performed using the generated adaptive-PCE-LS surrogate model trained with 120 simulation runs. Figures 3.10 and 3.11 show the resultant first order and some of the second order sensitivity indices, respectively.

The first order indices underline the contribution of a certain surrogate model parameter to the variance of the pressure output as explained in Section 1.4.6.1. The sensitivity of the different process settings shown in Figure 3.10a are in agreement with the common understanding of the injection molding process. The injection velocity is the more sensitive factor during the filling stage because

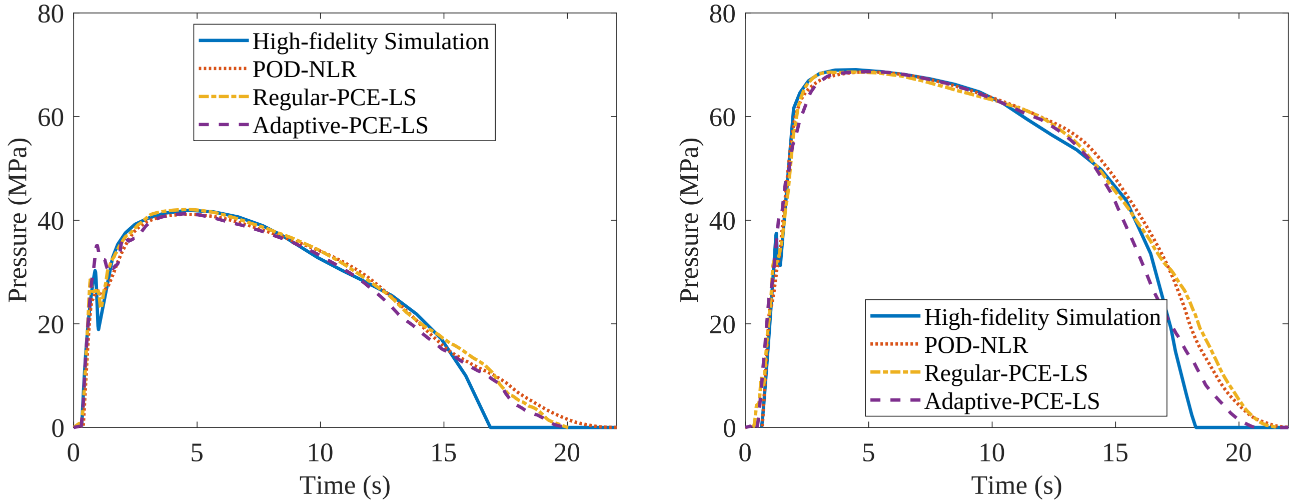

(a) Test 1 (b) Test 2

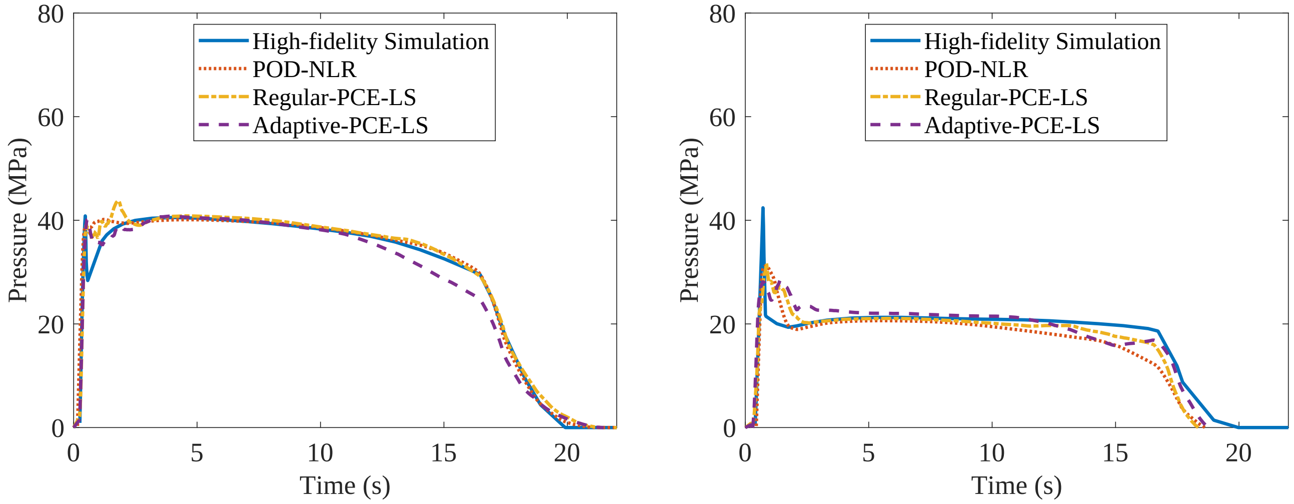

(c) Test 3 (d) Test 4

Figure 3.7 – Predicted pressure signals by the three proposed surrogate models after training with 120 simulations in comparison to the true high-fidelity simulation results for four test cases.

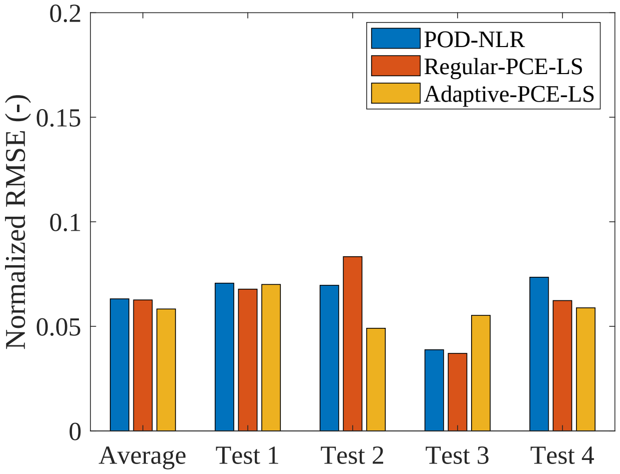

Figure 3.8 – RMSE of the three studied surrogate modeling methods after training with 120 simulation runs.

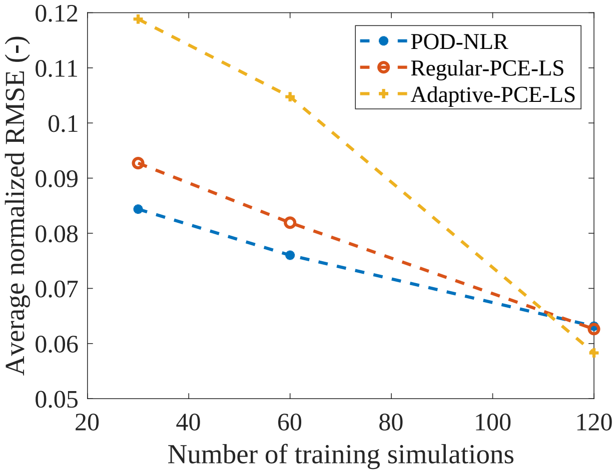

Figure 3.9 – Average normalized RMSE over the five test runs for each surrogate model generated as a function of the number of training simulations used.

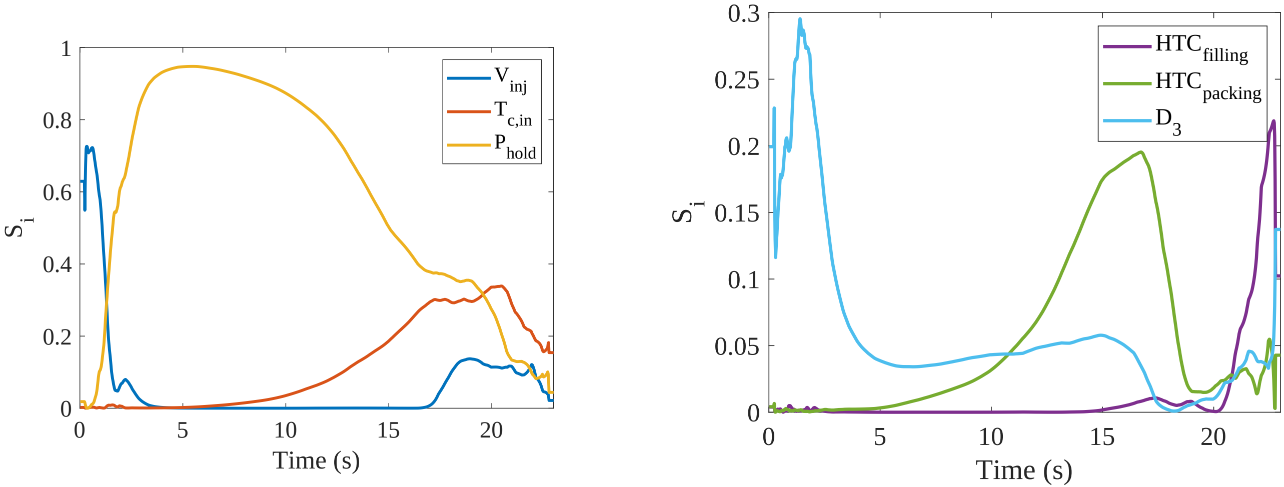

(a) Process parameters

(b) Modeling parameters

Figure 3.10 – The first order Sobol sensitivity indices obtained using the generated adaptive-PCE-LS surrogate model trained with 120 simulation runs.

it determines directly the pressure need. On the other hand, the holding pressure is naturally the more sensitive parameter during the packing phase, just after the switch-over till the time when the gate is completely solidified. After which the contribution of the coolant inlet temperature is the main driver of part shrinkage and therefore pressure development. The sensitivity of the HTC values and the pressure-dependent viscosity coefficient is presented in Figure 3.10b. During the filling and the beginning of the packing phase, the pressure signal is highly sensitive to changes of the pressure-dependent viscosity coefficient D_3, which is in principle an expected result given the natural impact of the viscosity model in the simulation of the filing stage. As for $HTC_{packing}$, it appears to affect the pressure output mainly at the time in which the gate freezes during the packing phase. Finally, it turns out that the $HTC_{filling}$ has no effect on the pressure results during the filling phase. The sensitivity of $HTC_{filling}$ after 20 s is certainly an artifact of the surrogate model, because this parameter should not play any role at this time in the high-fidelity simulation.

Figure 3.11 presents some of the second order sensitivity indices representing the most important interactions between the surrogate model parameters as a function of time in relation to their combined contribution to the output pressure. During the filling phase, the main interaction is given by the injection velocity and D_3. As for the beginning of the packing phase, the most important interactions are given by the holding pressure along with both the injection velocity and D_3. Whereas, along the packing phase, it turns out that there is not significant two-parameter relations affecting the

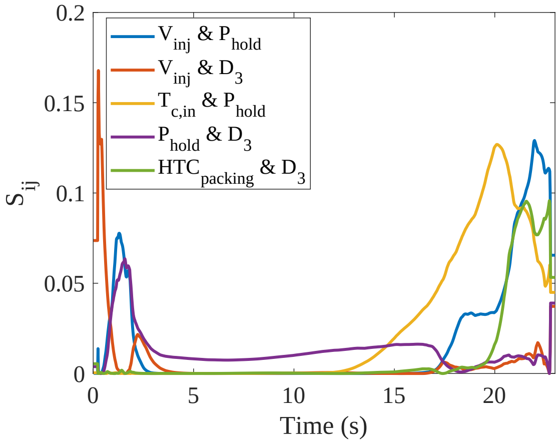

Figure 3.11 – The second order Sobol sensitivity indices obtained using the generated adaptive-PCE-LS surrogate model trained with 120 simulation runs.

pressure development. Interestingly, at the time when pressure strongly drops during the packing phase, probably associated to the freezing of the gate, pressure development is controlled by the interaction between the holding pressure and the coolant inlet temperature. The interaction between $HTC_{packing}$ and D_3 after 20 s is difficult to explain in terms of polymer physics, but eventually reveals some subtleties caught in the complexity of the simulated phenomena.

In general, such sensitivity analyses are helpful in understanding the effect of parameters on specific output results. One way they can play an important role in surrogate model generation is by pinpointing the most influential parameters at the regions in which the model exhibits the large errors. For example, at the end of the filling phase, the models are not fully capable to predict the correct pressure drop, as can be seen in Figures 3.7c and 3.7d . A possible way to improve these predictions is by adding DoE points where we mainly vary the injection velocity, holding pressure and D_3 as their first and second order sensitivity indices show their high contribution to the output in this region.

3.7.3 Modeling Parameter Calibration

All three models performed similarly after training with 120 high-fidelity simulations as shown in Figure 3.9. The POD-based surrogate model is used for the parameter optimization as the coupling of this particular model implementation with the optimization algorithm presented in Section 3.6 was straightforward in comparison with the other surrogate model implementations. The goal of this calibration is to identify the optimal uncertain simulation model parameters: $HTC_{filling}$, $HTC_{packing}$

Table 3.4 – The model and boundary condition parameters used in the default simulation and the ones obtained in the optimization use case.

Simulation	$HTC_{filling}$ (W/m^2°C)	$HTC_{packing}$ (W/m^2°C)	D_3 (K/MPa)
Default	5000	2500	0.076
Optimization	9520	3520	0.400

and D_3. The optimized parameters are summarized in Table 3.4 along with the default Moldflow® values for the $HTC_{filling}$ and $HTC_{packing}$ as well as the pressure-dependent viscosity parameter given in the Moldflow® material card (D_3) for the utilized POM material.

One of the main objectives of this optimization is the identification of material parameters or boundary conditions for enabling a more accurate estimation of the pressure field in a high-fidelity injection molding simulation. To show the impact of this parameter calibration, the experimental DoE is simulated using both the optimized parameters and the default parameters given in Table 3.4. The simulated pressure signals at the sensor location (taken from a surface node) are compared to the experimental pressure signals at that position. Four example DoEs are shown in Figure 3.12. In all cases, the simulation using the optimized parameters is closer to the experimental data than using the default parameters. The experimental setting showed in Figure 3.12a corresponds to V1 (refer to Table 2.6), for which the cavity was not filled completely (short shot) as seen in Figure 2.15a and both default and optimized simulations were not able to predict this event. This failure in the simulation can be related to the default solidification criterion, which defines the melt-to-solid transition at a constant temperature and oversimplifies the crystallization phenomena occurring in a wide range of cooling rates. In any case, the simulation results using the optimized parameters show more accurate pressure estimations during the packing phase as seen in Figures 3.12b and 3.12d. However, the estimation of the filling time and maximum pressure at the end of filling are less accurate than those obtained with default parameters. This issue is certainly due to the high value of the optimized pressure-dependent viscosity coefficient, which leads to higher viscosities and thus longer filling times. The prediction of the time when the pressure goes to zero is also prone to further improvement for both default and optimized simulations. This shortcoming should be also strongly related to the current simple solidification criterion.

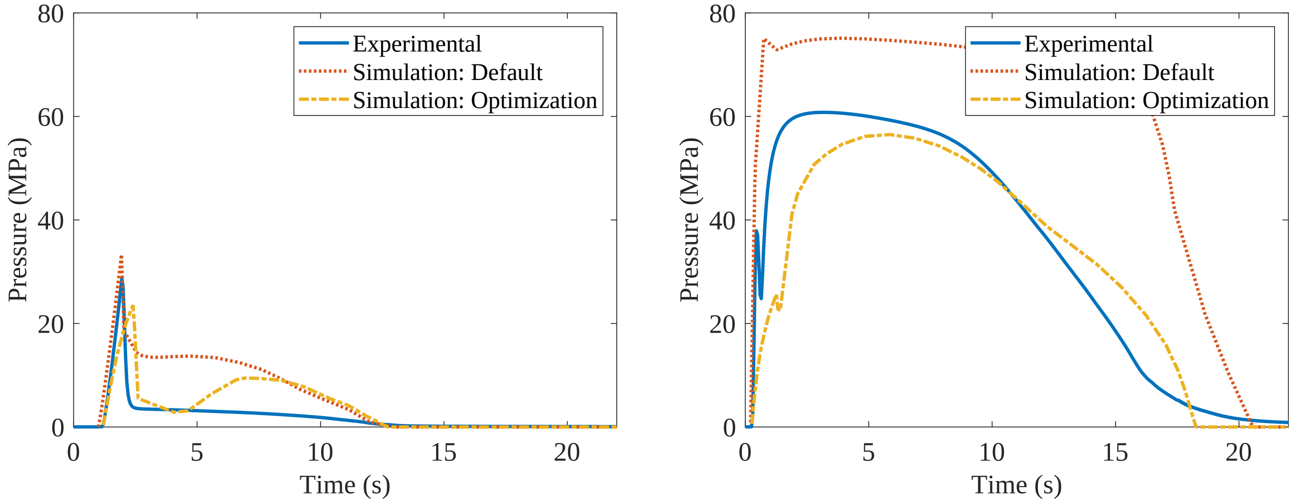

(a) V1 (b) V18

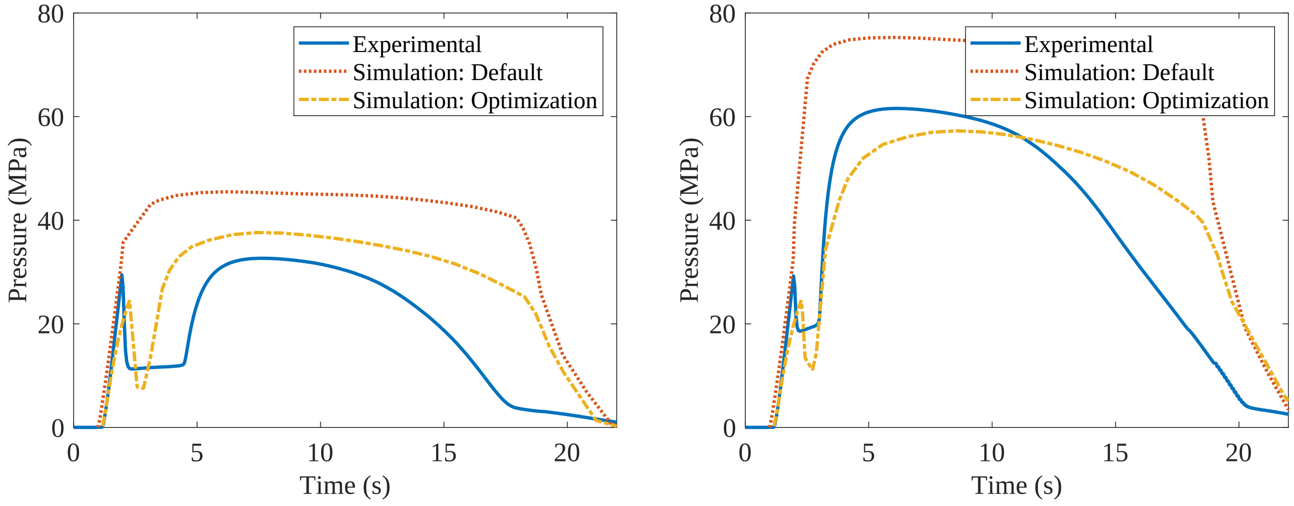

(c) V22 (d) V25

Figure 3.12 – Comparison between the experimental pressure signals and those obtained by the simulation using the default $HTC_{filling}$, $HTC_{packing}$ and D_3 values (Simulation: Default) and the optimized ones (Simulation: Optimization) for four example DoEs.

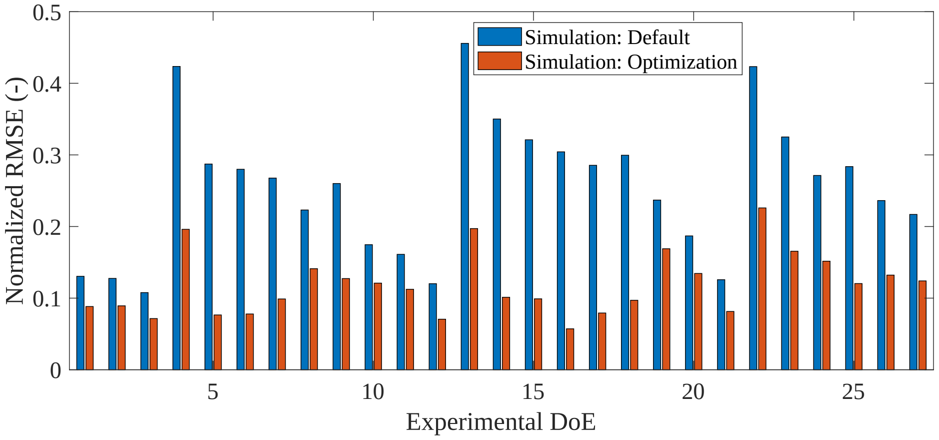

Figure 3.13 – RMSE of the simulated pressure results obtained using the default $HTC_{filling}$, $HTC_{packing}$ and D_3 values (Simulation: Default) and the optimized ones (Simulation: Optimization) for the 27 experimental DoEs.

The normalized RMSE comparing the pressure predictions using the default and optimized parameters for all 27 experimental DoEs are given in Figure 3.13. The use of the optimized parameters led to a huge decrease in the RMSE over all considered DoE cases. The simulation using default values exhibited for some cases errors around 40 % which are decreased by more than half while using the optimized parameters. However, both simulations are unable to recreate the short shots that were observed experimentally for the molding trials with a low injection velocity of 10 cm^3/s and a holding pressure of 20 MPa, as seen in Figure 3.12a. Since the optimized value for pressure-dependent viscosity parameter D_3 is found at the upper bound of the surrogate model generation range, it can indicate that the chosen intervals are insufficient or that the implemented models are intrinsically limited to mimic all physical phenomena during the injection molding process.

3.8 Conclusion

Surrogate models of high-fidelity simulations, where the variables are material-dependent parameters, offer an alternative to standard experimental identification methods, as shown for the case of injection molding in this feasibility study. The main aim of the method is the generation of an accurate surrogate model, which enables the reverse engineering of the material-dependent parameters using optimization techniques. Considering six independent variables, the POD-NLR and the regular-PCE-LS surrogate models exhibit basically the same performance especially when using a low number of training data. By increasing the number of training data, the adaptive-PCE-LS technique improves steadily the accuracy of the surrogate model and reaches a comparable performance with the fixed-DoE techniques for 120 training simulations. The advantages of the adaptive-PCE-LS should appear more evident when having a high number of variables.

Based on a Sobol sensitivity analysis using the generated surrogate model, we found that the heat transfer coefficient during filling has a low impact on the pressure evolution at a sensor node in front of the heat transfer coefficient during packing or the pressure-dependent viscosity coefficient. By optimizing the $HTC_{filling}$, $HTC_{packing}$ and the pressure-dependent viscosity model parameter D_3 using measured pressure signals, it was feasible to calibrate the high-fidelity simulation in order to decrease the deviations in the pressure estimation when compared to those obtained using default simulation values. However, there is still a gap for getting an accurate estimation of the pressure fields in injection molding, which could be closed with this methodology by including additional simulation model parameters in addition to a refinement of the models implemented in the simulation as shown in the next chapter by implementing a flow-induced crystallization model along with crystallization-dependent PVT, viscosity and solidification criterion for semi-crystalline thermoplastic polymers.

Chapter 4

Use of Surrogate Modeling for Calibrating a Flow-induced Crystallization Model in Moldflow

Content

4.1 Introduction

In the previous chapter, the feasibility of using surrogate modeling to identify three modeling parameters was studied. The study showed that it is possible to optimize these parameters using experimental pressure results with the help of a surrogate model representing the simulated pressure results at one surface node. Therefore, in this chapter, a similar methodology is followed in order to calibrate a flow-induced crystallization model along with crystallization-dependent PVT, viscosity and solidification models. These models are implemented in Moldflow® with the help of a user code. In total, three surrogate models are used to identify the five uncertain modeling parameters and these surrogates are generated using an analogous POD-NLR method as the one presented in Chapter 3. Such as the pressure signals are first reduced using the proper orthogonal decomposition technique followed by a least-squares regression of a second-order polynomial. This methodology is chosen as it exhibited a good performance when using a low number of training data and a low number of input parameters. After obtaining the optimized modeling parameters, the simulation performance is assessed by studying how well it is able to predict the pressure signals, filling status and skin layer thickness using the user-defined models in comparison to the experimental results. Additionally, the calibrated models are tested using three various mold geometries in order to check the generality of the identified parameters.

4.2 Description of the Implemented Models

4.2.1 Crystallization Model

The implemented crystallization model is a thermo-mechanical based model developed by Poitou et al. [17] in the framework of irreversible thermodynamics given by equation 1.26. This model is chosen since it takes into account both the flow-induced and quiescent crystallization in addition to having a limited number of parameters to identify. In Poitou et al.'s model [17], the crystallization's kinetics are modeled using a temperature-dependent function $\chi(T)$ defined by Hieber [66]. However, in this work, this relation is substituted by the Avrami kinetic constant which is proportional to the Avrami growth rate such as $k_{Avrami} \propto G^3$ making it possible to be described using the Hoffman-Lauritzen model and related to the previous function by $\chi(T) = 1/k_{Avrami}(T)^{1/n}$. Additionally, the β is considered a constant value to be determined and not dependent on temperature as presented in the original model. The crystallization model only applies for temperatures lower than the material's melting temperature $T_m(P)$ and can be rewritten as follows for $T < T_m(P)$:

$$\dot{\alpha}(t) = (1-\alpha)\left[-\frac{1}{\beta}\frac{\partial\eta}{\partial\alpha}\mathrm{tr}\mathbf{D}^2 + nk_{Avrami}(T)^{\frac{1}{n}}\left(-\ln(1-\alpha)\right)^{1-\frac{1}{n}}\right], \tag{4.1}$$

$$k_{Avrami}(T) = K_0 \exp\left(-\frac{3K_g}{T(T_m^0(P)-T)}\right)\exp\left(-\frac{3U^\star}{R(T-T_\infty(P))}\right) \tag{4.2}$$

where β, n, K_0 and K_g are data-fitted parameters, $\mathbf{D}$ is the strain rate tensor, $T_m^0(P)$ is the pressure-dependent equilibrium melting temperature, $U^\star$ is the activation energy for segmental jump of polymer molecules with a universal value of 6270 J/mol, R is the gas constant and $T_\infty = T_g(P) - 30$ with $T_g(P)$ as the pressure-dependent glass transition temperature. The first term in equation 4.1 represents the contribution of the flow-induced crystallization to the relative crystallinity evolution $\dot{\alpha}$ by computing the viscosity derivative in respect to the relative crystallinity α represented by $\frac{\partial\eta}{\partial\alpha}$. Whereas the second term in equation 4.1 is the contribution of the quiescent crystallization to $\dot{\alpha}$.

In order to reduce the number of model parameters, a linear relation is deduced between the kinetic constants of the Hoffman-Lauritzen equation for the used POM material such as:

$$K_g = 6732\ln(K_0) + 11296. \tag{4.3}$$

This dependency is obtained by fitting equation 4.2 to the Avrami kinetic constant calculated using the Avrami-Ozawa relation which relates the kinetic constants of both models using:

$$k_{Avrami}(T) = \left[-\frac{d}{dT}\left(k_{Ozawa}(T)^{1/n}\right)\right]^n \tag{4.4}$$

where n is the Avrami exponent with a typical value of 3 representing instantaneous nucleation, same parameter as in equation 4.1. In this work, since the DSC measurements presented in Section 2.2 are performed under non-isothermal conditions, k_{Ozawa} is first calculated under these conditions and following that the k_{Avrami} is obtained using equation 4.4.

Additionally, the pressure dependencies of the temperatures are defined by:

$$T_m(P) = T_m(0) + b_6 P, \tag{4.5}$$

$$T_m^0(P) = T_m^0(0) + aP, \tag{4.6}$$

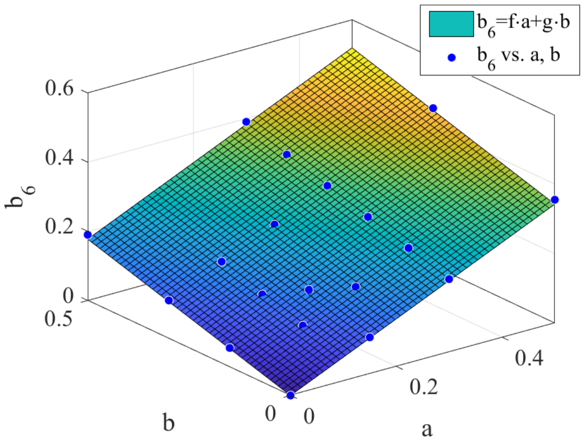

Figure 4.1 – Fitting surface relating the different pressure dependencies of the melting temperature (b_6), equilibrium melting temperature (a) and glass transition temperature (b).

$$T_g(P) = T_g(0) + bP \tag{4.7}$$

where b_6, a and b are usually experimentally-determined parameters. The pressure dependency of the melting temperature b_6 is typically obtained from PVT measurements. However, the two other dependencies are harder to determine experimentally for semi-crystalline materials. Therefore, for this work, a relation between the three parameters is proposed by computing the crystal growth curves as function of temperature for different pressure levels using the Hoffman-Lauritzen model given in equation 4.2. For various combinations of a and b, the maximal growth rate is determined for the different pressures and the corresponding temperatures are used to calculate b_6. Figure 4.1 shows the surface representing the relation between the dependencies such as:

$$b_6 = f \cdot a + g \cdot b \tag{4.8}$$

where $f = 0.629$ and $g = 0.4015$ are the obtained fitted parameters. The melting temperature and the equilibrium melting temperature are assumed to have the same pressure dependency such as $b_6 = a = 0.175$ K/MPa (value obtained from material's supplier). As for the dependence of the glass transition temperature, it can be deduced using equation 4.8 and found to be $b = 0.161$ K/MPa.

Table 4.1 – The model parameters of the implemented crystallization model.

Model Parameter	**Value (units)**
n	3 (-)
$U^\star$	6270 (J/mol)
$T_m^0(0)$	199.7 (°C) [124]
$T_m(0)$	178.9 (°C)
$T_g(0)$	-73.0 (°C) [113]
b_6	0.175 (K/MPa)
a	0.175 (K/MPa)
b	0.161 (K/MPa)

Table 4.2 – Material characteristics of the studied POM homopolymer obtained from the DSC measurements.

Melting Temperature, $T_m(0)$	**Crystallization Enthalpy**, ΔH_c
178.9 °C	155.35 J/g

4.2.1.1 Heat Source

As the polymer experiences a phase change while crystallizing, heat is released into the system, otherwise known as the latent heat of crystallization. Therefore, an additional heat source is defined that expresses the temperature increment ΔT as a function of crystallization such as:

$$\Delta T = \dot{\alpha}(t)\Delta t \frac{\Delta H_c}{c_p} \tag{4.9}$$

where Δt is the time step, ΔH_c is the crystallization enthalpy and c_p is the specific heat. If the temperature of the melt is higher than the material's melting temperature ($T > T_m(P)$), remelting of the crystals takes place leading to a negative $\Delta T = -\alpha \frac{\Delta H_c}{c_p}$.

The crystallization enthalpy is given in Table 4.2. As for the specific heat, it is typically defined using Moldflow$^{\circledR}$ material cards as a function of temperature including a crystallization peak. However, since in this implementation a crystallization-dependent a heat source is included, the specific heat is defined using a linear relation of the values presented in Table 4.3.

Table 4.3 – The specific heat data used in the Moldflow simulations along with self-defined models.

Temperature (°C)	**Specific Heat** ($\mathrm{J\,kg^{-1}\,K^{-1}}$)
32	1286
220	1932

4.2.2 Viscosity Model

A modified Cross-WLF model is used to describe the viscosity in this implementation. This model takes into account the crystallization dependency in addition to the temperature, shear rate and pressure dependencies of the viscosity. The melt viscosity η is given by:

$$\eta(T, P, \alpha, \dot{\gamma}) = \frac{\eta_0(T, P, \alpha)}{1 + (\frac{\eta_0(T,P,\alpha)\dot{\gamma}}{\tau^\star})^{1-\lambda_v}} \tag{4.10}$$

where $\dot{\gamma}$ is the shear rate, $\tau^\star$ is the critical stress level at the transition to shear thinning, λ_v is the power law index in the high shear rate regime and η_0 is the zero shear viscosity defined as:

$$\eta_0(T, P, \alpha) = D_1 \exp\left(\frac{-A_1(T - T_{ref})}{A_2 + (T - T_{ref})}\right) \vartheta(\alpha) \tag{4.11}$$

where $T_{ref} = T_g(P)$ with a pressure-dependency defined in equation 4.7 and D_1, A_1 and A_2 are data-fitted coefficients. As for $\vartheta(\alpha)$, it is a function describing the crystallization-dependency of the viscosity and is an extension of Kitano et al.'s relation [67] for concentrated suspension of particles. This function is defined as:

$$\vartheta(\alpha) = \frac{1}{(1 - \frac{\alpha}{A})^B} \tag{4.12}$$

where A represents the maximum relative crystallinity reached by the material before it solidifies and B is a data-fitted exponent. This coupling function differs from the one defined in equation 1.27 since the function $\vartheta(\alpha) = \eta_0(T, P, \alpha)/\eta_0(T, P)$. This choice is made to increase the effect of crystallization on viscosity at low shear rates as done by Pantani et al. [15].

By excluding the crystallization-dependency $\vartheta(\alpha)$, this Cross-WLF model still differs from the one implemented by default in Moldflow®, shown in Appendix A, since the A_2 coefficient is not dependent on pressure in this implementation. Including this dependency as done in default Moldflow® leads to a linear relation between η_0 and P for all temperatures. However, Rudolph et al. [125] showed a non-linear dependency between them for low temperatures approaching the glass transition temperature

Table 4.4 – The model parameters of the implemented viscosity model.

Model Parameter	**Value (units)**
λ_v	0.1608 (-)
$\tau^\star$	398 000 (Pa)
D_1	5.55×10^{13} (Pa.s)
A_1	26.596 (-)
A_2	28.875 (K)

of a polycarbonate material. Therefore, in this work, the main connection between the viscosity and pressure is modeled using the glass transition temperature's dependency.

To identify the parameters of the WLF model, the dynamic temperature ramp test performed at a constant frequency of 3 rad/s and a 0.03 % strain with a heating/cooling rate of 3 °C/min shown in Figure 2.7 is used. The viscosity results before the onset of crystallization at 152.4 °C are utilized to determine the temperature dependency of the viscosity by fitting the following linear relation:

$$\frac{1}{\ln(\eta^\star/D_1)} = -\frac{A_2}{A_1}\frac{1}{(T - T_{ref})} - \frac{1}{A_1} \tag{4.13}$$

where $\eta^\star$ is the measured complex viscosity from the rheological test. Additionally, to describe the shear rate dependency of the viscosity using the Cross model given in equation 4.10, Moldflow®'s material database is used. The model parameters for the Cross-WLF model are summarized in Table 4.4.

4.2.3 PVT Model

Since this work deals with a semi-crystalline thermoplastic material, the Pressure-Volume-Temperature (PVT) model is defined in relation to the relative crystallinity α. For these purposes, a simple two-phase system is assumed. This makes it possible to describe the specific volume v using a mixing law of the molten and solidified phases' specific volumes, represented respectively as v_m and v_s. This law is written as:

$$v = \alpha v_s + (1 - \alpha) v_m. \tag{4.14}$$

The specific volumes v_m and v_s are described using the empirical Tait equation given in equations 1.29 to 1.31. The PVT model parameters are taken from Moldflow®'s material database for POM and are

Table 4.5 – The model parameters of the implemented PVT model.

Model Parameter	**Value (units)**
b_{1m}	8.452×10^{-4} (m^3/kg)
b_{2m}	5.65×10^{-7} (m^3/kgK)
b_{3m}	$1.570\,79 \times 10^{8}$ (Pa)
b_{4m}	7.667×10^{-3} (1/K)
b_5	448.15 (K)
b_{1s}	7.446×10^{-4} (m^3/kg)
b_{2s}	2.944×10^{-7} (m^3/kgK)
b_{3s}	$2.876\,63 \times 10^{8}$ (Pa)
b_{4s}	4.784×10^{-3} (1/K)

summarized in Table 4.5.

4.2.4 Solidification Model

A solidification criterion is used in an injection molding simulation to determine whether the polymer is solidified or still flowing. This is usually defined by a no-flow temperature characteristic to a material. However, the solidification of the material is highly dependent on the crystallization degree present in it. Therefore, in this implementation, a crystallization-dependent solidification model is utilized such as:

- if ($\alpha > A$): solidified polymer

- if ($\alpha < A$): flowing polymer

where A is the same parameter used to describe the dependency of the viscosity on crystallization using the function given in equation 4.12.

Table 4.6 presents a summary of the implemented models in comparison to the ones used by the default Moldflow® solver.

Table 4.6 – Comparison between the implemented models and the ones used by default in a Moldflow simulation for the injection molding of a semi-crystalline thermoplastic material.

Modeling	Default Moldflow®	Proposed Implementation
Crystallization	Not included	Poitou et al. [17] thermo-mechanical model: FIC & quiescent crystallization
Viscosity	Cross-WLF model without crystallization dependency and a linear pressure dependency	Modified Cross-WLF model with crystallization coupling and a non-linear pressure dependency
PVT	2-domain Tait model with a transition temperature linearly dependent on pressure	Tait model coupled with crystallization and pressure
Heat Source	Not included	Heat created due to crystallization and removed due to remelting of crystals

4.3 Implementation in Moldflow using Solver API

4.3.1 Solver API Feature

The Solver Application Programming Interface (API) in Moldflow® enables the user to create their own C++ functions which the solver can call to calculate a property during an analysis. In AMI2021.1, this feature allows user-defined models for viscosity, PVT, core shift, solidification and fiber orientation. Additionally, due to the newly-introduced Advection API functionality, it is possible to define material derivatives that are solved in time and space by the solver while providing the user's code access to the solution of the derivative(s).

To be able to use the Solver API feature, a shared library object needs to be compiled and copied into the binary directory of the AMI installation folder. The project should be compiled with all the header and C++ files needed to get a successful run when the Solver API option is enabled in Moldflow®. Most importantly, this should include the header files defining the user and utility functions which represent the main link between Moldflow®'s solver and the user's code:

- Utility functions are functions that are already defined inside the Moldflow® solver which can be called by the user's code. They are used in order to gain access to information available to the solver during an analysis or to perform specific actions.

- User functions are defined by the user's own code and are called by the solver during an analysis when needed. Function calls depend on the options selected in the Solver API window in the process settings of the current running study. Called functions need to be defined in the compiled shared library file or the solver will exit with failure.

4.3.2 Implementation Code

The models presented in Section 4.2 are implemented using a C++ code in a Visual Studio project. This project file includes a class for each user-defined model in which the class member functions are used by the main source file to calculate the viscosity, crystallization and specific volume. The main source file plays a major role in the implementation of the various models using the Solver API feature as it defines the user functions called by the solver during an analysis. The structure of this file resembles any other source file, it begins with #include directives which are read and interpreted by the preprocessor when the Visual Studio project is compiled. In this work, the following C++ Standard Library headers are used:

- input/output library: <iostream>, <sstream>, <fstream>,
- error handling: <cassert>,
- numerics library: <cmath>, <math.h>.

To be able to obtain the relative crystallinity α at a specific node in the simulation at time t, the crystallization model equation given by equation 4.1 needs to be solved in time and space. This is possible using the new Solver API advection functionality through the new user functions recognized as *UserNodeFields*. The user's code can access the integration results of the defined equation using the *GetUserNodeField* utility function.

In total, five main user functions are defined in the C++ code to compute:

- relative crystallinity: *SolverUserHb3dUserNodeFieldsEvolution*,
- viscosity: *SolverUserHb3dViscosityAtNode*,
- specific volume: *SolverUserHb3dSpecificVolumeAtNode*,
- heat generation/loss: *SolverUserHb3dTemperatureIncrementAtNode*,

- solidification criterion: *SolverUserHb3dSolidificationAtNode*.

These functions necessitate access to the model parameters, this is done by defining the path of the text files containing these parameters in the Moldflow® simulation. Example codes for these functions can be found in the installed directory folder of Moldflow® Insight and code explanations on the Autodesk website [126].

To sum up, the flowchart presented in Figure 4.2 is provided as an overview of the implemented code which is compiled to a shared library file in the form of a dynamic-link library (DLL) to be used during the various Moldflow® simulation runs presented in this chapter.

4.3.3 Simulation Environment

Similarly to the simulation model used in Chapter 3, the half length 3 mm thick geometry is again used to perform the simulation runs in this implementation. The 3D meshed model along with the feed system and cooling channels are presented in Figure 3.1. For the material data, the POM material card from Moldflow®'s database is edited to have a linear specific heat relation with temperature as given in Table 4.3. The process settings of the base simulation are similarly defined using imported data from the ENGEL sim link software tool.

Additionally, since in this work multiple user-defined models are implemented, the Solver API option should be enabled as well as selecting a user-defined viscosity, PVT and solidification models. Since the crystallization model is defined using the Advection functionality, it does not have its own drop-down option but if the *SolverUserHb3dUserNodeFieldsEvolution* user function is compiled in the code it will be taken into account. For the model parameters, text file paths need to be provided by the user in the parameter text strings in Process Settings > Advanced options... > Solver API window in Moldflow®.

In this implementation, a single simulation requires around 110 minutes to be completed on a workstation with a 4.10 GHz processor and 32 GB RAM. In order to generate the different surrogate models, the automation utilities available in Moldflow® are utilized to run efficiently the multiple simulations needed, refer to Section 3.2.1 for more information concerning this topic.

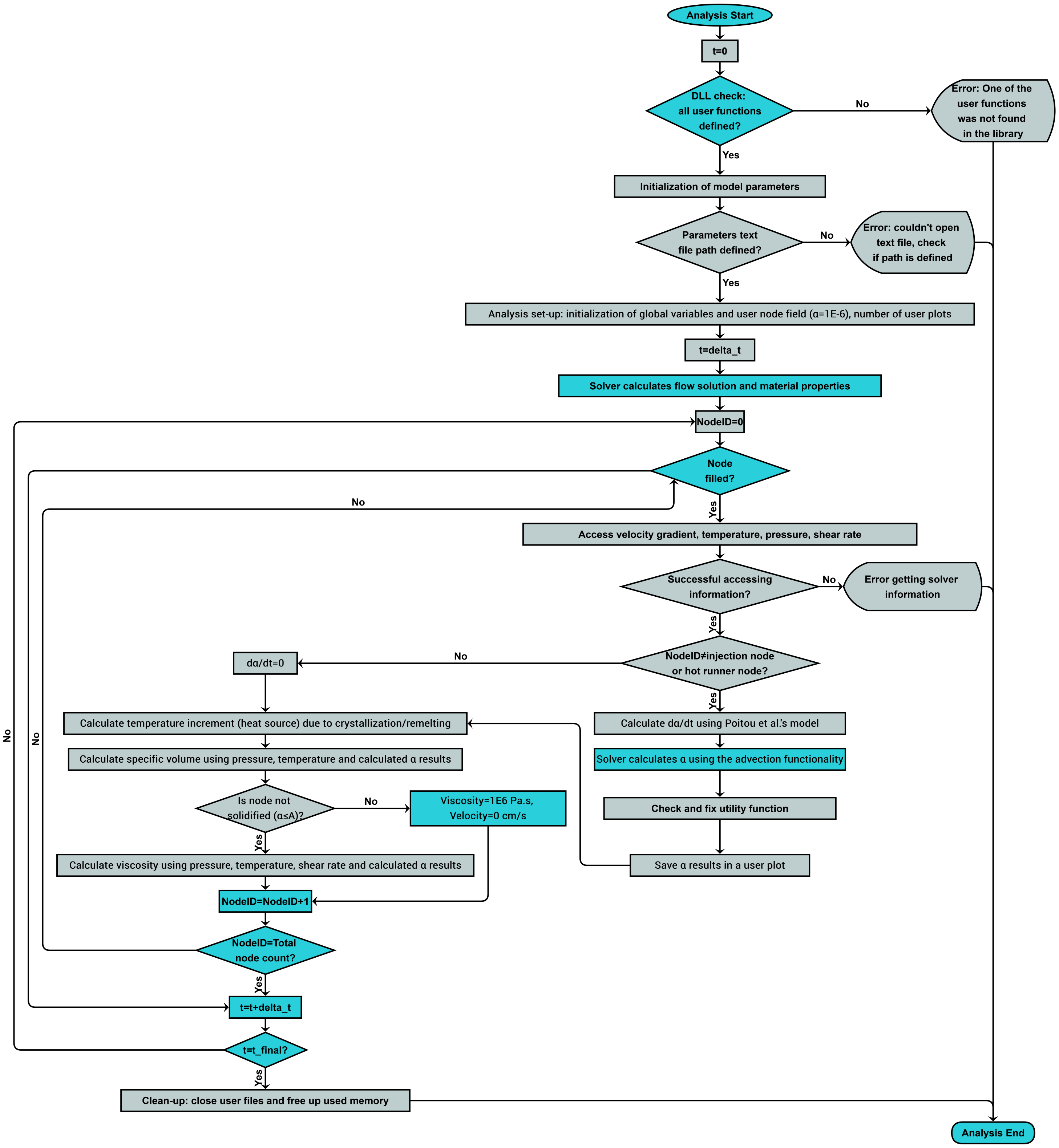

Figure 4.2 – Flowchart representing the link between the Moldflow solver (turquoise nodes) and the implemented C++ code used to define the user models (gray nodes), DLL=Dynamic-link library.

Table 4.7 – The process settings used in the basis simulations for the three generated surrogate models.

Experimental DoE Name	**Surrogate Model Name**	$T_{c,in}$ (°C)	V_{inj} (cm^3/s)	P_{hold} (MPa)
V6	SM1	84	50	50
V14	SM2	99	30	50
V27	SM3	114	50	80

Table 4.8 – The surrogate model variables with their upper and lower bounds.

Surrogate Model Variables (units)	**Lower Bound**	**Upper Bound**
β (Pa^{-1} s^{-1})	-10^{12}	-10^{10}
$\ln(K_0)$ (-)	23	83
A (-)	0.3	0.6
B (-)	2	5
HTC_p (W m^{-2} °C^{-1})	500	5000

4.4 Surrogate Models

4.4.1 Input Variables and Output

A total of three surrogate models are generated for three different processing conditions corresponding to the ones used during the experimental injection molding runs. These process settings are presented in Table 4.7 along with the surrogate model's name according to which experimental DoE it represents. For each surrogate model, five input parameters are varied: two crystallization model parameters (β, K_0), two viscosity model parameters (A, B) and the heat transfer coefficient (HTC_p) used during the packing analysis. These inputs are summarized in Table 4.8 along with their lower and upper limits.

Some of these ranges were determined with the help of heuristics while others are based on experimental results. For K_0, the DSC data obtained from the measurements presented in Section 2.2 are used. Since only a couple of cooling rates were utilized for these measurements, the temperature range covered is limited making it difficult to obtain one constant value for K_0. Therefore, it is part of the surrogate model variables and the range fits the six data points calculated using the Avrami-Ozawa relation given in equation 4.4 and is centralized at $ln(K_0) = 53$; a value determined by Plummer and Kausch [127] for POM. As for the solidification criterion A, in the case of $B = 2$, the viscosity coupling is analogous to the one given by Metzner [68] where he specified $A = 0.68$ for smooth spheres and $A \approx 0.44$ for rough compact crystals. Therefore, for this implementation, since there should exist spherical and thread-like morphologies during injection molding, we postulate a rough ± 0.15 to the value given for compact crystals. As for the B viscosity exponent parameter, Kitano [67] and Metzner [68] defined it to be equal to 2 according to suspension theory. However, the B is varied between 2 and 5 in order to take into account the sudden increase in the POM viscosity as it starts to crystallize as already seen in Figure 2.7 during the dynamic temperature ramp tests.

The β parameter has a strong effect on the contribution of the flow-induced crystallization to the total relative crystallinity in the part, therefore, this parameter interval was not straightforward to define as its high value can lead to short shots due to the fast solidification of the thin gate. Nevertheless, the β interval was assumed after performing multiple sensitivity studies and generating some test surrogate models in order to obtain a DoE that produces a representative amount of short shots and fully filled parts in order to efficiently calibrate the parameters later on using the optimization routine.

The output result used to train the surrogate models is the pressure signal at a surface node corresponding to the location of the second sensor P2 located directly after the gate shown in Figure 2.9.

4.4.2 Generation Methodology

A Latin Hypercube sampling method is chosen to generate the surrogate models. The number of runs chosen for the training of the models is 132 simulations and for the testing is 20 simulations. This choice is postulated to be appropriate as five parameters are being varied in this implementation in comparison to the six parameters changed in the feasibility study performed in Chapter 3 where it was shown that the pressure predictions are highly accurate using 120 training simulations.

The generation of the three surrogate models is done in MATLAB R2019b using an analogous POD-NLR methodology to that presented in Section 3.4.1. However, in this implementation, the following differences exist:

1. *Pre-processing*: the pressure results P_i $(i = 1, \cdots, S)$ are differently pre-processed as in Section

3.4.1. In this implementation, the original time series are normalized between 0 and 1 according to the determined t_{start} and t_{end} by:

$$t_{norm} = \frac{t_{original} - t_{start}}{t_{end}} \tag{4.15}$$

where $t_{original}$ is the imported unprocessed simulation time, t_{start} represents the time at which the flow front reaches the sensor node and produces a non-zero pressure signal and t_{end} is the time at which the pressure signal goes to zero at the end of the packing stage. This normalization step is followed by the resampling of the pressure data using a common time vector from 0 to 1 s with 0.001 s time steps.

2. *Model order reduction*: the POD basis functions ϕ are calculated similarly as in Section 3.4.1 using equation 3.1. The only difference is that in this study a truncation error value of $\epsilon = 5 \times 10^{-4}$ is used.

3. *Model fitting*: a least-squares regression of a second-order polynomial is used to train a model to predict the POD parameters Γ, the time shift values t_{start} and t_{end}. The first two are determined using equations 3.2 and 3.3, respectively, with $i = j$. Whereas, t_{end} is determined as follows:

$$t_{end}^{(s)} = g + h_i X_i^{(s)} + z_{ij} X_i^{(s)} X_j^{(s)} \tag{4.16}$$

where X_i and X_j are the surrogate model input variables with $i = j$ representing the number of variables $(1, \cdots, 5)$ and g, h, z are additional surrogate parameters to those present in equations 3.2 and 3.3. The implicit Einstein summation convention is used for indexes i and j in equation 4.16.

4.5 Calibration Algorithm

To identify the five modeling parameters presented in Table 4.8, a multi-objective optimization routine is performed using the *lsqnonlin* built-in MATLAB function from the optimization toolbox. The experimental pressure signals are used as reference results. The performed optimization utilizes

Table 4.9 – The experimentally-determined parameters used to define the six objective functions used in the optimization routine to identify the modeling parameters.

k	$Y_{max}^{exp,k}$ (MPa)	$t_{end}^{exp,k}$ (s)
6	38.09	12.8
14	35.25	15.2
27	63.65	20.47

all three surrogate models to obtain one set of optimized parameters using the following formulation:

$$\begin{aligned}
\text{find} \quad & \mathbf{V} = (\beta, K_0, A, B, HTC_p) \\
\text{argmin} \quad & |\hat{Y}_{max}^{l} - Y_{max}^{exp,k}| \quad (l = 1,2,3 \ \& \ k = 6,14,27) \\
& |\hat{t}_{end}^{l} - t_{end}^{exp,k}| \\
\text{s.t.} \quad & -10^{12} \leq \beta \leq -10^{10}, \\
& 23 \leq \ln(K_0) \leq 83, \\
& 0.3 \leq A \leq 0.6, \\
& 2 \leq B \leq 5, \\
& 500 \leq HTC_p \leq 5000.
\end{aligned}$$

In total, the optimization consists of six objective functions. Three of them are minimizing the difference between the maximum pressure value obtained experimentally $Y_{max}^{exp,k}$ where $k = 6, 14, 27$ represents the experimental DoE number (V6, V14, V27) and that predicted by the corresponding surrogate model $\hat{Y}_{max}^{l}$ with $l = 1, 2, 3$ the number of the surrogate model (SM1, SM2, SM3). The other three objective functions are minimizing the difference between the predicted $\hat{t}_{end}^{l}$ defined using equation 4.16 and the experimentally-determined $t_{end}^{exp,k}$. This value is obtained by fitting a tangent line to the decreasing pressure slope during the end of packing and checking the intercept with the x-axis of that line. This method is used to not take into account the probable over-compacting that was observed experimentally in Figure 2.13 at the end of packing and discussed in Section 2.4.4 since in the simulation it was not possible to recreate this. Table 4.9 summarizes the experimental values used to define the six objective functions.

4.6 Results and Discussion

4.6.1 Surrogate Models Performance

The performance of each generated surrogate model is assessed according to how well it is able to recreate the full pressure signal results of the high-fidelity simulation at one sensor location. Therefore, in this section, we present some example predicted pressure results from both the training and testing DoE sets as well as the error metrics of the POD parameters and time shifts obtained using the trained surrogate model, in other words, using the fitted polynomials defined by equations 3.2, 3.3 and 4.16.

The error metrics presented in this chapter are the normalized RMSE defined in equation 3.5 and the coefficient of determination also known as the R^2 score. It is a statistical measure that indicates how well the data fit the regression model and how well the unseen samples are likely to be predicted by the model. The best score is 1.0 and has a range between $-\infty < R^2 \leq 1$. A value far from 1 means that the surrogate model response $\hat{Y}$ is unable to predict accurately the true output results Y. R^2 is calculated as follows:

$$R^2(Y, \hat{Y}) = 1 - \frac{\sum_{i=1}^{n}(Y^i - \hat{Y}^i)^2}{\sum_{i=1}^{n}(Y^i - \bar{Y})^2} \tag{4.17}$$

where $\bar{Y} = \frac{1}{n}\sum_{i=1}^{n} Y^i$ is the mean value of Y.

In order to support the presentation of the previously-mentioned results, the POD basis functions of each surrogate model are presented in Figure 4.3. The SM1 and SM2 models are reduced using five basis functions whereas the SM3 model is reduced using only three. The reason behind this difference is the use of the same truncation error ϵ for all models. Additionally, since the pressure signal for the V27 process settings is less complex than the one for V6 and V14, the SM3 model necessitates less basis functions to represent it.

Starting off by the SM1 surrogate model, Figure 4.4a presents the pressure results of four training simulations and the approximated results for these same simulations obtained by the model after its training. Even though the model is trained using these simulations, there still exists some discrepancy between the model predictions and that of the simulation especially in the case of the green curve. These differences are expected since a non-interpolation technique is used to train the model as the signal is first reduced using POD and then its parameters are fitted to generate the final model. It is also clear that the form of the pressure result in the case of the green curve is different than the other

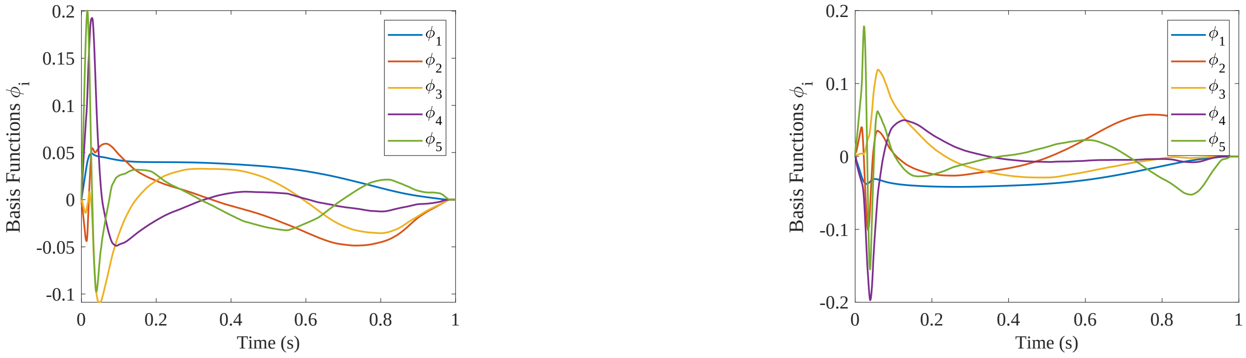

(a) SM1 (b) SM2

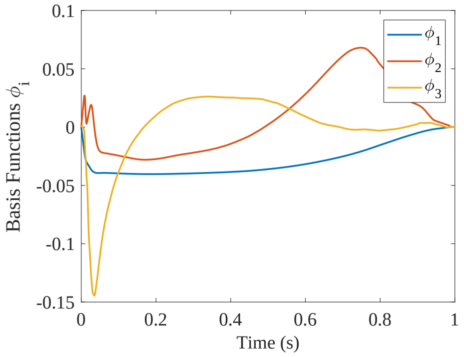

(c) SM3

Figure 4.3 – The POD basis functions of the three generated surrogate models.

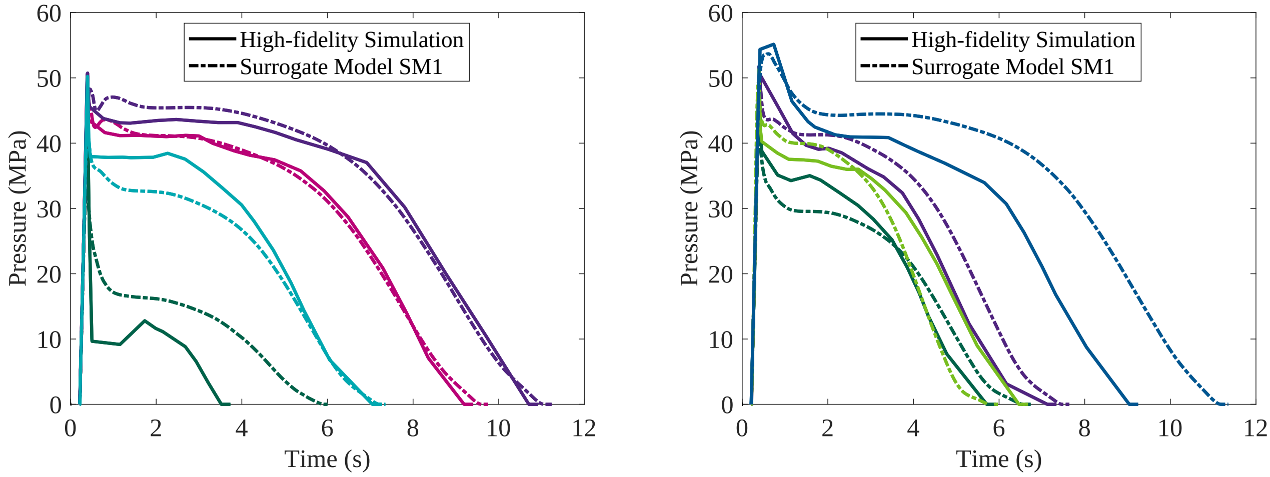

(a) Training: SM1 (b) Testing: SM1

Figure 4.4 – Comparison between the pressure predictions using the SM1 surrogate model and those obtained by four example high-fidelity simulations used for the model's (a) training and (b) testing.

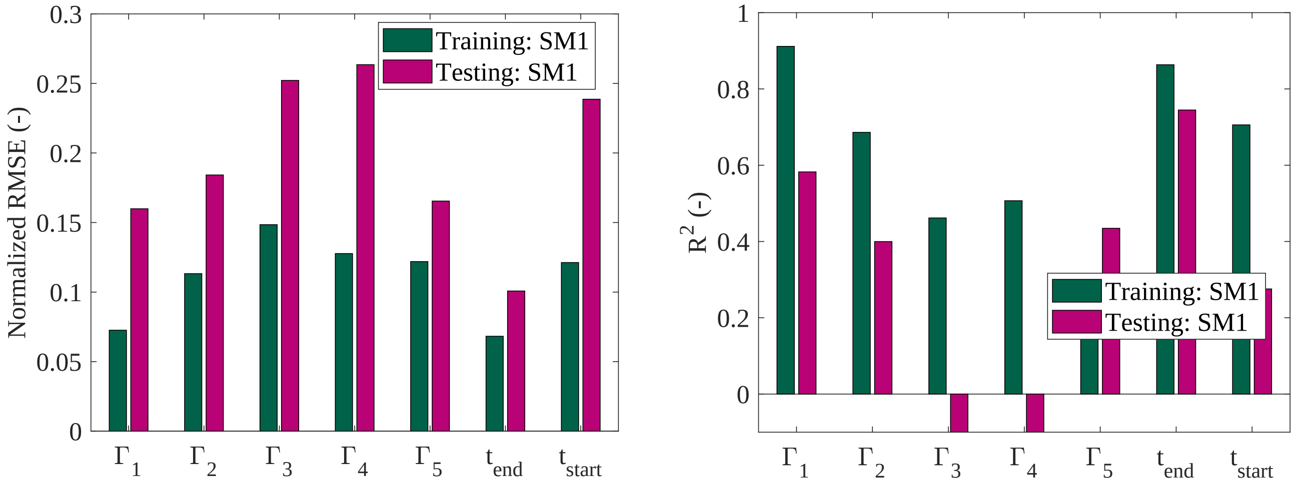

(a) Root mean square error

(b) Coefficient of determination

Figure 4.5 – The error metrics of the calculated POD parameters Γ and time shifts t_{start} and t_{end} using the SM1 surrogate model when using input data from the training and testing sets.

three curves making it more challenging to obtain a well-fitted model. Figure 4.4b shows the pressure signals of four simulations used to test the model in comparison to the pressure results obtained by the fitted model. It is apparent that the model is able to recreate the form of the pressure signal. However, it still struggles for some cases to accurately predict the time shift t_{end} as seen in the curve represented in dark blue.

Since it is difficult to compare visually all the training and testing prediction results, the error metrics for the five POD Γ parameters and time shift parameters are calculated and presented in Figure 4.5. Figures 4.5a and 4.5b show the RMSE and R^2 score, respectively, of these parameters obtained during the training and testing steps of the SM1 surrogate model. The parameter errors for the training set are, as expected, lower than those obtained for the testing set. Using unseen input data on the trained SM1 model doubles the RMSE of the POD parameter Γ_1 and Γ_4 as well as the time shift t_{start}. Overall, the surrogate model's parameters are predicted with a RMSE lower than 26 % which is considered for these purposes as acceptable. By analyzing the coefficient of determination results, the calculated Γ_3 and Γ_4 parameters by the fitted surrogate model produce a negative R^2 score for the testing set pointing that the chosen regression is not a good fit for the parameters in question.

Moving on to the SM2 model, Figure 4.6 provides four examples of the pressure predictions using the SM2 model in comparison to those obtained by the high fidelity simulation from both the training and testing sets. At the first glance, there is some minor differences between the predictions and the

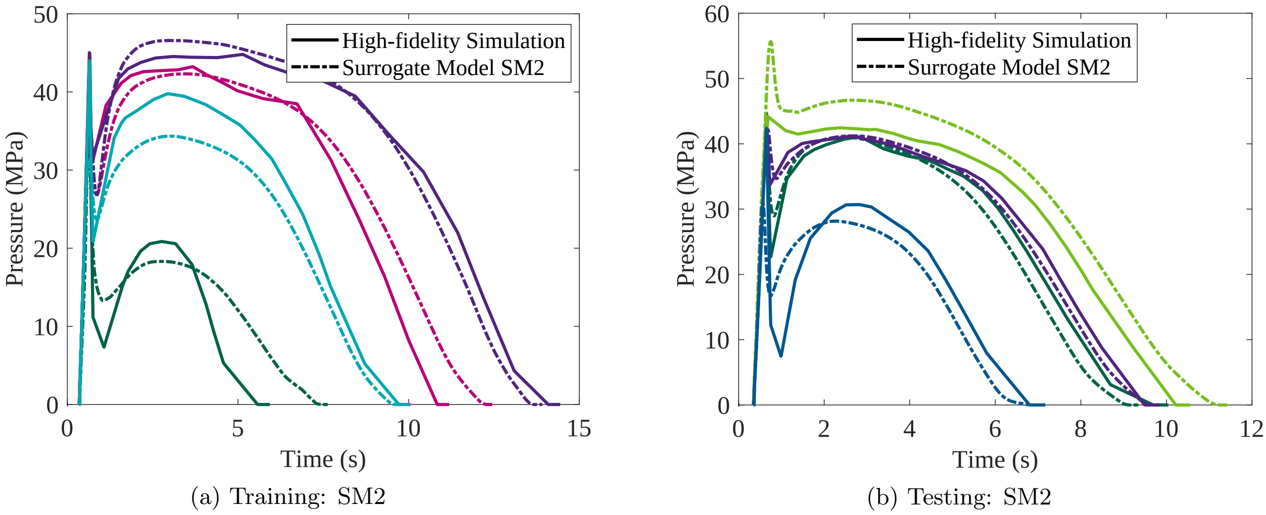

(a) Training: SM2 (b) Testing: SM2

Figure 4.6 – Comparison between the pressure predictions using the SM2 surrogate model and those obtained by four example high-fidelity simulations used for the model's (a) training and (b) testing.

reference simulation results. For the training simulations, the amplitude of the pressure during packing in the turquoise curve is under-predicted whereas for the time shift t_{end} in the green and pink curves is over-predicted. As for the testing simulations, it seems that the SM2 model is performing very well on the four presented examples in Figure 4.6b. This is confirmed by analyzing the error metrics given by Figure 4.7 where the overall RMSE for all parameters is lower than 0.2. Additionally, there is very minimal difference between the model's ability in predicting seen and unseen data when comparing the error between the training and testing results.

As for the SM3 model, Figures 4.8a and 4.8b present some example pressure results using the generated model in comparison to those obtained using the high-fidelity simulations with training input data and testing ones, respectively. The shown examples highlight a good model accuracy in general. The maximum pressure during packing in the two training simulations represented in green and turquoise in Figure 4.8a is under-predicted by the model. Whereas, the presented testing simulations are well predicted. For this model, it was sufficient to reduce the pressure signals with only three POD modes to satisfy the truncation error of $\epsilon = 5 \times 10^{-4}$ as shown in Figure 4.3c. Therefore, the error metrics given by Figure 4.9 include three Γ POD parameters. The model seems to perform very well in recreating the training data as the RMSE is lower than 12 % for all parameters. However, it is apparent that the third POD parameter Γ_3 is inaccurately represented by the fitted polynomial

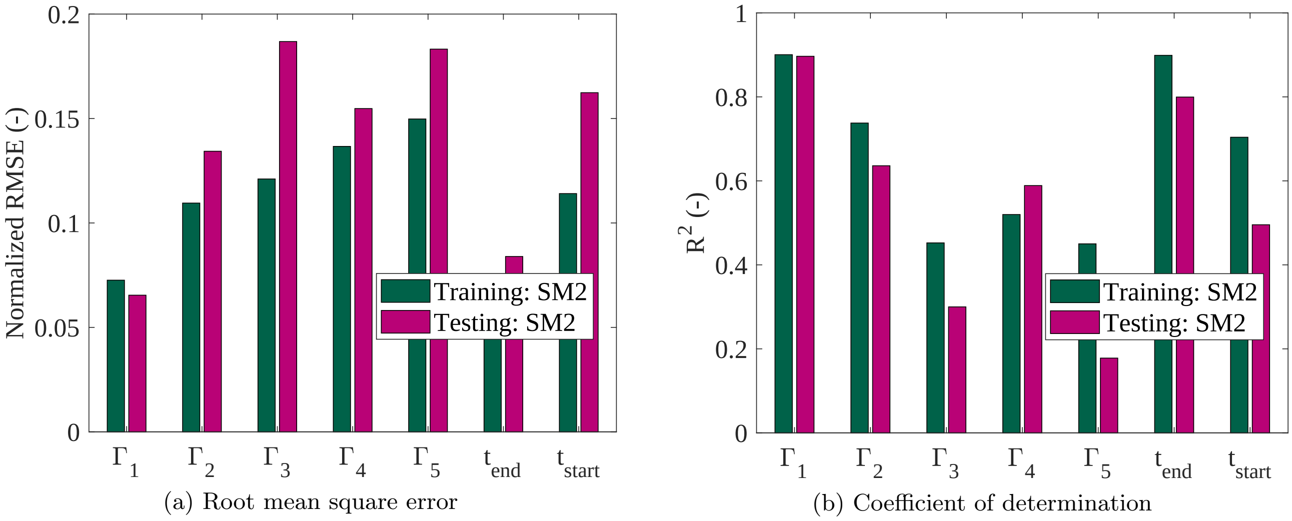

(a) Root mean square error

(b) Coefficient of determination

Figure 4.7 – The error metrics of the calculated POD parameters Γ and time shifts t_{start} and t_{end} using the SM2 surrogate model when using input data from the training and testing sets.

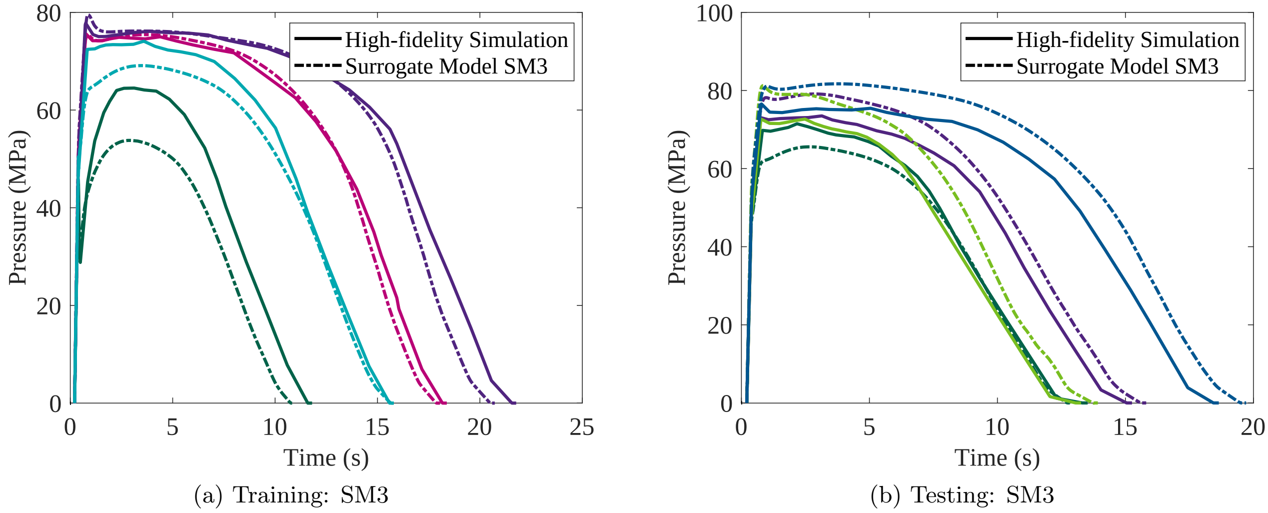

(a) Training: SM3

(b) Testing: SM3

Figure 4.8 – Comparison between the pressure predictions using the SM3 surrogate model and those obtained by four example high-fidelity simulations used for the model's (a) training and (b) testing.

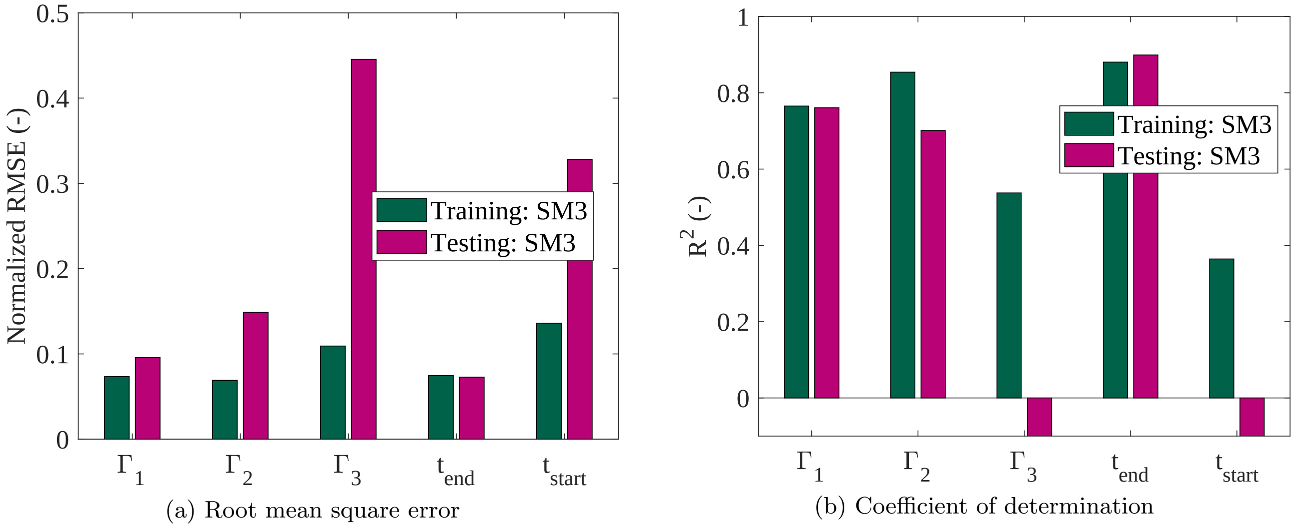

(a) Root mean square error

(b) Coefficient of determination

Figure 4.9 – The error metrics of the calculated POD parameters Γ and time shifts t_{start} and t_{end} using the SM3 surrogate model when using input data from the training and testing sets.

function representing the surrogate model as it performs badly using unseen input data during testing. This is also highlighted by the negative R^2 for Γ_3 as well as for t_{start}.

4.6.2 Modeling Parameters Calibration

The three generated surrogate models are used to calibrate the implemented material models in Moldflow® by identifying the five parameters β, K_0, A, B, HTC_p using the algorithm described in Section 3.6. The optimization routine necessitated 15 iterations to reach a local minimum with a residuals norm of 11.72 as shown in Figure 4.10. In order to check if there exist other local minima for this multi-objective optimization and to find the global minimum, the built-in *MultiStart* MATLAB function is used to find the possible other local solutions to the optimization problem by starting from various initial points. This resulted in finding the same combination of parameters suggesting that the found local minimum is in fact the global one. The final optimized parameters are given in Table 4.10.

Starting by the optimized viscosity parameters, the identified solidification criterion parameter $A = 0.35$ seems reasonable since it is a parameter that takes into account the geometrical effects of the crystallites. According to Kennedy and Zheng [3] and Metzner [68], the criterion is approximately equal to 0.44 for rough compact crystals and since during injection molding non-spherical crystals develop due to shear, an $A < 0.44$ is expected. As for the exponent parameter B, the optimized value is nearly equal

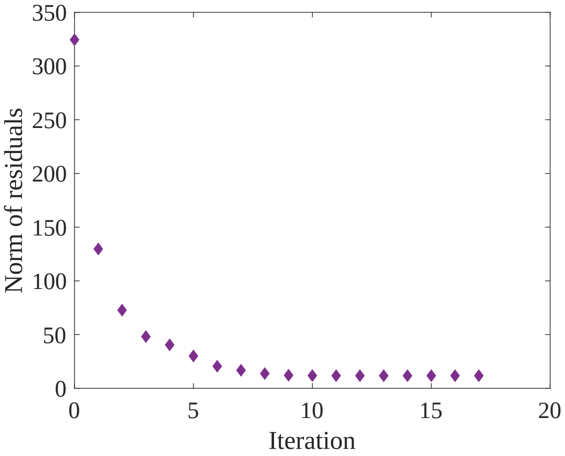

Figure 4.10 – The norm of the residuals as a function of the number of iterations performed by *lsqnonlin* during the optimization routine.

Table 4.10 – The identified modeling parameters from the multi-objective optimization algorithm.

Modeling Parameters (units)	**Identified Value**
β ($\mathrm{Pa^{-1}\,s^{-1}}$)	$-10^{11.37}$
$\ln(K_0)$ (-)	83.00
A (-)	0.35
B (-)	4.96
HTC_p ($\mathrm{W\,m^{-2}\,°C^{-1}}$)	500

to the upper interval bound of $B = 5$ which underlines the high coupling between the crystallization and viscosity. This correlates well with the observations made during the rheological tests presented in Figure 2.7 where the viscosity increases rapidly after the onset of crystallization. Moving on to the crystallization parameters, the FIC parameter β is not straightforward to assess but an exponent value of 11.37 translates into a lower contribution of FIC on the total relative crystallinity as compared to the interval midpoint β exponent value of 11. As for the identified quiescent crystallization parameter $\ln(K_0)$, it lies on the upper bound of the considered interval leading to high contribution of the quiescent crystallization on the α results. This can be reasonable as POM crystallizes rapidly leading to fast crystallization kinetics, however, the value is much greater than the one determined by Plummer and Kausch [127,128] equal to 53. Finally, the heat transfer coefficient during packing lies on the lower bound of its corresponding interval at $500\ \mathrm{W\,m^{-2}\,°C^{-1}}$. This indicates that the heat exchange between the mold cavity and the material is on the lower end. This value played an important role in the optimization since it directly affected the temperature profile which in turn affected the crystallization and the solidification of the material leading to a fully filled part or a short shot. As a reference, the default Moldflow® value is $2500\ \mathrm{W\,m^{-2}\,°C^{-1}}$.

In the next sections, the identified parameters are used in the Moldflow® implementation proposed in Section 4.2 and its results are compared to the default Moldflow® simulation that does not take crystallization explicitly into account.

4.6.2.1 Pressure Results

As shown in Table 4.7, each surrogate model is based on one experimental DoE. Additionally, the optimization used the experimental pressure signals at the sensor located after the gate (P2) to identify the modeling parameters given in Table 4.10. Therefore, to assess the proposed implementation's results, the pressure signals obtained using the simulation with the calibrated models (Simulation: Optimization) are plotted in comparison to the ones obtained by the default Moldflow® simulation (Simulation: Default) and as a reference the experimental results (Experimental). The plots presented in Figures 4.11, 4.12 and 4.13 correspond to the previously-mentioned results for the three processing conditions V6, V14 and V27, respectively and they show these predictions at the three sensor locations P1, P2 and P3 (refer to Figure 2.9).

By observing these comparison plots, it is clear that the simulation that takes into account polymer

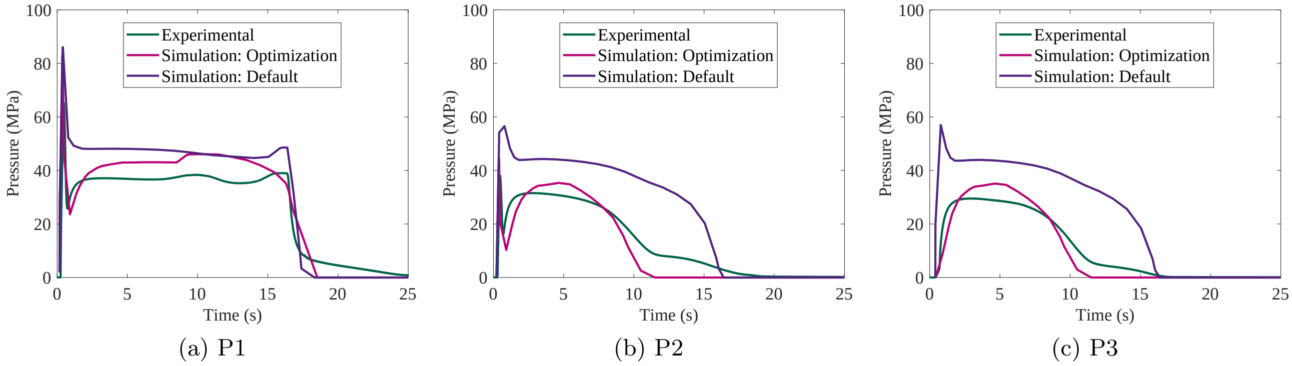

(a) P1 (b) P2 (c) P3

Figure 4.11 – The pressure signals for the V6 processing condition obtained using the simulation with the calibrated models (Simulation: Optimization) in comparison to the ones obtained by the default Moldflow simulation (Simulation: Default) along with the corresponding experimental results (Experimental) for this condition.

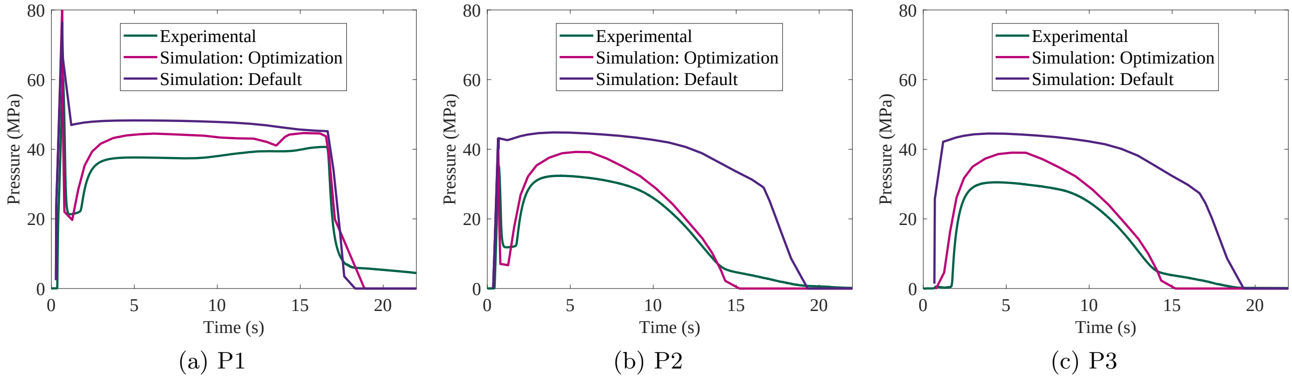

(a) P1 (b) P2 (c) P3

Figure 4.12 – The pressure signals for the V14 processing condition obtained using the simulation with the calibrated models (Simulation: Optimization) in comparison to the ones obtained by the default Moldflow simulation (Simulation: Default) along with the corresponding experimental results (Experimental) for this condition.

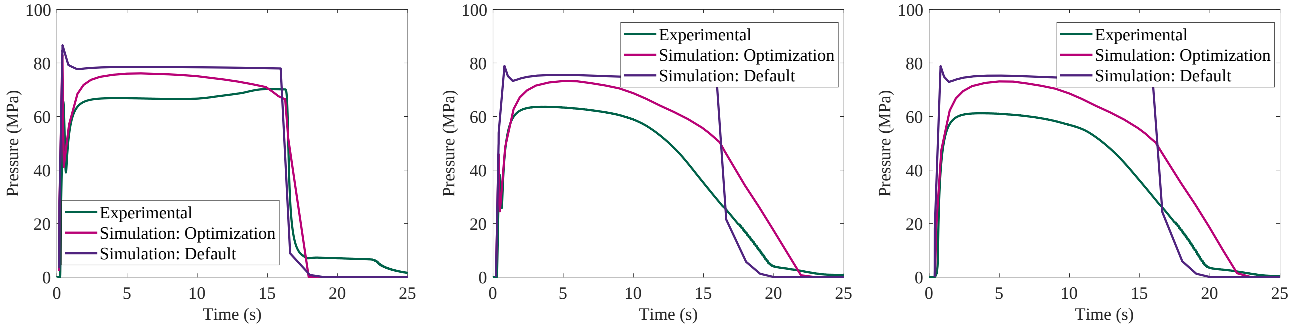

(a) P1 (b) P2 (c) P3

Figure 4.13 – The pressure signals for the V27 processing condition obtained using the simulation with the calibrated models (Simulation: Optimization) in comparison to the ones obtained by the default Moldflow simulation (Simulation: Default) along with the corresponding experimental results (Experimental) for this condition.

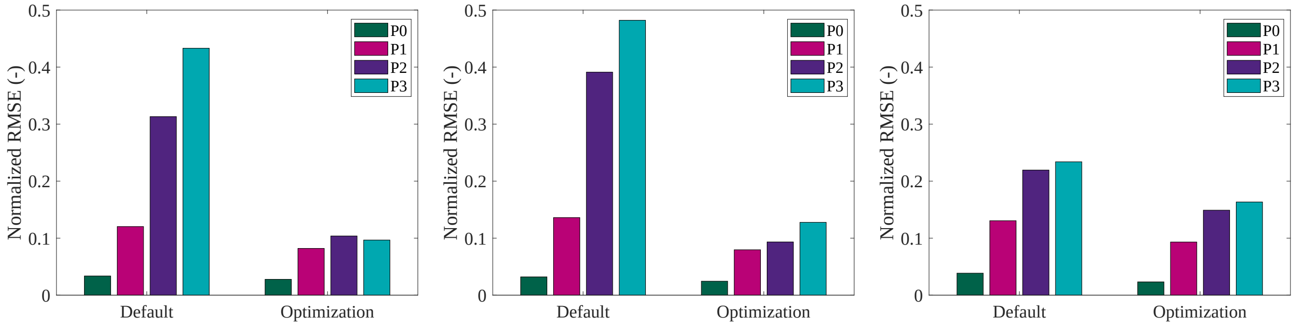

(a) V6 (b) V14 (c) V27

Figure 4.14 – The RMSE of the pressure predictions using the simulation with the calibrated models (Optimization) and the one using the default Moldflow models (Default) for each of the three processing conditions used to generate a surrogate model.

crystallization is performing much better than the one with the default models. For all three conditions, the pressure predictions improved drastically at the three sensor locations using the proposed method especially at P2 and P3. The estimations are following the same trend as the experimental results using the optimized parameters which is not the case while using the default settings. One interesting observation is the ability of the proposed models to recreate the constant pressure seen after the switch-over in Figures 4.12a and 4.12b at P1 and P2, respectively, which leads to a delay in the signal reaching P3 as predicted in Figure 4.12c for the V14 condition.

To quantify the improvement in pressure predictions, the normalized RMSE are calculated for the simulations using the default models and the ones using the proposed models. Figures 4.14a, 4.14b and 4.14c present the obtained results for the three processing conditions V6, V14 and V27, respectively.

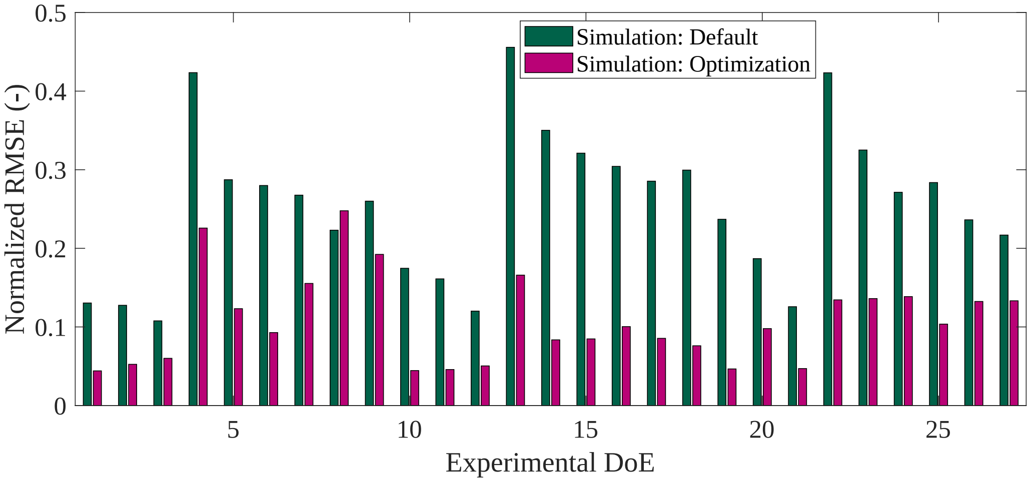

Figure 4.15 – The averaged normalized RMSE of the pressure predictions at P2 using the simulation with the calibrated models (Optimization) and the one using the default Moldflow models (Default) for all 27 experimental processing conditions for the half length 3 mm thick geometry.

As expected, the prediction error has significantly decreased by including the crystallization model along with the crystallization-dependent viscosity, PVT and solidification models with their identified parameters. Major improvement is apparent in the pressure estimation of P2 and P3 for conditions V6 and V14 where the error decreases three folds in the case of P2 and four times for P3. These sensors are located in the part cavity and therefore predicting the pressure at these locations more accurately can lead to more accurate shrinkage and warpage predictions. In the case of the V27 processing condition, the pressure predictions became closer to reality as seen in Figure 4.13, however, quantitatively, the error decreased by less than 5 %.

The above-discussed results seem quite promising, however, since the optimization is based on the three presented experimental results, it is still not yet certain that the identified parameters are able to predict other experimental conditions as well as the previously-shown ones. Therefore, Figure 4.15 presents the averaged normalized RMSE at P2 for all experimental processing conditions (Experimental DoE) summarized in Table 2.6 while using Moldflow$^{®}$ with default models or with the calibrated models of this work.

By observing Figure 4.15, for the majority of the different DoEs, the prediction error is decreased by more than half from the default results. The only exceptions are seen for the experimental DoEs V7, V8 and V9. To analyze the probable reasons behind this discrepancy, Figure 4.16 presents the pressure

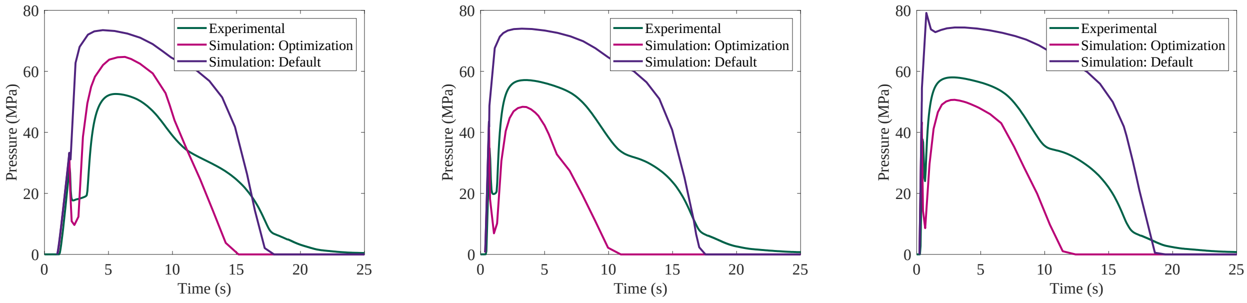

(a) V7, P2

(b) V8, P2

(c) V9, P2

Figure 4.16 – The P2 pressure signals for three processing condition obtained using the simulation with the calibrated models (Simulation: Optimization) in comparison to the ones obtained by the default Moldflow simulation (Simulation: Default) along with the corresponding experimental results (Experimental) for these conditions.

signals at P2 obtained experimentally in comparison to the ones predicted by the default simulation and by the simulation using the proposed models with the optimized parameters for the three conditions in consideration. By observing the presented results, it is apparent that both simulations are not able to recreate the experimental signals as the latter is more complex than the ones used to calibrate the material models. In the experimental data, during the packing phase around 10 s, the pressure signal changes slopes creating a second bump in the signal. This was hypothesized in Section 2.4.4 to be due to a probable partial remelting of the gate leading to additional polymer melt entering the cavity. Even though the model includes the effect of remelting, the current calibrated models are not able to recreate the shown bump in pressure. This shows the possibility that some model assumptions need to be revised or that the model is not fully calibrated yet. In Figure 4.16b, a slight change of slope is seen at around 7 s but not as prominent as in reality. As a final remark on this topic, the calibrated models are able to better predict the maximum pressure needed during filling as observed in Figure 4.16 and they predict the first bump in the pressure curve during packing more accurately than the default simulation.

4.6.2.2 Fill Predictions

As briefly mentioned in Section 2.4.4, some experimental DoEs for the HL3 part did not produce a fully filled part therefore a short shot was produced. Figure 4.17a summarizes the filling status of the 27 experimental DoEs. One of the main goals of implementing a crystallization model and crystallization-dependent material models is to be able to predict accurately when a part is fully filled

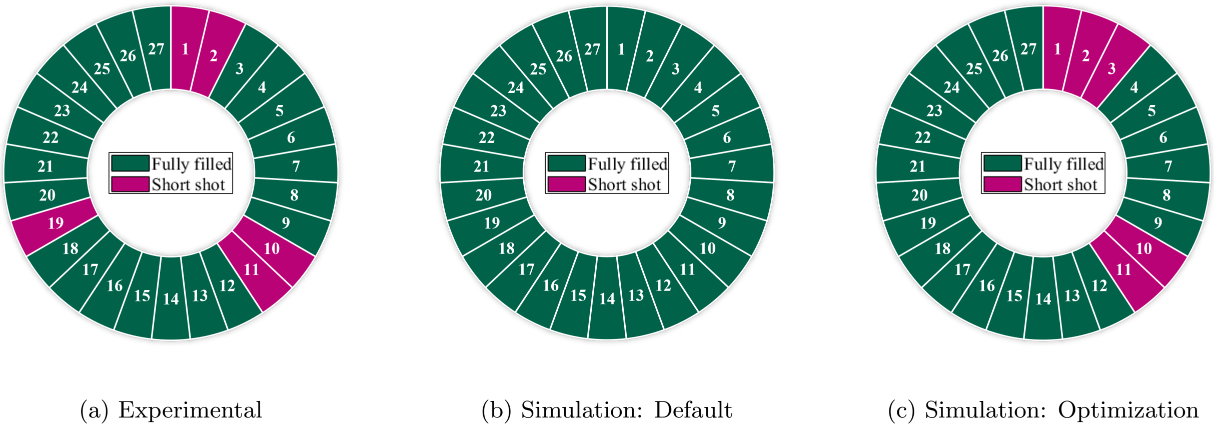

(a) Experimental (b) Simulation: Default (c) Simulation: Optimization

Figure 4.17 – The experimental fill results (a) in comparison to the ones predicted using the (b) default simulation, (b) simulation with the calibrated models.

and when not. Using the default Moldflow® simulation, it is not possible to predict the short shots as seen in Figure 4.17b. However, by using the proposed models in the Moldflow® simulation, it became possible to predict most of these short shots as shown in Figure 4.17c. In total, four out of the five short shots are identified along one wrongly predicted slight short shot for V3 ($\approx$ 4 mm not filled) and one wrongly estimated full fill for V19 which shorted around 7 mm experimentally. The flow length are accurate up to ±15 mm, such as for example for V10, it was not possible to fill the last 10 mm of the mold experimentally whereas in the simulation the leftover unfilled length was around 5 mm. In general, this is considered a huge advance in the topic of fill predictions and underlines the importance of implementing a crystallization model in injection molding simulations and the use of crystallization-dependent solidification criterion instead of one constant no-flow temperature.

4.6.2.3 Skin Layer Thickness

Since the proposed simulation approach includes a crystallization model, one of the simulation results is the relative crystallinity evolution. Therefore, this result is used to determine the skin layer thickness that is solidified during the filling phase and compacting under shear strain. As mentioned by Pantani et al. [15, 27], there exists a critical shear rate value above which the nucleation density and growth rate are affected due to flow. Since this critical value is hard to determine experimentally, a threshold value of 50 s^{-1} is postulated in this work below which the flow-induced crystallization is considered minimal. This value is obtained by analyzing the simulation results after switch-over

Table 4.11 – The skin layer thicknesses determined using the simulation utilizing the calibrated models across the thickness at the three sensor locations for four processing conditions (V1, V3, V19, V21).

	Simulated Skin Layer Thickness (mm)			
	V1	V3	V19	V21
Cross-section P1	0.40-0.68	0.21	0.23	0.10-0.21
Cross-section P2	0.35	0.08	0.17	0.02
Cross-section P3	0.20	0.08	0.09	-

where the shear rate decreases by two orders of magnitude to reach this threshold value. To determine the skin layer thickness solidified under the high shear conditions, the time at which the shear rate through the thickness at the sensor locations is below this threshold is first determined. Then the relative crystallinity result α is plotted at that time along the thickness of the part at the three sensor locations P1, P2 and P3 specified in Figure 2.9. Following this, the thickness where $\alpha > A$ is read from the plot. The simulation results are summarized in Table 4.11 and compared to the ones obtained using optical microscopy (refer to Section 2.4.5) in Figure 4.18.

By comparing the thicknesses determined experimentally and those from the simulation, it is important to keep in mind that both results are prone to errors and uncertainties. The experimental values could include some observational errors whereas the simulation ones are based on the assumption that the skin layer does not grow further when the shear rate is lower than 50 s^{-1}. Nevertheless, the simulation predictions are quite accurate with a mean absolute error of 7.5 % and give a good approximation of the skin layer thickness obtained using optical microscopy. Some discrepancies are present, however, the trend of the results is correct such as the thickness is bigger at the cross-section of P1 and it becomes smaller as we move further to P2 and P3. This is consistent with the experimental results.

4.6.3 Calibrated Models Used in Other Geometries

In this section, the calibrated parameters are tested on the three other geometries that are possible to produce with the same mold presented in Figure 2.9. The simulation results obtained using the default Moldflow® models are compared to the ones obtained from the implemented models along with the identified parameters.

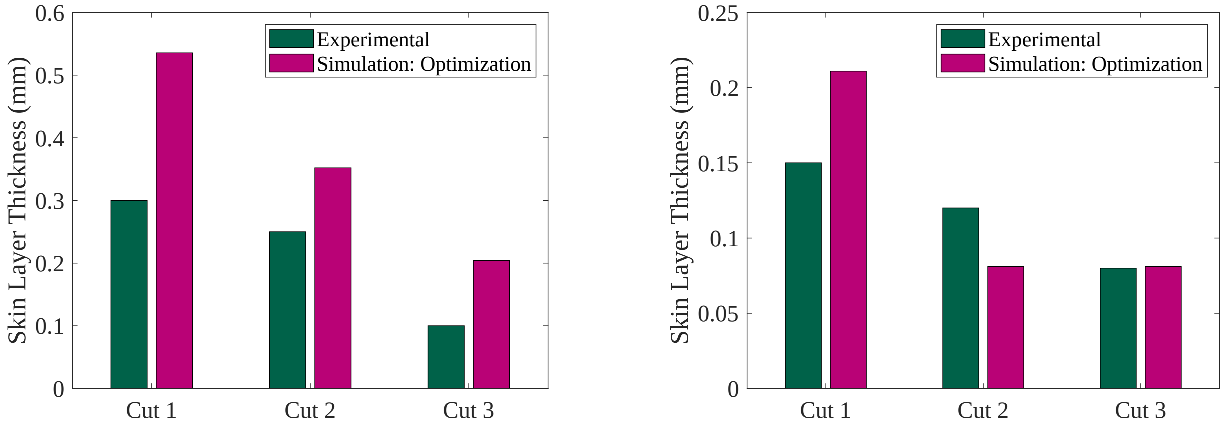

(a) V1 (b) V3

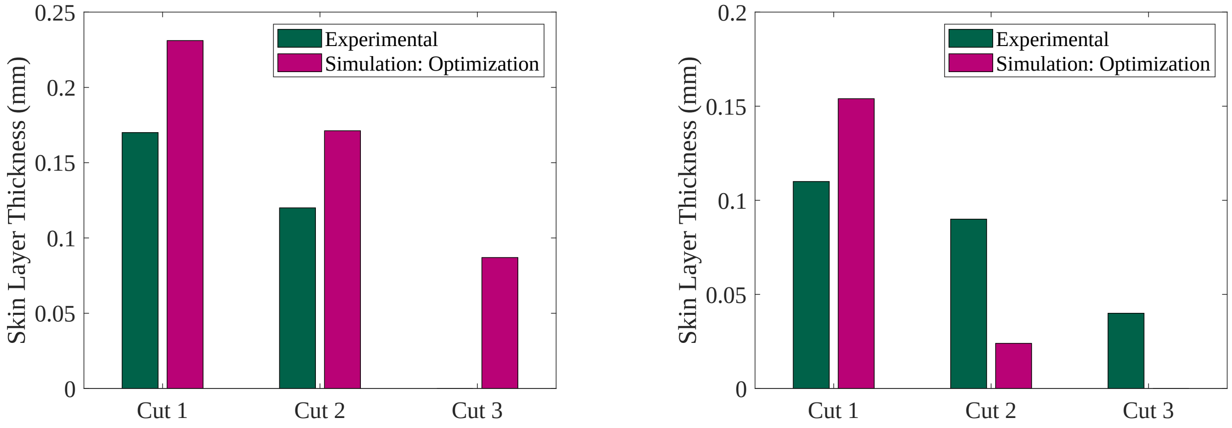

(c) V19 (d) V21

Figure 4.18 – The comparison between the skin layer thicknesses determined experimentally and those obtained using the optimized simulation along the part thickness of the three sensor locations.

4.6.3.1 Half Length 1.5 mm Thick Geometry

The first geometry considered is the one with the same cavity length as the main geometry (HL3) but with half of its thickness with 1.5 mm. This geometry is referred to as HL15. Figure 4.19 presents two experimental pressure results in comparison to the two different simulation results at P1 and P3 for the two processing conditions T2 and T25. At the P1 sensor location seen in Figures 4.19a and 4.19c, both simulation results are nearly the same and seem to recreate accurately the experimental pressure signal at P1. However, it is important to remember that the models behind these simulations are quite different and it is not expected that they produce the same result. This highlights that the implemented models with the crystallization-dependent solidification criterion performs similarly to the no-flow temperature criterion before the gate where the same runner system is used for both the HL3 and HL15 geometries. This shows that the proposed models are able to reproduce the no-flow temperature criterion for some special cases such as in this case where the incomplete solidification of the runner due to a lower cooling time led to the same pressure results for both simulations.

At the P3 sensor location seen in Figures 4.19b and 4.19d, the pressure prediction similarities of the two simulations is not anymore observed and the material solidifies earlier using the no-flow condition than using the crystallization-dependent criterion. Nevertheless, as shown in Figure 4.19b, the experimental P3 signal is zero for the T2 condition which signifies a shorted part. However, both simulations are not able to reproduce this result. Even when no short shot is produced experimentally such as it is the case for T25 shown in Figure 4.19d, both simulations are unable to predict the signal accurately. For this geometry, the pressure signals in the part along with the fill predictions are not as well-predicted as the ones in the main HL3 geometry. This is due to the under-prediction of the crystallization evolution which could result form multiple sources. One possible explanation is the low identified value of the HTC_p at 500 $\mathrm{W\,m^{-2}\,{}^{\circ}C^{-1}}$. As the mold thickness decreases, the heat exchange between the metal and the polymer melt is more prominent. This can directly relate to the bad prediction of short shots as the temperature profile is probably wrongly predicted leading to a more delayed solidification than observed experimentally. To summarize, the parameters calibrated using the HL3 geometry are unable to estimate the pressure signals correctly in the part cavity as well as the final filling status of the half length 1.5 mm thick geometry.

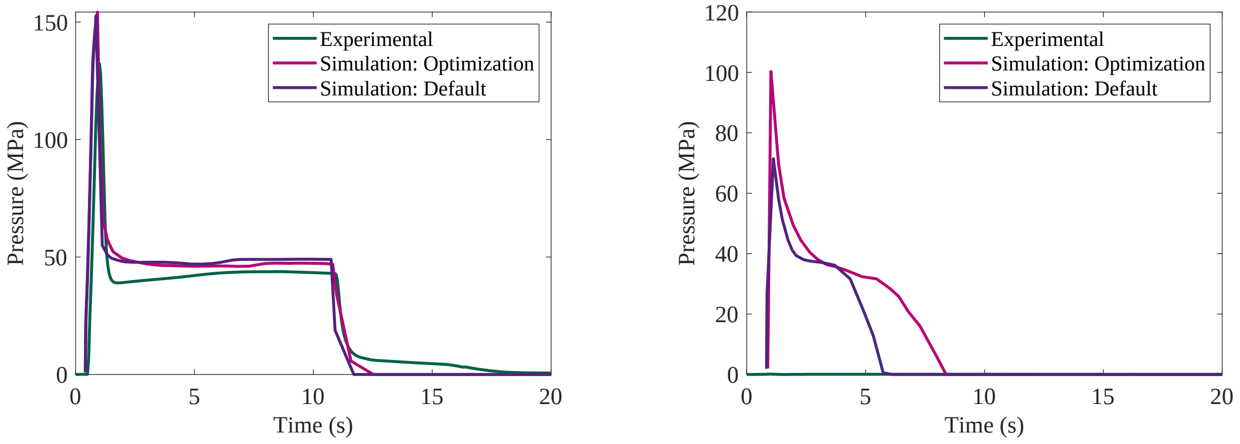

(a) T2, P1

(b) T2, P3

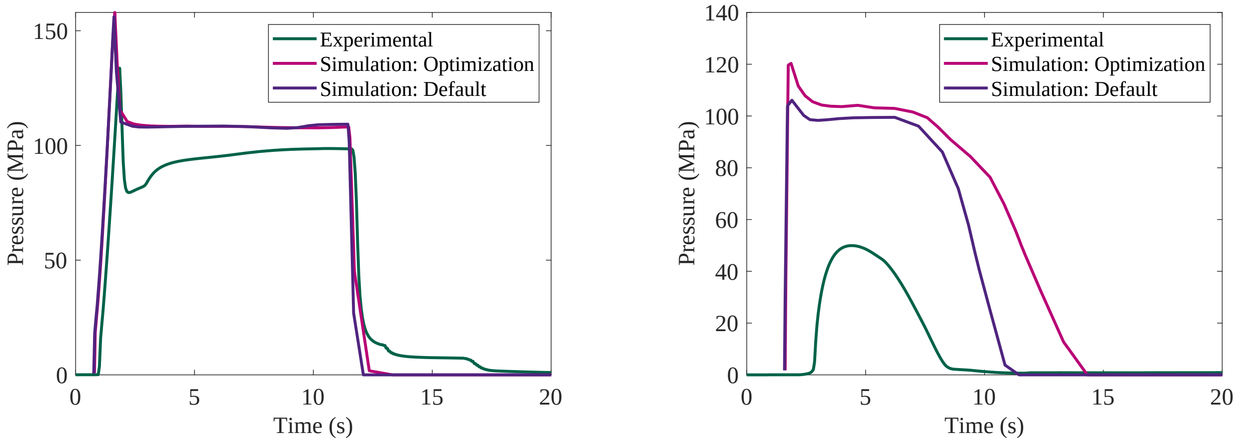

(c) T25, P1

(d) T25, P3

Figure 4.19 – Two example P1 and P3 pressure predictions for two processing conditions T2 and T25 injected with the half length 1.5 mm thick geometry using the simulation with the calibrated models (Simulation: Optimization) and the one with the default models (Simulation: Default) in comparison to the experimental results (Experimental).

4.6.3.2 Full Length 3 mm Thick Geometry

The second geometry considered is the one with the same cavity thickness as the main geometry (HL3) but with the whole length in order to make a U-shaped part. This geometry is referred to as FL3. Figure 4.20 presents two experimental pressure results in comparison to the two different simulation results at P1 and P3 for the two processing conditions S1 and S5. At the first glance, it is apparent that both simulations are unable to predict accurately the experimental pressure results especially during the packing phase of the process. By focusing on the simulation predictions using the implemented models with the optimized parameters presented in Table 4.10, it is clear that the filling phase is well-predicted but due to the early solidification of the gate the packing pressure is not delivered to the part cavity. This phenomenon is observed due to the prolonged shearing experienced along the 1 mm thick gate leading to higher flow-induced crystallization and therefore solidification followed by the restriction of the gate's cross-section. It is important to point that the injection velocity used for S1 and S5 is 5 cm^3/s which is slightly outside the bounds of the process settings of the HL3 geometry. With such a low velocity, the filling of the FL3 geometry takes four times longer than when using the lowest velocity of 10 cm^3/s for the HL3 geometry. The calibration using the HL3 geometry seems to be sensitive to the various complex physical phenomena happening at the gate leading to early solidification due to the fast FIC kinetics.

As for the filling predictions for this geometry, the simulation using the calibrated model predicted two short shots for the S2 and S4 conditions, however, experimentally no short shots were produced for all six conditions given in Table 2.5.

4.6.3.3 Full Length 1.5 mm Thick Geometry

The third and final geometry considered is the one with the full length U-shaped cavity having a 1.5 mm thickness. This geometry is referred to as FL15. For all experimental conditions presented in Table 2.7, the part produced was a short shot and the machine reached the maximum injection pressure of 240 MPa during the filling phase. Figure 4.21 presents two experimental pressure results in comparison to the two different simulation results at P1 and P3 for the two processing conditions W2 and W10. Both of the simulation pressure predictions at P1 for the W2 condition seen in Figure 4.21a predict correctly the short shot. However, after the machine maximum pressure is reached in both simulations around 0.5 s, the filling is switched to being pressure-controlled. In both these cases, there

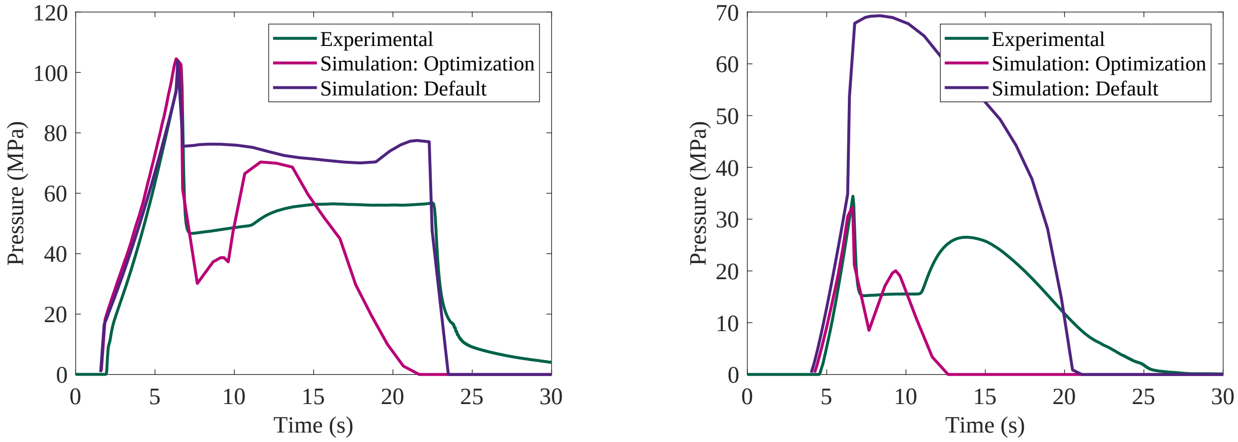

(a) S1, P1

(b) S1, P3

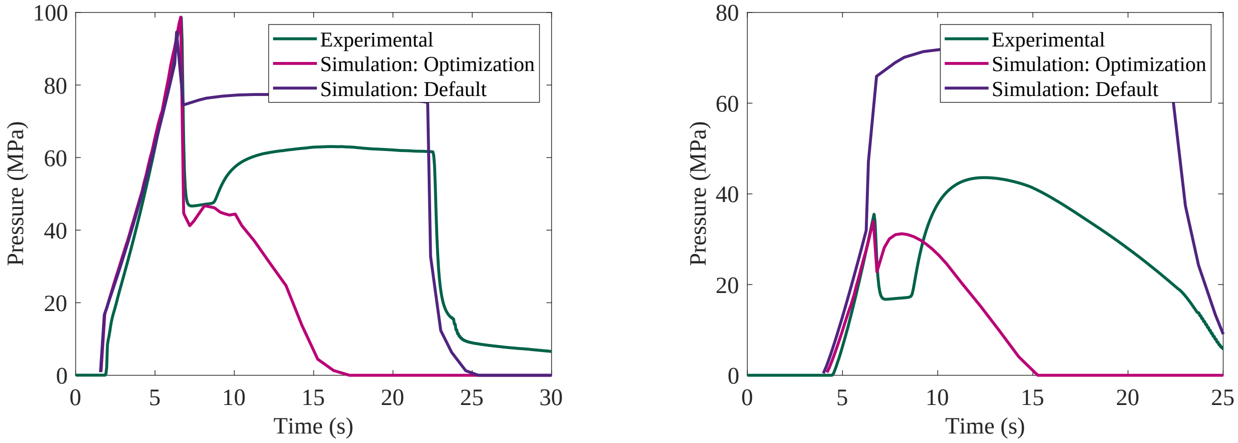

(c) S5, P1

(d) S5, P3

Figure 4.20 – Two example P1 and P3 pressure predictions for two processing conditions S1 and S5 injected with the full length 3 mm thick geometry using the simulation with the calibrated models (Simulation: Optimization) and the one with the default models (Simulation: Default) in comparison to the experimental results (Experimental).

is a relatively high average volume of around 14 V% of material already solidified and the switching to pressure-control filling may have led to a change of pressure distribution in the mold cavity that can explain the discontinuity seen in Figure 4.21a around 0.5 s. However, at the end of the filling stage, both simulations' pressure drops to zero following a linear line without applying the holding pressure of 50 MPa. This behavior and the previous observation can also be due to an artifact in Moldflow® and since it appears in both the default and optimized results, it indicates that it is not due to the user's code.

This behavior at P1 is encountered only in the optimized simulation for the W10 condition leading to a short shot unlike using the default simulation which predicts incorrectly a completely filled part as seen in Figure 4.21c. An interesting observation is the shape of the pressure signal in the default simulation which resembles the one measured experimentally but does a poor job in correctly recreating the end of the filling phase. As for the pressure predictions at the P3 sensor location for these two conditions presented in Figures 4.21b and 4.21d, the simulation using the proposed models along with the optimized parameters seems to estimate the experimental signals more accurately than the default simulation. Additionally, the simulation using the optimized parameters is able to correctly predict 24 out of the 27 short shots observed experimentally.

In general, the results for this geometry seem to be unreliable making it hard to assess the performance of the simulation using the calibrated model parameters. Therefore, they are not taken into account in the final assessment given in the following section.

4.7 Conclusion

In this chapter, the implementation of a crystallization model along with PVT, viscosity and solidification models is performed in Moldflow®. To calibrate the implemented models, three surrogate models are generated using model order reduction and least-squares regression. After studying the performance of the generated surrogates, it became apparent that the fitting method using the same second-order polynomial for all POD parameters and time shifts is not optimal. However, the generated surrogate models were still able to predict the pressure signals with high accuracy. Therefore, a multi-objective optimization scheme is performed to identify the five uncertain model parameters and the calibrated models are then tested in the simulation in comparison to the default Moldflow® simulation

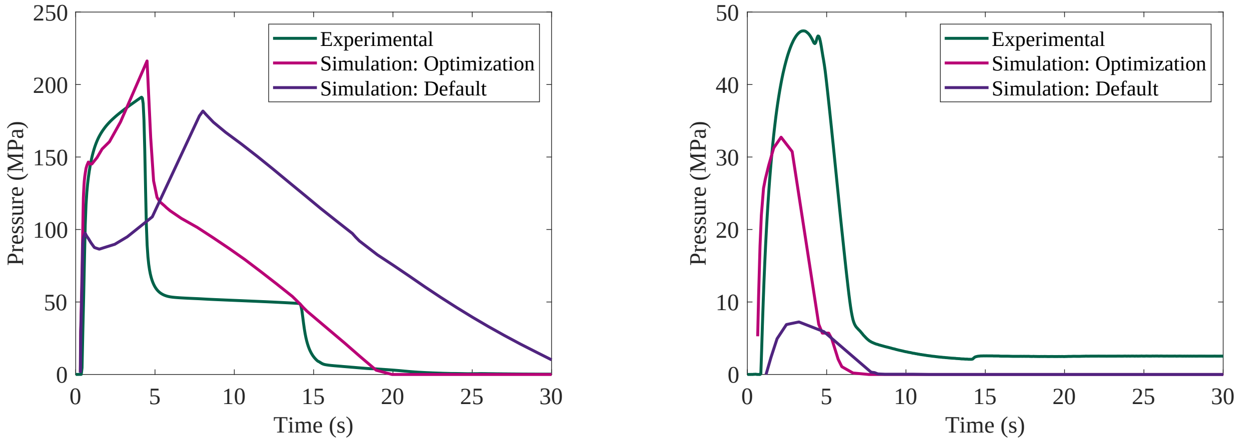

(a) W2, P1

(b) W2, P3

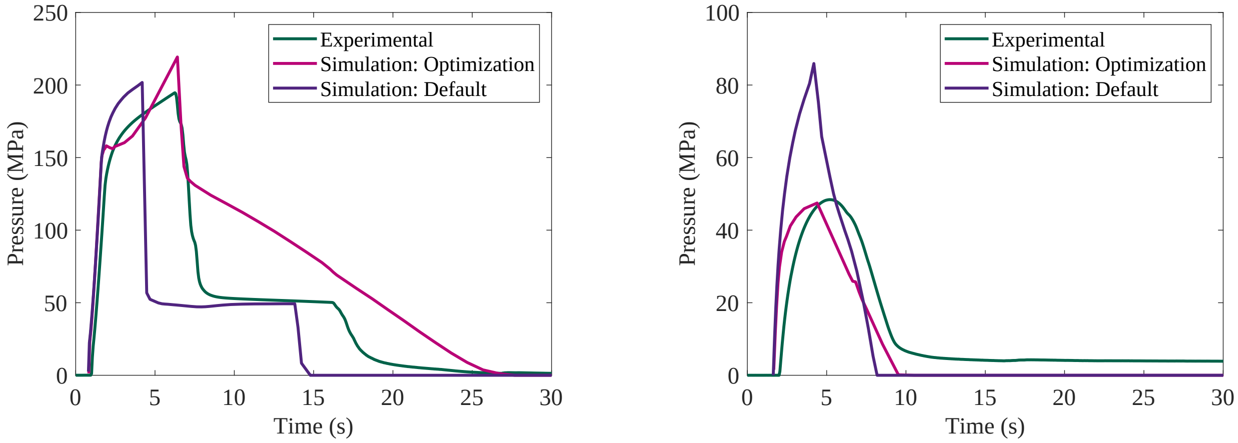

(c) W10, P1

(d) W10, P3

Figure 4.21 – Two example P1 and P3 pressure predictions for two processing conditions W2 and W10 injected with the full length 1.5 mm thick geometry using the simulation with the calibrated models (Simulation: Optimization) and the one with the default models (Simulation: Default) in comparison to the experimental results (Experimental).

results for the half length 3 mm thick part.

This comparison showed great improvements in the ability of the simulation using the calibrated models to predict the pressure signals more accurately where the prediction error decreased by more than half from the default simulation for the majority of the studied DoEs. Using the simulation with user-defined models, it became possible to predict short shots produced during processing whereas this was not possible with the default simulation. Additionally, to determine the skin layer thickness developed during the filling phase and compacting stage, a threshold shear rate is assumed under which the FIC is considered minimal. The determined thicknesses showed a good agreement with the ones measured experimentally and presented in Chapter 2.

Following this, the calibrated models are tested with the three other available mold geometries. The pressure signals are observed for a couple of processing settings and the simulation predictions using the user models and default ones are compared. As a general observation, for all three geometries, both simulation results performed poorly. By focusing only on the simulation with user-defined models, the HL15 geometry shed the light on a possible low heat transfer coefficient when the mold thickness is divided by half. Whereas the FL3 geometry suffered from fast FIC kinetics leading to early gate solidification which indicates a possible under-estimation of the β exponent parameter. But it can also underline the complexity of the physical phenomena happening in the gate making the original calibration scheme in the HL3 geometry highly sensitive to them and leading to non-generalized model parameters. As the FL15 geometry showed probable Moldflow® artifacts, it is not taken into account in this final discussion.

Conclusions and Outlook

In this thesis, after having proved the feasibility of using surrogate modeling to identify modeling parameters by a simple optimization scheme, three surrogate models are used to calibrate user-defined models implemented in an injection molding simulation. The commercial software Autodesk® Moldflow® Insight 2021 is used to simulate the injection molding of a semi-crystalline thermoplastic material. In Moldflow®, four user models are defined; a crystallization model describing both the flow-induced and quiescent crystallization along with crystallization-dependent viscosity, PVT and solidification models. These models are implemented in order to take into account the crystallization process happening during the processing of the material as it affects the flow solution as well as the predictions of warpage and shrinkage in the simulation. A multi-objective optimization is then performed to identify the model parameters using the generated surrogate models with the help of experimentally-measured pressure signals.

The simulation using the proposed models along with their identified parameters showed major improvements in the predictions of pressure signals in various conditions for the base mold geometry. One of the crucial advances made by using this implementation was the ability of the simulation to accurately predict the filling status of the produced parts (short shot or fully filled) . Additionally, due to the inclusion of a crystallization model, it became possible to observe the relative crystallinity evolution along the different phases of the injection molding process which helped in estimating the skin layer thicknesses formed under high-shear conditions.

The performance of the calibrated models is additionally assessed using three variations of the base mold geometry. The pressure predictions for these geometries using the calibrated models were not satisfactory. This highlighted different shortcomings of the implemented models along with their identified parameters. By changing the mold's thickness, it was not anymore possible to accurately predict the short shots. Whereas, by having a longer channel with the same base thickness, it became difficult to predict full filled parts. These behaviors could be due to various reasons. One of them is the use of global heat transfer coefficients for the filling and packing phases instead of local ones. This can lead to inaccurate temperature profile predictions affecting the whole heat balance calculations and in turn the crystallization and solidification predictions. Another reason could be that the chosen parameter intervals, for which the surrogate models are generated, are not big enough since some of the optimized parameters lied on the extremities of these intervals. An additional explanation could be that the calibration process was limited by the gate geometry and the complex physical phenomena happening in it such as early solidification due to high shears and fast cooling.

For future works, the redesign of the mold can be considered in which the gate is removed and the experimental runs are performed using a pressure-controlled filling. This could mitigate the probable errors contributed by the inclusion of the gate during the calibration of the models. Additionally, in the case of short shots, the flow length could be included as an extra output result and used in the models' calibration as it can give important information concerning the material solidification.

In the presented work, the measured pressure signal during the injection molding process is used to calibrate the models as it is accurately and easily measured during processing and can be directly related to the simulated pressure. The temperature measurements, on the other hand, are not as straightforward as the previous ones such as in the best case scenario the temperature sensors measure the mold surface temperature. However, this does not correlate well with the simulated temperature. Therefore, it would be interesting to use machine learning to bridge the gap between these two results in order to be able to use such measured data in a similar application as presented in this thesis.

As an outlook into the topic of surrogate modeling in the field of injection molding simulation, the present work can be extended to include a full time and space model. This could be used to visualize and assess solutions instantaneously while varying the input parameters. Such surrogate models provide the key to performing uncertainty quantification and efficient sensitivity analyses. Another interesting application is the creation of a digital twin of the injection molding process using these methodologies.

Chapter 5

Résumé en Français

Content

5.1 Introduction

Le moulage par injection est l'une des principales techniques de transformation des polymères avec laquelle plus d'un tiers des matériaux thermoplastiques sont produits [1]. Le processus de moulage par injection est cyclique et idéal pour la production en série de géométries complexes avec des tolérances serrées [2]. En cas de défauts de la pièce pendant la production, un changement des conditions du processus peut ne pas être suffisant et des modifications du moule doivent être appliquées pour résoudre le problème [3]. Cependant, cette démarche est coûteuse et prend du temps. Il est donc important de pouvoir prévoir ces problèmes dès la phase de conception de la pièce à l'aide de techniques de simulation. Par conséquent, pour minimiser ces coûts tout en garantissant une qualité supérieure du produit, la simulation du moulage par injection est largement utilisée pour concevoir efficacement les moules et fournir un outil pour déterminer les paramètres optimaux du processus qui permettent de surmonter les défauts couramment observés tels que le gauchissement, le rétrécissement.

Toutefois, au cours des dernières années, l'intérêt croissant pour les simulations de haute précision a entraîné une augmentation de la complexité des modèles intégrés et, par conséquent, une hausse des coûts de calcul. Ce problème est particulièrement souligné lors de l'utilisation de tels modèles de simulation pour l'optimisation, les analyses de sensibilité ou la quantification des incertitudes. La modélisation de substitution offre un moyen de surmonter les limites de ces simulations haute-fidélité et de réaliser de telles analyses de manière plus économique et plus rapide. Ces modèles sont généralement générés à l'aide d'un nombre relativement faible de simulations obtenues en faisant varier un nombre spécifique de paramètres d'entrée et sont ensuite capables d'approcher la sortie d'intérêt en quelques secondes au lieu de minutes ou d'heures en utilisant la simulation haute-fidélité. Un exemple d'application est présenté dans la figure 5.1 où un modèle de substitution est utilisé pour calibrer les paramètres du modèle de simulation en exécutant une routine d'optimisation efficace. Dans le cas présenté, le modèle de substitution représente un résultat de sortie appris à partir de l'exécution de plusieurs simulations haute-fidélité et est ensuite utilisé indépendamment pour obtenir les paramètres d'entrée optimaux qui correspondent le mieux aux résultats expérimentaux. Actuellement, dans le domaine de la simulation du moulage par injection, l'utilisation de la modélisation de substitution dans la littérature se limite principalement à l'optimisation des paramètres du processus tels que les températures du moule et de la matière fondue [5,6], les temps de remplissage et de refroidissement [7,8],

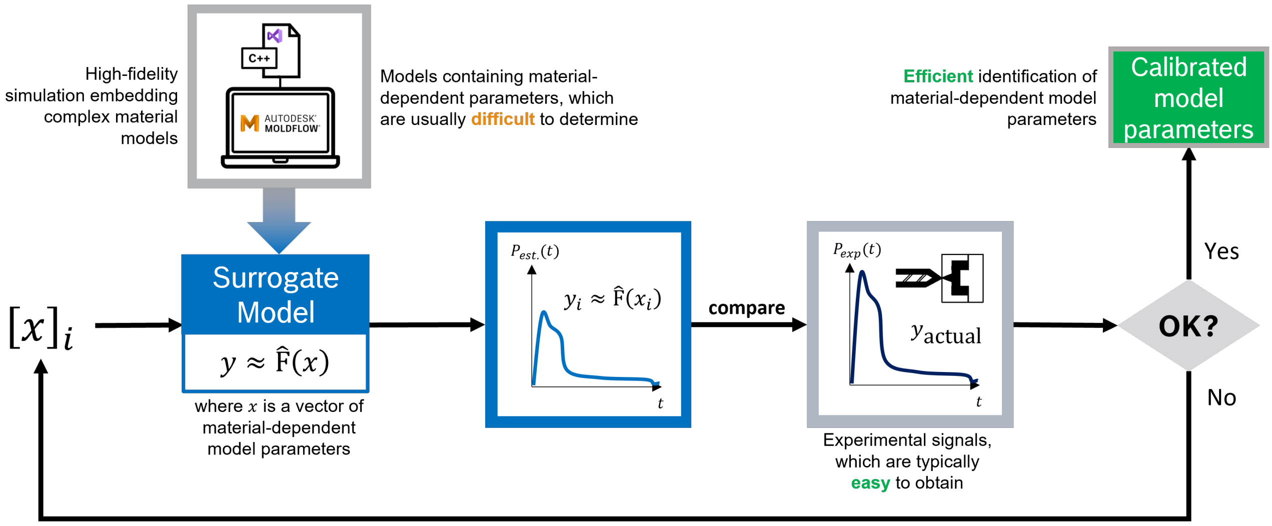

Figure 5.1 – Schéma d'optimisation des paramètres du modèle utilisant un modèle de substitution [4].

la pression de post-remplissage [9, 10]... Une publication récente d'Ivan et al. [11] utilise un modèle de substitution pour identifier deux paramètres de modèle qui décrivent l'orientation des fibres. Une approche similaire pourrait être utilisée pour calibrer d'autres types de modèles de matériaux complexes tels qu'un modèle de cristallisation. En raison de la complexité de l'identification expérimentale des paramètres de cristallisation dans des conditions de moulage par injection, de nombreux logiciels commerciaux n'en tiennent pas compte, même lorsqu'ils traitent de l'injection de matériaux semi-cristallins. Cela conduit à des inexactitudes dans les prédictions de remplissage ainsi que dans l'estimation du gauchissement et du rétrécissement dans la simulation [3].

Au cours des dernières décennies, de grands efforts ont été faits pour modéliser la cristallisation des polymères en tenant compte de l'histoire de l'écoulement de la matière fondue. Une approche commune utilisée pour décrire la cristallisation induite par l'écoulement, observée pendant le moulage par injection, est basée sur la théorie de nucléation et de croissance d'Avrami-Kolmogorov [12,13] combinée aux équations de vitesse de Schneider [14]. Cette méthode nécessite la détermination expérimentale d'un grand nombre de paramètres du modèle et la résolution d'un système complexe et interdépendant d'équations différentielles [15]. En revanche, Poitou et al. [16,17] ont proposé une approche thermomécanique décrivant à la fois la cristallisation induite par l'écoulement et la cristallisation naturelle avec un nombre beaucoup plus faible de paramètres de modèle, ce qui rend son utilisation plus attrayante dans les logiciels de simulation.

L'objectif principal de cette thèse est l'utilisation de la modélisation de substitution dans la calibration des paramètres d'un modèle de cristallisation implémenté dans une simulation de moulage par injection. Afin d'atteindre cet objectif, une étude de faisabilité est d'abord réalisée pour évaluer l'utilisation de différentes techniques de modélisation de substitution et de plans d'expériences dans la calibration des paramètres de modélisation dans la simulation de moulage par injection d'une pièce thermoplastique en polyoxyméthylène. Cette étape est suivie de l'implémentation d'un modèle de cristallisation modifié de Poitou et al. ainsi que de modèles de viscosité, de PVT et de solidification dépendant de la cristallisation dans le logiciel commercial Autodesk® Moldflow® Insight 2021 en utilisant la fonction Solver API. Les modèles sont mis en œuvre en 3D et calibrés à l'aide de trois modèles de substitution représentant la pression simulée dans différentes conditions de traitement. La capacité des modèles calibrés à prédire avec précision la pression, l'état de remplissage et l'épaisseur de la couche cristalline est testée dans différentes conditions en utilisant une géométrie de moule de base et trois variations de celle-ci.

5.2 Contenu et Structure de la Thèse

La simulation du moulage par injection constitue un moyen rentable de concevoir et d'améliorer la qualité des pièces avant de produire un moule, ainsi que d'identifier les paramètres optimaux du processus pour la production. Toutefois, pour y parvenir, les simulations doivent être très précises et comporter de moins en moins d'approximations. Dans le cas des thermoplastiques semi-cristallins, cela signifie qu'il faut prendre en compte le processus complexe de cristallisation qui a lieu pendant le traitement du matériau, ainsi que son effet sur d'autres propriétés telles que la viscosité et le volume spécifique. De plus, afin d'améliorer les prédictions de remplissage global ainsi que les estimations de gauchissement et de retrait, le critère de solidification doit être couplé à la cristallisation au lieu d'utiliser une valeur de température constante sans écoulement pour déterminer la solidification. Néanmoins, comme nous l'avons vu dans la section 1.3, le processus de cristallisation dans des conditions d'écoulement est complexe et la physique qui le sous-tend n'est pas encore totalement comprise, ce qui rend ce problème difficile à résoudre. De plus, la plupart des modèles disponibles sont des modèles phénoménologiques avec un grand nombre de paramètres qui sont difficiles à déterminer expérimentalement en raison de l'impossibilité de recréer les conditions extrêmes rencontrées pendant le processus de moulage par injection en utilisant les dispositifs expérimentaux actuels. Une façon de surmonter cet inconvénient est d'utiliser un modèle de substitution pour représenter un résultat de simulation qui peut être mesuré expérimentalement sur la machine de moulage par injection et de l'utiliser pour identifier les paramètres du modèle comme Ivan et al. [11] l'ont fait pour les paramètres du modèle d'orientation des fibres.

Par conséquent, dans cette thèse, l'objectif principal est d'implémenter un modèle de cristallisation dans une routine de simulation d'injection 3D tout en prenant en considération l'effet de la cristallisation sur les modèles de viscosité, PVT et solidification. Afin d'identifier les paramètres expérimentaux difficiles à déterminer, des modèles de substitution sont générés pour représenter les résultats de pression obtenus par la simulation et pour effectuer une calibration à l'aide de mesures expérimentales de signaux de pression obtenues lors d'essais de moulage par injection.

Pour atteindre cet objectif, la théorie et l'état actuel de l'art dans le domaine du moulage par injection, de la cristallisation des polymères et de la modélisation de substitution ont d'abord été présentés dans ce chapitre. Le chapitre 1 se termine par la présentation de quelques travaux de la littérature qui ont utilisé la modélisation de substitution pour représenter des résultats de simulation de moulage par injection similaires à ceux qui seront présentés dans ce travail.

Ensuite, la caractérisation du matériau ainsi que les essais de moulage par injection réalisés sont décrits dans le chapitre 2. De plus, dans ce chapitre, certains des signaux de pression expérimentaux sont analysés pour les différentes géométries considérées dans cette thèse ainsi que certaines micrographies produites pour observer la morphologie cristalline dans l'épaisseur des pièces produites.

Dans le chapitre 3, une étude de faisabilité est réalisée pour tester l'utilisation de la modélisation de substitution dans le but de calibrer certains paramètres de modélisation dans la simulation de moulage par injection. Cette étude compare trois approches différentes de modélisation de substitution et teste l'effet du nombre de simulations d'entraînement sur la précision des résultats de pression prédits.

Enfin, dans le chapitre 4, l'implémentation d'un modèle de cristallisation basé sur la thermomécanique est décrite ainsi que les modèles de viscosité, de PVT et de solidification dépendant de la cristallisation dans Moldflow® pour simuler le moulage par injection d'un matériau thermoplastique non renforcé. Cinq paramètres de modélisation sont identifiés à l'aide de trois modèles de substitution générés par une routine d'optimisation multi-objectifs. Les résultats de la simulation utilisant les modèles calibrés sont ensuite analysés pour différentes conditions de traitement et géométries de moule.

5.3 Caractérisation des Matériaux et Essais de Moulage par Injection

Le matériau polymère utilisé dans ce travail est un homopolymère de polyoxyméthylène (POM) non renforcé de qualité industrielle sous sa forme granulaire. Ce polymère, également connu sous le nom de polyacétal, est un matériau thermoplastique semi-cristallin d'ingénierie largement utilisé dans l'industrie automobile en raison de sa grande rigidité, de sa faible friction et de ses excellentes propriétés anti-usure [21, 113].

Deux types d'expériences sont réalisées afin de caractériser le matériau utilisé. Le premier type était les mesures DSC qui ont fourni des informations sur le comportement de cristallisation du matériau sous différentes vitesses de refroidissement. Ceci a permis de déterminer la température de fusion du matériau à 178,88 °C et l'enthalpie de cristallisation de 155,35 J/g. L'évolution de la cristallinité relative avec la température et le temps sous les différents taux de refroidissement a également été déterminée et sera utilisée pour quantifier la cinétique de cristallisation du POM dans le chapitre 4. Le deuxième type d'expérience est un test dynamique de rampe de température utilisé pour identifier la dépendance de la viscosité à la température et observer son comportement après le début de la cristallisation. Ces données seront également utilisées pour déterminer les paramètres du modèle de viscosité plus tard dans le travail.

Un moule a été conçu pour permettre la production de quatre géométries différentes variant en longueur et/ou en épaisseur, ainsi que la mesure des signaux de pression pendant le processus de moulage par injection à quatre endroits de la cavité. Pour mettre en place les essais de moulage par injection, des études de remplissage et d'emballage ont été réalisées, suivies des essais officiels où, pour chaque géométrie, trois paramètres du processus sont modifiés. Les paramètres variables sont la température du moule, la vitesse d'injection et la pression de maintien. Certains signaux de pression caractéristiques ont été analysés dans ce chapitre pour donner un aperçu des résultats obtenus qui sont utilisés dans ce travail pour la calibration des paramètres du modèle.

Certains des échantillons moulés par injection ont été étudiés à l'aide d'un microscope optique polarisé afin de mieux comprendre les morphologies des cristaux et les différentes couches qui se forment au cours du processus. Des coupes au microtome ont été réalisées à l'emplacement des capteurs pour différents paramètres du processus afin d'étudier l'effet de la température du moule et de la vitesse d'injection sur la morphologie et l'épaisseur de la couche de peau. En observant les différentes micrographies, il est apparu que plus la température du moule et la vitesse d'injection sont élevées, plus la couche cristalline est fine.

5.4 Étude de Faisabilité : Utilisation de la Modélisation de Substitution pour la Calibration des Paramètres de Modélisation

La faisabilité de l'utilisation de la modélisation de substitution pour calibrer les paramètres dans une simulation de moulage par injection est étudiée. Trois paramètres de modélisation sont choisis pour la calibration dans cette étude. Il s'agit des coefficients de transfert de chaleur pendant le remplissage et le compactage ainsi que du coefficient de dépendance à la pression dans le modèle de viscosité Cross-WLF [117,118]. Les paramètres susmentionnés sont connus pour affecter les résultats de pression dans la simulation et leur détermination expérimentale est difficile et prend du temps [119–121]. Pour cette calibration, la géométrie de la demi-longueur de 3 mm d'épaisseur présentée sur la figure 2.11 est utilisée et les trois paramètres de modélisation sont étalonnés à l'aide des données expérimentales du capteur de pression P2 (voir la figure 2.9).

Dans cette étude de faisabilité, on étudie la précision de trois techniques de modélisation de substitution basées sur la régression et de deux méthodes de plan d'expérience dans leur capacité à approximer le signal de pression à un seul nœud de la simulation. Les approches de modélisation proposées sont les suivantes :

1. un modèle de régression non linéaire des coefficients de la décomposition orthogonale propre entraîné à l'aide d'un échantillonnage fixe de l'Hypercube latin (POD-NLR),
2. un modèle de polynomial chaos expension ajusté par une technique d'optimisation des moindres carrés utilisant les mêmes points d'échantillonnage fixes de l'Hypercube latin (Regular-PCE-LS), et
3. un modèle de polynomial chaos expension ajusté par une technique d'optimisation des moindres carrés, mais utilisant une DoE adaptative qui est enrichie pendant la génération du modèle (Adaptive-PCE-LS).

Les modèles sont entraînés à l'aide de 30, 60 et 120 cycles de simulation et leurs prédictions sont évaluées en conséquence. Les trois modèles sont construits en faisant varier un total de six paramètres d'entrée, y compris les paramètres du processus et les variables de modélisation. Les paramètres du processus sont la vitesse d'injection, la température d'entrée du liquide de refroidissement, la pression de maintien et les paramètres de modélisation, comme déjà mentionné, sont les coefficients de transfert de chaleur pendant le remplissage et le conditionnement ainsi que le coefficient dépendant de la pression dans le modèle de viscosité Cross-WLF. Après avoir obtenu les modèles de substitution, une analyse de sensibilité est effectuée pour étudier la contribution de chaque paramètre varié au signal de pression ainsi que leur interaction les uns avec les autres. Enfin, en utilisant les données de pression expérimentales mesurées et l'un des modèles de substitution générés, les paramètres de modélisation sont calibrés et l'erreur entre la simulation optimisée et la simulation par défaut est comparée.

Cette étude a montré que le modèle de substitution POD-NLR et le modèle de substitution PCE-LS régulier présentent fondamentalement les mêmes performances, en particulier lorsque le nombre de données d'entraînement est faible. En augmentant le nombre de données d'entraînement, la technique PCE-LS adaptative améliore régulièrement la précision du modèle de substitution et atteint une performance comparable à celle des techniques à DoE fixe pour 120 simulations d'entraînement. Les avantages de la technique adaptive-PCE-LS devraient apparaître plus clairement lorsque le nombre de variables est élevé.

Sur la base d'une analyse de sensibilité 'Sobol' utilisant le modèle de substitution généré, nous avons constaté que le coefficient de transfert de chaleur pendant le remplissage a un faible impact sur l'évolution de la pression au niveau d'un nœud de capteur devant le coefficient de transfert de chaleur pendant le conditionnement ou le coefficient de viscosité dépendant de la pression. En optimisant les paramètres $HTC_{filling}$, $HTC_{packing}$ et le paramètre D_3 du modèle de viscosité dépendant de la pression à l'aide des signaux de pression mesurés, il a été possible de calibrer la simulation haute-fidélité afin de diminuer les déviations dans l'estimation de la pression par rapport à celles obtenues en utilisant les valeurs de simulation par défaut. Cependant, il existe encore une lacune dans l'obtention d'une estimation précise des champs de pression dans le moulage par injection, qui pourrait être comblée avec cette méthodologie en incluant des paramètres de modèle de simulation supplémentaires en plus d'un raffinement des modèles mis en œuvre dans la simulation, comme le montre le chapitre suivant en mettant en œuvre un modèle de cristallisation induite par l'écoulement ainsi qu'un diagramme

PVT, de la viscosité et le critère de solidification dépendant de la cristallisation pour les polymères thermoplastiques semi-cristallins.

5.5 Utilisation de la Modélisation de Substitution pour Calibrer un Modèle de Cristallisation Induite par l'Écoulement dans Moldflow

L'étude de faisabilité a montré qu'il est possible d'optimiser ces paramètres en utilisant les résultats de pression expérimentale à l'aide d'un modèle de substitution représentant les résultats de pression simulée à un nœud de surface. Par conséquent, dans ce chapitre, une méthodologie similaire est suivie afin de calibrer un modèle de cristallisation induit par l'écoulement ainsi que des modèles PVT, de la viscosité et de solidification dépendant de la cristallisation. Ces modèles sont implémentés dans Moldflow® à l'aide d'un code utilisateur. Au total, trois modèles de substitution sont utilisés pour identifier les cinq paramètres de modélisation incertains et ces substituts sont générés à l'aide d'une méthode POD-NLR analogue à celle présentée au chapitre 3. Par exemple, les signaux de pression sont d'abord réduits à l'aide de la technique de décomposition orthogonale appropriée, suivie d'une régression des moindres carrés d'un polynôme du second ordre. Cette méthodologie a été choisie car elle a montré une bonne performance en utilisant un faible nombre de données d'apprentissage et un faible nombre de paramètres d'entrée. Après avoir obtenu les paramètres de modélisation optimisés, les performances de la simulation sont évaluées en étudiant la capacité à prédire les signaux de pression, l'état de remplissage et l'épaisseur de la couche de peau à l'aide des modèles définis par l'utilisateur par rapport aux résultats expérimentaux. En outre, les modèles calibrés sont testés en utilisant trois géométries de moule différentes afin de vérifier la généralité des paramètres identifiés.

Après avoir étudié les performances des modèles de substitution générés, il est apparu que la méthode d'ajustement utilisant le même polynôme du second ordre pour tous les paramètres POD et les décalages temporels n'est pas optimale. Cependant, les modèles de substitution générés étaient toujours capables de prédire les signaux de pression avec une grande précision. Par conséquent, un schéma d'optimisation multi-objectif est exécuté pour identifier les cinq paramètres incertains du modèle et les modèles calibrés sont ensuite testés dans la simulation en comparaison avec les résultats de simulation par défaut de Moldflow® pour la demi-longueur de la pièce de 3 mm d'épaisseur.

Cette comparaison a montré de grandes améliorations dans la capacité de la simulation utilisant les modèles calibrés à prédire les signaux de pression avec plus de précision où l'erreur de prédiction a diminué de plus de la moitié par rapport à la simulation par défaut pour la majorité des DoEs étudiées. En utilisant la simulation avec des modèles définis par l'utilisateur, il est devenu possible de prédire les coups courts produits pendant le traitement alors que cela n'était pas possible avec la simulation par défaut. En outre, pour déterminer l'épaisseur de la couche cristalline développée pendant la phase de remplissage et l'étape de compactage, on suppose un taux de cisaillement seuil en dessous duquel le FIC est considéré comme minimal. Les épaisseurs déterminées ont montré un bon accord avec celles mesurées expérimentalement et présentées dans le chapitre 2.

Ensuite, les modèles calibrés sont testés avec les trois autres géométries de moule disponibles. Les signaux de pression sont observés pour quelques paramètres de traitement et les prédictions de simulation utilisant les modèles de l'utilisateur et ceux par défaut sont comparés. D'une manière générale, pour les trois géométries, les deux résultats de simulation ont donné de mauvais résultats. En se concentrant uniquement sur la simulation avec les modèles définis par l'utilisateur, la géométrie HL15 a mis en lumière un possible faible coefficient de transfert de chaleur lorsque l'épaisseur du moule est divisée par deux. La géométrie FL3, quant à elle, a souffert d'une cinétique FIC rapide conduisant à une solidification précoce de l'entrée, ce qui indique une possible sous-estimation du paramètre exposant β. Mais cela peut également souligner la complexité des phénomènes physiques qui se produisent dans la grille, rendant le schéma de calibration original dans la géométrie HL3 très sensible à ces phénomènes et conduisant à des paramètres de modèle non généralisés. Comme la géométrie FL15 a montré de probables artefacts Moldflow®, elle n'est pas prise en compte dans cette discussion finale.

5.6 Conclusions et Perspectives

Dans cette thèse, après avoir prouvé la faisabilité de l'utilisation de modèles de substitution pour identifier les paramètres de modélisation par un schéma d'optimisation simple, trois modèles de substitution sont utilisés pour calibrer des modèles définis par l'utilisateur et implémentés dans une simulation de moulage par injection. Le logiciel commercial Autodesk® Moldflow® Insight 2021 est utilisé pour simuler le moulage par injection d'un matériau thermoplastique semi-cristallin. Dans Moldflow, quatre modèles utilisateur sont définis : un modèle de cristallisation décrivant à la fois la cristallisation induite par l'écoulement et la cristallisation naturelle, ainsi que des modèles de viscosité, de PVT et de solidification dépendant de la cristallisation. Ces modèles sont mis en œuvre afin de prendre en compte le processus de cristallisation qui se produit pendant le traitement du matériau et qui affecte la solution d'écoulement ainsi que les prédictions de déformation et de rétraction dans la simulation. Une optimisation multi-objectifs est ensuite réalisée pour identifier les paramètres du modèle en utilisant les modèles de substitution générés avec l'aide de signaux de pression mesurés expérimentalement.

La simulation utilisant les modèles proposés avec leurs paramètres identifiés a montré des améliorations majeures dans les prédictions des signaux de pression dans diverses conditions pour la géométrie du moule de base. L'un des progrès cruciaux réalisés grâce à cette mise en œuvre est la capacité de la simulation à prédire avec précision l'état de remplissage des pièces produites (remplissage partiel ou remplissage complet). En outre, grâce à l'inclusion d'un modèle de cristallisation, il est devenu possible d'observer l'évolution de la cristallinité relative au cours des différentes phases du processus de moulage par injection, ce qui a permis d'estimer l'épaisseur des couches cristallines formées dans des conditions de cisaillement élevé.

La performance des modèles calibrés est également évaluée en utilisant trois variations de la géométrie du moule de base. Les prédictions de pression pour ces géométries utilisant les modèles calibrés n'étaient pas satisfaisantes. Cela a mis en évidence différentes lacunes des modèles mis en œuvre ainsi que leurs paramètres identifiés. En modifiant l'épaisseur du moule, il n'était plus possible de prédire avec précision le remplissage partiel. En revanche, en ayant un canal plus long avec la même épaisseur de base, il est devenu difficile de prédire les pièces entièrement remplies. Ces comportements peuvent être dus à diverses raisons. L'une d'entre elles est l'utilisation de coefficients de transfert de chaleur globaux pour les phases de remplissage et de post-remplissage au lieu de coefficients locaux. Cela peut conduire à des prédictions de profil de température inexactes qui affectent l'ensemble des calculs de bilan thermique et, par conséquent, les prédictions de cristallisation et de solidification. Une autre raison pourrait être que les intervalles de paramètres choisis, pour lesquels les modèles de substitution sont générés, ne sont pas assez grands puisque certains des paramètres optimisés se situent aux extrémités de ces intervalles. Une autre explication pourrait être que le processus de calibration a été limité par la géométrie de la porte et les phénomènes physiques complexes qui s'y produisent, comme la solidification précoce due à des cisaillements élevés et à un refroidissement rapide.

Pour les travaux futurs, on peut envisager de revoir la conception du moule en supprimant le seuil d'injection et en effectuant les essais expérimentaux avec un remplissage contrôlé par la pression. Cela pourrait atténuer les erreurs probables dues à l'inclusion du seuil lors de la calibration des modèles. En outre, dans le cas de remplissages partiels, la longueur d'écoulement pourrait être incluse comme un résultat de sortie supplémentaire et utilisée dans la calibration des modèles, car elle peut donner des informations importantes sur la solidification du matériau.

Dans le travail présenté, le signal de pression mesuré pendant le processus de moulage par injection est utilisé pour calibrer les modèles car il est mesuré avec précision et facilement pendant le traitement et peut être directement relié à la pression simulée. Les mesures de température, en revanche, ne sont pas aussi simples que les précédentes. Dans le meilleur des cas, les capteurs de température mesurent la température de surface du moule. Cependant, cette mesure n'est pas bien corrélée avec la température simulée. Par conséquent, il serait intéressant d'utiliser l'apprentissage machines basés sur les données pour combler l'écart entre ces deux résultats afin de pouvoir utiliser ces données mesurées dans une application similaire à celle présentée dans cette thèse.

En guise de perspective sur le sujet de la modélisation de substitution dans le domaine de la simulation du moulage par injection, le présent travail peut être étendu pour inclure un modèle temporel et spatial complet. Celui-ci pourrait être utilisé pour visualiser et évaluer les solutions instantanément tout en faisant varier les paramètres d'entrée. De tels modèles de substitution fournissent la clé pour effectuer la quantification des incertitudes et des analyses de sensibilité efficaces. Une autre application intéressante est la création d'un jumeau numérique du processus de moulage par injection à l'aide de ces méthodologies.

Bibliography

[1] T. A. Osswald and G. Menges, *Material science of polymers for engineers*, 3rd ed. Cincinnati: Hanser Publishers, 2012.

[2] Q. Feng and X. Zhou, “Automated and robust multi-objective optimal design of thin-walled product injection process based on hybrid RBF-MOGA,” *The International Journal of Advanced Manufacturing Technology*, vol. 101, no. 9-12, pp. 2217–2231, Apr. 2019. [Online]. Available: http://link.springer.com/10.1007/s00170-018-3084-5

[3] P. Kennedy and R. Zheng, *Flow analysis of injection molds*, 2nd ed. Munich ; Cincinnati: Hanser Publishers, 2013.

[4] C. Cruz and S. Saad, “Model parameter optimization scheme using a surrogate model,” 2021.

[5] Y. Gao and X. Wang, “Surrogate-based process optimization for reducing warpage in injection molding,” *Journal of Materials Processing Technology*, vol. 209, no. 3, pp. 1302–1309, Feb. 2009. [Online]. Available: https://linkinghub.elsevier.com/retrieve/pii/S0924013608002586

[6] W. Chen, X.-h. Zhou, H.-f. Wang, and W. Wang, “Multi-objective optimal approach for injection molding based on surrogate model and particle swarm optimization algorithm,” *Journal of Shanghai Jiaotong University (Science)*, vol. 15, no. 1, pp. 88–93, Feb. 2010. [Online]. Available: http://link.springer.com/10.1007/s12204-010-9517-4

[7] C. Li, F.-L. Wang, Y.-Q. Chang, and Y. Liu, “A modified global optimization method based on surrogate model and its application in packing profile optimization of injection molding process,” *The International Journal of Advanced Manufacturing Technology*, vol. 48, no. 5-8, pp. 505–511, May 2010. [Online]. Available: http://link.springer.com/10.1007/s00170-009-2302-6

[8] J. Cheng, Z. Liu, and J. Tan, “Multiobjective optimization of injection molding parameters based on soft computing and variable complexity method,” *The International Journal of Advanced Manufacturing Technology*, vol. 66, no. 5-8, pp. 907–916, May 2013. [Online]. Available: http://link.springer.com/10.1007/s00170-012-4376-9

[9] H. Gao, Y. Zhang, X. Zhou, and D. Li, “Intelligent methods for the process parameter determination of plastic injection molding,” *Frontiers of Mechanical Engineering*, vol. 13, no. 1, pp. 85–95, Mar. 2018. [Online]. Available: http://link.springer.com/10.1007/s11465-018-0491-0

[10] H. Shi, S. Xie, and X. Wang, “A warpage optimization method for injection molding using artificial neural network with parametric sampling evaluation strategy,” *The International Journal of Advanced Manufacturing Technology*, vol. 65, no. 1-4, pp. 343–353, Mar. 2013. [Online]. Available: http://link.springer.com/10.1007/s00170-012-4173-5

[11] R. Ivan, M. Sorgato, F. Zanini, and G. Lucchetta, “Improving Numerical Modeling Accuracy for Fiber Orientation and Mechanical Properties of Injection Molded Glass Fiber Reinforced Thermoplastics,” *Materials*, vol. 15, no. 13, p. 4720, Jul. 2022. [Online]. Available: https://www.mdpi.com/1996-1944/15/13/4720

[12] M. Avrami, “Kinetics of Phase Change. I General Theory,” *The Journal of Chemical Physics*, vol. 7, no. 12, pp. 1103–1112, Dec. 1939. [Online]. Available: http://aip.scitation.org/doi/10.1063/1.1750380

[13] A. N. Kolmogotov, “A Statistical Theory for the Recrystallisation of Metals,” *Izvestiya Akademii Nauk SSSR, Neorganicheskie Materialy*, vol. 3, pp. 355–359, 1937.

[14] W. Schneider, A. Köppl, and J. Berger, “Non – Isothermal Crystallization Crystallization of Polymers: System of Rate Equations,” *International Polymer Processing*, vol. 2, no. 3-4, pp. 151–154, Mar. 1988. [Online]. Available: http://www.hanser-elibrary.com/doi/10.3139/217.880150

[15] R. Pantani, I. Coccorullo, V. Speranza, and G. Titomanlio, “Modeling of morphology evolution in the injection molding process of thermoplastic polymers,” *Progress in Polymer Science*, vol. 30, no. 12, pp. 1185–1222, Dec. 2005. [Online]. Available: https://linkinghub.elsevier.com/retrieve/pii/S0079670005001176

[16] A. Poitou and A. Ammar, “Cristallisation induite par écoulement ou par déformation d’un polymère – une approche thermodynamique,” *Comptes Rendus de l’Académie des Sciences - Series IIB - Mechanics*, vol. 329, no. 1, pp. 5–11, Jan. 2001. [Online]. Available: https://linkinghub.elsevier.com/retrieve/pii/S1620774200012903

[17] A. Poitou, A. Ammar, Y. Marco, L. Chevalier, and M. Chaouche, “Crystallization of polymers under strain: from molecular properties to macroscopic models,” *Computer Methods in Applied Mechanics and Engineering*, vol. 192, no. 28-30, pp. 3245–3264, Jul. 2003. [Online]. Available: https://linkinghub.elsevier.com/retrieve/pii/S0045782503003499

[18] R. Zheng, R. I. Tanner, and X.-J. Fan, *Injection Molding.* Berlin, Heidelberg: Springer Berlin Heidelberg, 2011, dOI: 10.1007/978-3-642-21263-5. [Online]. Available: http://link.springer.com/10.1007/978-3-642-21263-5

[19] G. H. Michler, *Electron microscopy of polymers*, ser. Springer Laboratory. Berlin: Springer, 2008, oCLC: 248616777.

[20] G. Lamberti, “Flow induced crystallisation of polymers,” *Chem. Soc. Rev.*, vol. 43, no. 7, pp. 2240–2252, 2014. [Online]. Available: http://xlink.rsc.org/?DOI=C3CS60308C

[21] F. De Santis, R. Pantani, and G. Titomanlio, “Effect of shear flow on spherulitic growth and nucleation rates of polypropylene,” *Polymer*, vol. 90, pp. 102–110, May 2016. [Online]. Available: https://linkinghub.elsevier.com/retrieve/pii/S0032386116301380

[22] H. Zuidema, “Flow induced crystallization of polymers: application to injection moulding,” PhD thesis, Technische Universiteit Eindhoven, Eindhoven, 2000, oCLC: 248341950.

[23] W. Hu, *Polymer Physics.* Vienna: Springer Vienna, 2013, dOI: 10.1007/978-3-7091-0670-9. [Online]. Available: http://link.springer.com/10.1007/978-3-7091-0670-9

[24] G. Liang, S. Bao, and F. Zhu, “Theoretical Aspects of Polymer Crystallization in Multiphase Systems,” in *Crystallization in Multiphase Polymer Systems.* Elsevier, 2018, pp. 17–48, dOI: 10.1016/B978-0-12-809453-2.00002-5. [Online]. Available: https://linkinghub.elsevier.com/retrieve/pii/B9780128094532000025

[25] M. Boutaous, P. Bourgin, and M. Zinet, “Thermally and flow induced crystallization of polymers at low shear rate,” *Journal of Non-Newtonian Fluid Mechanics*, vol. 165, no. 5-6, pp. 227–237, Mar. 2010. [Online]. Available: https://linkinghub.elsevier.com/retrieve/pii/S0377025709002353

[26] M. Zhang, B.-H. Guo, and J. Xu, “A Review on Polymer Crystallization Theories,” *Crystals*, vol. 7, no. 1, p. 4, Dec. 2016. [Online]. Available: http://www.mdpi.com/2073-4352/7/1/4

[27] R. Pantani, F. De Santis, V. Speranza, and G. Titomanlio, “Analysis of flow induced crystallization through molecular stretch,” *Polymer*, vol. 105, pp. 187–194, Nov. 2016. [Online]. Available: https://linkinghub.elsevier.com/retrieve/pii/S0032386116309375

[28] I. Coccorullo, R. Pantani, and G. Titomanlio, “Crystallization kinetics and solidified structure in iPP under high cooling rates,” *Polymer*, vol. 44, no. 1, pp. 307–318, Jan. 2003. [Online]. Available: https://linkinghub.elsevier.com/retrieve/pii/S0032386102007620

[29] H. Zuidema, G. W. Peters, and H. E. Meijer, “Development and validation of a recoverable strain-based model for flow-induced crystallization of polymers,” *Macromolecular theory and simulations*, vol. 10, no. 5, pp. 447–460, 2001. [Online]. Available: https://onlinelibrary.wiley.com/doi/abs/10.1002/1521-3919(20010601)10:5%3C447::AID-MATS447%3E3.0.CO;2-C

[30] R. Zheng, R. I. Tanner, D. L. Wo, X.-j. Fan, C. Hadinata, F. S. Costa, P. K. Kennedy, P. Zhu, and G. Edward, “Modeling of flow-induced crystallization of colored polypropylene in injection molding,” *Korea-Australia Rheology Journal*, vol. 22, no. 3, pp. 151–162, 2010. [Online]. Available: http://images.autodesk.com/apac_japan_main/files/kr22-03-0001.pdf

[31] R. Pantani, V. Speranza, and G. Titomanlio, “Thirty years of modeling of injection molding. a brief review of the contribution of UNISA code to the field,” *International Polymer Processing*, vol. 31, no. 5, pp. 655–663, 2016. [Online]. Available: https://www.hanser-elibrary.com/doi/abs/10.3139/217.3249

[32] E. Troisi, S. Arntz, P. Roozemond, A. Tsou, and G. Peters, “Application of a multi-phase multi-morphology crystallization model to isotactic polypropylenes with different molecular weight distributions,” *European Polymer Journal*, vol. 97, pp. 397–408, Dec. 2017. [Online]. Available: https://linkinghub.elsevier.com/retrieve/pii/S0014305717309722

[33] T. Parenteau, G. Ausias, Y. Grohens, and P. Pilvin, “Structure, mechanical properties and modelling of polypropylene for different degrees of crystallinity,” *Polymer*, vol. 53, no. 25, pp. 5873–5884, Nov. 2012. [Online]. Available: https://linkinghub.elsevier.com/retrieve/pii/S0032386112008385

[34] R. Pantani, V. Speranza, and G. Titomanlio, “Effect of flow-induced crystallization on the distribution of spherulite dimensions along cross section of injection molded parts,” *European Polymer Journal*, vol. 97, pp. 220–229, Dec. 2017. [Online]. Available: https://linkinghub.elsevier.com/retrieve/pii/S0014305717311618

[35] P. C. Roozemond, M. van Drongelen, Z. Ma, M. A. Hulsen, and G. W. Peters, “Modeling flow-induced crystallization in isotactic polypropylene at high shear rates,” *Journal of rheology*, vol. 59, no. 3, pp. 613–642, 2015. [Online]. Available: https://sor.scitation.org/doi/abs/10.1122/1.4913696

[36] E. Koscher and R. Fulchiron, “Influence of shear on polypropylene crystallization: morphology development and kinetics,” *Polymer*, vol. 43, no. 25, pp. 6931–6942, 2002. [Online]. Available: https://www.sciencedirect.com/science/article/pii/S0032386102006286

[37] Y. Mu, G. Zhao, A. Chen, G. Dong, and S. Li, “Numerical investigation of the crystallization and orientation behavior in polymer processing with a two-phase model,” *Computers & Chemical Engineering*, vol. 63, pp. 91–107, Apr. 2014. [Online]. Available: https://linkinghub.elsevier.com/retrieve/pii/S0098135413003918

[38] A. Toda, R. Androsch, and C. Schick, “Insights into polymer crystallization and melting from fast scanning chip calorimetry,” *Polymer*, vol. 91, pp. 239–263, May 2016. [Online]. Available: https://linkinghub.elsevier.com/retrieve/pii/S0032386116301781

[39] A. I. Isayev, T. W. Chan, M. Gmerek, and K. Shimojo, “Injection molding of semicrystalline polymers. II. Modeling and experiments,” *Journal of applied polymer science*, vol. 55, no. 5, pp. 821–838, 1995. [Online]. Available: https://onlinelibrary.wiley.com/doi/abs/10.1002/app.1995.070550519

[40] J. Guo and K. A. Narh, “Computer simulation of stress-induced crystallization in injection molded thermoplastics,” *Polymer Engineering & Science*, vol. 41, no. 11, pp. 1996–2012, 2001. [Online]. Available: https://onlinelibrary.wiley.com/doi/abs/10.1002/pen.10896

[41] U. R. Evans, “The laws of expanding circles and spheres in relation to the lateral growth of surface films and the grain-size of metals,” *Transactions of the Faraday Society*, vol. 41, p. 365, 1945. [Online]. Available: http://xlink.rsc.org/?DOI=tf9454100365

[42] S. Coppola, L. Balzano, E. Gioffredi, P. L. Maffettone, and N. Grizzuti, “Effects of the degree of undercooling on flow induced crystallization in polymer melts,” *Polymer*, vol. 45, no. 10, pp. 3249–3256, May 2004. [Online]. Available: https://linkinghub.elsevier.com/retrieve/pii/S0032386104002733

[43] J. I. Lauritzen and J. D. Hoffman, “Theory of formation of polymer crystals with folded chains in dilute solution,” *Journal of Research of the National Bureau of Standards Section A: Physics and Chemistry*, vol. 64A, no. 1, p. 73, Jan. 1960. [Online]. Available: https://nvlpubs.nist.gov/nistpubs/jres/64A/jresv64An1p73_A1b.pdf

[44] T. Ozawa, “Kinetics of non-isothermal crystallization,” *Polymer*, vol. 12, no. 3, pp. 150–158, Mar. 1971. [Online]. Available: https://linkinghub.elsevier.com/retrieve/pii/0032386171900413

[45] K. Nakamura, T. Watanabe, K. Katayama, and T. Amano, “Some aspects of nonisothermal crystallization of polymers. I. Relationship between crystallization temperature, crystallinity, and cooling conditions,” *Journal of Applied Polymer Science*, vol. 16, no. 5, pp. 1077–1091, May 1972. [Online]. Available: http://doi.wiley.com/10.1002/app.1972.070160503

[46] A. K. Doufas, A. J. McHugh, and C. Miller, “Simulation of melt spinning including flow-induced crystallization: Part I. Model development and predictions,” *Journal of Non-Newtonian Fluid Mechanics*, vol. 92, no. 1, pp. 27–66, 2000. [Online]. Available: https://www.sciencedirect.com/science/article/pii/S0377025700000884

[47] M. Zinet, R. El Otmani, M. Boutaous, and P. Chantrenne, “Numerical modeling of nonisothermal polymer crystallization kinetics: Flow and thermal effects,” *Polymer Engineering & Science*, vol. 50, no. 10, pp. 2044–2059, Oct. 2010. [Online]. Available: http://doi.wiley.com/10.1002/pen.21733

[48] J. A. Kulkarni and A. N. Beris, “Lattice-based simulations of chain conformations in semi-crystalline polymers with application to flow-induced crystallization,” *Journal of Non-Newtonian Fluid Mechanics*, vol. 82, no. 2-3, pp. 331–366, May 1999. [Online]. Available: https://linkinghub.elsevier.com/retrieve/pii/S0377025798001712

[49] R. I. Tanner and F. Qi, “A comparison of some models for describing polymer crystallization at low deformation rates,” *Journal of Non-Newtonian Fluid Mechanics*, vol. 127, no. 2-3, pp. 131–141, May 2005. [Online]. Available: https://linkinghub.elsevier.com/retrieve/pii/S0377025705000583

[50] N. Brahmia, “Contribution à la modélisation de la cristallisation des polymères sous cisaillement: application à l’injection des polymères semi-cristallins,” Ph.D. dissertation, PhD Thesis INSA de Lyon, France, 2007. [Online]. Available: http://theses.insa-lyon.fr/publication/2007ISAL0069/these.pdf

[51] Y. Mu, G. Zhao, A. Chen, and X. Wu, “Numerical investigation of the thermally and flow induced crystallization behavior of semi-crystalline polymers by using finite element–finite difference method,” *Computers & Chemical Engineering*, vol. 46, pp. 190–204, Nov. 2012. [Online]. Available: https://linkinghub.elsevier.com/retrieve/pii/S0098135412002104

[52] T. W. Haas and B. Maxwell, “Effects of shear stress on the crystallization of linear polyethylene and polybutene-1,” *Polymer Engineering and Science*, vol. 9, no. 4, pp. 225–241, Jul. 1969. [Online]. Available: https://onlinelibrary.wiley.com/doi/10.1002/pen.760090402

[53] G. Titomanlio, V. Speranza, and V. Brucato, “On the Simulation of Thermoplastic Injection Moulding Process: II Relevance of Interaction Between Flow and Crystallization,” *International Polymer Processing*, vol. 12, no. 1, pp. 45–53, Mar. 1997. [Online]. Available: https://www.degruyter.com/document/doi/10.3139/217.970045/html

[54] J. Guo and K. A. Narh, “Simplified model of stress-induced crystallization kinetics of polymers,” *Advances in Polymer Technology*, vol. 21, no. 3, pp. 214–222, 2002. [Online]. Available: http://doi.wiley.com/10.1002/adv.10022

[55] G. Titomanlio and G. Lamberti, “Modeling flow induced crystallization in film casting of polypropylene,” *Rheologica Acta*, vol. 43, no. 2, pp. 146–158, Mar. 2004. [Online]. Available: http://link.springer.com/10.1007/s00397-003-0329-4

[56] K. H. Kim, A. Isayev, K. Kwon, and C. van Sweden, “Modeling and experimental study of birefringence in injection molding of semicrystalline polymers,” *Polymer*, vol. 46, no. 12, pp. 4183–4203, May 2005. [Online]. Available: https://linkinghub.elsevier.com/retrieve/pii/S0032386105002077

[57] G. Eder, H. Janeschitz-Kriegl, and S. Liedauer, “Crystallization processes in quiescent and moving polymer melts under heat transfer conditions,” *Progress in Polymer Science*, vol. 15, no. 4, pp. 629–714, Jan. 1990. [Online]. Available: https://linkinghub.elsevier.com/retrieve/pii/007967009090008O

[58] S. K. Kim and A. Jeong, “Numerical Simulation of Crystal Growth in Injection Molded Thermoplastics based on Monte Carlo Method with Shear Rate Tracking,” *International Journal of Precision Engineering and Manufacturing*, vol. 20, no. 4, pp. 641–650, Apr. 2019. [Online]. Available: http://link.springer.com/10.1007/s12541-019-00089-x

[59] J. van Meerveld, M. Hütter, and G. W. Peters, “Continuum model for the simulation of fiber spinning, with quiescent and flow-induced crystallization,” *Journal of Non-Newtonian Fluid Mechanics*, vol. 150, no. 2-3, pp. 177–195, Apr. 2008. [Online]. Available: https://linkinghub.elsevier.com/retrieve/pii/S0377025707002340

[60] M. Zinet, Z. Refaa, M. Boutaous, S. Xin, and P. Bourgin, “Thermophysical Characterization and Crystallization Kinetics of Semi-Crystalline Polymers,” *Journal of Modern Physics*, vol. 04, no. 07, pp. 28–37, 2013. [Online]. Available: http://www.scirp.org/journal/doi.aspx?DOI=10.4236/jmp.2013.47A2005

[61] P. C. Roozemond, T. B. van Erp, and G. W. Peters, “Flow-induced crystallization of isotactic polypropylene: Modeling formation of multiple crystal phases and morphologies,” *Polymer*, vol. 89, pp. 69–80, Apr. 2016. [Online]. Available: https://linkinghub.elsevier.com/retrieve/pii/S0032386116300325

[62] S. Acierno, S. Coppola, N. Grizzuti, and P. L. Maffettone, “Coupling between kinetics and rheological parameters in the flow-induced crystallization of thermoplastic polymers,” *Macromolecular Symposia*, vol. 185, no. 1, pp. 233–241, Aug. 2002. [Online]. Available: https://onlinelibrary.wiley.com/doi/10.1002/1521-3900(200208)185:1<233::AID-MASY233>3.0.CO;2-W

[63] R. Zheng and P. K. Kennedy, “A model for post-flow induced crystallization: General equations and predictions,” *Journal of Rheology*, vol. 48, no. 4, pp. 823–842, Jul. 2004. [Online]. Available: http://sor.scitation.org/doi/10.1122/1.1763944

[64] G. Laschet, M. Spekowius, R. Spina, and C. Hopmann, “Multiscale simulation to predict microstructure dependent effective elastic properties of an injection molded polypropylene component,” *Mechanics of Materials*, vol. 105, pp. 123–137, Feb. 2017. [Online]. Available: https://linkinghub.elsevier.com/retrieve/pii/S0167663616304240

[65] T. Schrank, M. Berer, B. Haar, B. Ramoa, T. Lucyshyn, M. Feuchter, G. Pinter, V. Speranza, and R. Pantani, “Injection Molding Simulation of Polyoxymethylene Using Crystallization Kinetics Data and Comparison with the Experimental Process,” *Polymer Crystallization*, vol. 2022, pp. 1–15, Mar. 2022. [Online]. Available: https://www.hindawi.com/journals/pcrys/2022/2387752/

[66] C. A. Hieber, “Correlations for the quiescent crystallization kinetics of isotactic polypropylene and poly (ethylene terephthalate),” *Polymer*, vol. 36, no. 7, pp. 1455–1467, 1995. [Online]. Available: https://www.sciencedirect.com/science/article/pii/003238619595925Q

[67] T. Kitano, T. Kataoka, and T. Shirota, “An empirical equation of the relative viscosity of polymer melts filled with various inorganic fillers,” *Rheologica Acta*, vol. 20, no. 2, pp. 207–209, Mar. 1981. [Online]. Available: http://link.springer.com/10.1007/BF01513064

[68] A. B. Metzner, “Rheology of Suspensions in Polymeric Liquids,” *Journal of Rheology*, vol. 29, no. 6, pp. 739–775, Dec. 1985. [Online]. Available: http://sor.scitation.org/doi/10.1122/1.549808

[69] A. Ziabicki, “Crystallization of polymers in variable external conditions: 1. General equations,” *Colloid & Polymer Science*, vol. 274, no. 3, pp. 209–217, Mar. 1996. [Online]. Available: http://link.springer.com/10.1007/BF00665637

[70] R. I. Tanner, “On the flow of crystallizing polymers,” *Journal of Non-Newtonian Fluid Mechanics*, vol. 112, no. 2-3, pp. 251–268, Jun. 2003. [Online]. Available: https://linkinghub.elsevier.com/retrieve/pii/S0377025703001046

[71] G. Lamberti, G. W. M. Peters, and G. Titomanlio, “Crystallinity and Linear Rheological Properties of Polymers,” *International Polymer Processing*, vol. 22, no. 3, pp. 303–310, Jul. 2007. [Online]. Available: http://www.hanser-elibrary.com/doi/abs/10.3139/217.2006

[72] J.-F. Luye, G. Regnier, P. Le Bot, D. Delaunay, and R. Fulchiron, “PVT measurement methodology for semicrystalline polymers to simulate injection-molding process,” *Journal of Applied Polymer Science*, vol. 79, no. 2, pp. 302–311, Jan. 2001. [Online]. Available: https://onlinelibrary.wiley.com/doi/10.1002/1097-4628(20010110)79:2<302::AID-APP120>3.0.CO;2-I

[73] R. Fulchiron, E. Koscher, G. Poutot, D. Delaunay, and G. Régnier, “Analysis of the pressure effect on the crystallization kinetics of polypropylene: dilatometric measurements and thermal gradient modeling,” *Journal of Macromolecular Science, Part B*, vol. 40, no. 3-4, pp. 297–314, 2001. [Online]. Available: https://www.tandfonline.com/doi/abs/10.1081/MB-100106159

[74] P. Zhao, W. Yang, X. Wang, J. Li, B. Yan, and J. Fu, “A novel method for predicting degrees of crystallinity in injection molding during packing stage,” *Proceedings of the Institution of Mechanical Engineers, Part B: Journal of Engineering Manufacture*, vol. 233, no. 1, pp. 204–214, 2017. [Online]. Available: http://journals.sagepub.com/doi/10.1177/0954405417718593

[75] P. S. Cook, Z. Zuo, and F. S. Costa, “A research framework for cooling rate-dependent PVT models,” in *Proceedings of the Technical Conference & Exhibition.* Indianapolis, Indiana, USA: Society of Plastics Engineers (SPE), 2016. [Online]. Available: https://www.researchgate.net/profile/Zhihao-Zuo/publication/303703576_A_RESEARCH_FRAMEWORK_FOR_COOLING_RATE-DEPENDENT_PVT_MODELS/links/574ed9bb08aefc38ba120d6a/A-RESEARCH-FRAMEWORK-FOR-COOLING-RATE-DEPENDENT-PVT-MODELS.pdf

[76] J. Wang, C. Hopmann, M. Röbig, T. Hohlweck, C. Kahve, and J. Alms, “Continuous Two-Domain Equations of State for the Description of the Pressure-Specific Volume-Temperature Behavior of Polymers,” *Polymers*, vol. 12, no. 2, p. 409, Feb. 2020. [Online]. Available: https://www.mdpi.com/2073-4360/12/2/409

[77] C. Hopmann, C. Xiao, C. E. Kahve, and J. Fellerhoff, “Prediction and validation of the specific volume for inline warpage control in injection molding,” *Polymer Testing*, vol. 104, p. 107393, Dec. 2021. [Online]. Available: https://linkinghub.elsevier.com/retrieve/pii/S014294182100338X

[78] S. Hijazi, G. Stabile, A. Mola, and G. Rozza, “Data-driven POD-Galerkin reduced order model for turbulent flows,” *Journal of Computational Physics*, vol. 416, Sep. 2020. [Online]. Available: https://linkinghub.elsevier.com/retrieve/pii/S0021999120302874

[79] F. Chinesta, A. Leygue, F. Bordeu, J. V. Aguado, E. Cueto, D. Gonzalez, I. Alfaro, A. Ammar, and A. Huerta, “PGD-Based Computational Vademecum for Efficient Design, Optimization and Control,” *Archives of Computational Methods in Engineering*, vol. 20, no. 1, pp. 31–59, Mar. 2013. [Online]. Available: http://link.springer.com/10.1007/s11831-013-9080-x

[80] G. G. Wang and S. Shan, “Review of Metamodeling Techniques in Support of Engineering Design Optimization,” *Journal of Mechanical Design*, vol. 129, no. 4, pp. 370–380, Apr. 2007. [Online]. Available: https://asmedigitalcollection.asme.org/mechanicaldesign/article/129/4/370/466824/Review-of-Metamodeling-Techniques-in-Support-of

[81] A. I. Forrester and A. J. Keane, “Recent advances in surrogate-based optimization,” *Progress in Aerospace Sciences*, vol. 45, no. 1-3, pp. 50–79, Jan. 2009. [Online]. Available: https://linkinghub.elsevier.com/retrieve/pii/S0376042108000766

[82] E. Iuliano and D. Quagliarella, “Proper Orthogonal Decomposition, surrogate modelling and evolutionary optimization in aerodynamic design,” *Computers & Fluids*, vol. 84, pp. 327–350, Sep. 2013. [Online]. Available: https://linkinghub.elsevier.com/retrieve/pii/S0045793013002223

[83] T. Simpson, J. Poplinski, P. N. Koch, and J. Allen, “Metamodels for Computer-based Engineering Design: Survey and recommendations,” *Engineering with Computers*, vol. 17, no. 2, pp. 129–150, Jul. 2001. [Online]. Available: http://link.springer.com/10.1007/PL00007198

[84] S. Razavi, B. A. Tolson, and D. H. Burn, “Review of surrogate modeling in water resources: REVIEW,” *Water Resources Research*, vol. 48, no. 7, Jul. 2012. [Online]. Available: http://doi.wiley.com/10.1029/2011WR011527

[85] A. Giunta, S. Wojtkiewicz, and M. Eldred, “Overview of Modern Design of Experiments Methods for Computational Simulations.” American Institute of Aeronautics and Astronautics, Jan. 2003. [Online]. Available: https://arc.aiaa.org/doi/10.2514/6.2003-649

[86] R. G. McClarren, *Uncertainty Quantification and Predictive Computational Science: A Foundation for Physical Scientists and Engineers*, 1st ed. Cham: Springer International Publishing : Imprint: Springer, 2018.

[87] W. Jank, “Quasi-Monte Carlo sampling to improve the efficiency of Monte Carlo EM,” *Computational Statistics & Data Analysis*, vol. 48, no. 4, pp. 685–701, Apr. 2005. [Online]. Available: https://linkinghub.elsevier.com/retrieve/pii/S0167947304001033

[88] N. Metropolis and S. Ulam, “The Monte Carlo Method,” *Journal of the American Statistical Association*, vol. 44, no. 247, pp. 335–341, Sep. 1949. [Online]. Available: http://www.tandfonline.com/doi/abs/10.1080/01621459.1949.10483310

[89] J. H. Halton, “On the efficiency of certain quasi-random sequences of points in evaluating multi-dimensional integrals,” *Numerische Mathematik*, vol. 2, no. 1, pp. 84–90, Dec. 1960. [Online]. Available: http://link.springer.com/10.1007/BF01386213

[90] H. Niederreiter, Society for Industrial and Applied Mathematics, *Random number generation and quasi-Monte Carlo methods: Author's expanded lecture notes from his talks at the NSF-CBMS Regional Research Conference on Random Number Generation and Quasi-Monte Carlo Methods held at the University of Alaska at Fairbanks, Aug. 13-17, 1990.* Philadelphia, Pa.: Society for Industrial and Applied Mathematics, 1992, oCLC: 775728856.

[91] I. Sobol, “On the distribution of points in a cube and the approximate evaluation of integrals,” *USSR Computational Mathematics and Mathematical Physics*, vol. 7, no. 4, pp. 86–112, Jan. 1967. [Online]. Available: https://linkinghub.elsevier.com/retrieve/pii/0041555367901449

[92] H. Faure, P. Kritzer, and F. Pillichshammer, “From van der Corput to modern constructions of sequences for quasi-Monte Carlo rules,” *Indagationes Mathematicae*, vol. 26, no. 5, pp. 760–822, Dec. 2015. [Online]. Available: https://linkinghub.elsevier.com/retrieve/pii/S0019357715000683

[93] A. Nouy, “A priori model reduction through Proper Generalized Decomposition for solving time-dependent partial differential equations,” *Computer Methods in Applied Mechanics*

and Engineering, vol. 199, no. 23-24, pp. 1603–1626, Apr. 2010. [Online]. Available: https://linkinghub.elsevier.com/retrieve/pii/S0045782510000186

[94] D. Ryckelynck, F. Chinesta, E. Cueto, and A. Ammar, "On the a priori model reduction: Overview and recent developments," *Archives of Computational methods in Engineering*, vol. 13, no. 1, pp. 91–128, 2006. [Online]. Available: https://link.springer.com/article/10.1007/BF02905932

[95] J. Du, F. Fang, C. Pain, I. Navon, J. Zhu, and D. Ham, "POD reduced-order unstructured mesh modeling applied to 2d and 3d fluid flow," *Computers & Mathematics with Applications*, vol. 65, no. 3, pp. 362–379, Feb. 2013. [Online]. Available: https://linkinghub.elsevier.com/retrieve/pii/S0898122112004397

[96] T. Simpson, V. Toropov, V. Balabanov, and F. Viana, "Design and analysis of computer experiments in multidisciplinary design optimization: a review of how far we have come-or not," in *12th AIAA/ISSMO multidisciplinary analysis and optimization conference*, 2008, p. 5802. [Online]. Available: https://arc.aiaa.org/doi/pdf/10.2514/6.2008-5802

[97] R. Alizadeh, J. K. Allen, and F. Mistree, "Managing computational complexity using surrogate models: a critical review," *Research in Engineering Design*, vol. 31, no. 3, pp. 275–298, Jul. 2020. [Online]. Available: http://link.springer.com/10.1007/s00163-020-00336-7

[98] W. Liu, X. Wang, Z. Li, J. Gu, S. ruan, C. Shen, and X. Wang, "Integration optimization of molding and service for injection-molded product," *The International Journal of Advanced Manufacturing Technology*, vol. 84, no. 9-12, pp. 2019–2028, Jun. 2016. [Online]. Available: http://link.springer.com/10.1007/s00170-015-7862-z

[99] P. Zhao, J. Zhang, Z. Dong, J. Huang, H. Zhou, J. Fu, and L.-S. Turng, "Intelligent Injection Molding on Sensing, Optimization, and Control," *Advances in Polymer Technology*, vol. 2020, pp. 1–22, Mar. 2020. [Online]. Available: https://www.hindawi.com/journals/apt/2020/7023616/

[100] R. Teixeira, M. Nogal, and A. O'Connor, "Adaptive approaches in metamodel-based reliability analysis: A review," *Structural Safety*, vol. 89, p. 102019, Mar. 2021. [Online]. Available: https://linkinghub.elsevier.com/retrieve/pii/S0167473020300989

[101] L. L. Gratiet, S. Marelli, and B. Sudret, "Metamodel-Based Sensitivity Analysis: Polynomial Chaos Expansions and Gaussian Processes," in *Handbook of Uncertainty Quantification*, R. Ghanem, D. Higdon, and H. Owhadi, Eds. Cham: Springer International Publishing, 2015, pp. 1–37, dOI: 10.1007/978-3-319-11259-6_38-1. [Online]. Available: http://link.springer.com/10.1007/978-3-319-11259-6_38-1

[102] T. Crestaux, O. Le Maıˆtre, and J.-M. Martinez, "Polynomial chaos expansion for sensitivity analysis," *Reliability Engineering & System Safety*, vol. 94, no. 7, pp. 1161–1172, Jul. 2009. [Online]. Available: https://linkinghub.elsevier.com/retrieve/pii/S0951832008002561

[103] J. Nossent, P. Elsen, and W. Bauwens, "Sobol sensitivity analysis of a complex environmental model," *Environmental Modelling & Software*, vol. 26, no. 12, pp. 1515–1525, Dec. 2011. [Online]. Available: https://linkinghub.elsevier.com/retrieve/pii/S1364815211001939

[104] I. Sobol, "Global sensitivity indices for nonlinear mathematical models and their Monte Carlo estimates," *Mathematics and Computers in Simulation*, vol. 55, no. 1-3, pp. 271–280, Feb. 2001. [Online]. Available: https://linkinghub.elsevier.com/retrieve/pii/S0378475400002706

[105] R. Rosolem, H. V. Gupta, W. J. Shuttleworth, X. Zeng, and L. G. G. de Gonçalves, "A fully multiple-criteria implementation of the Sobol method for parameter sensitivity analysis: MULTICRITERIA SOBOL SENSITIVITY ANALYSIS," *Journal of Geophysical Research: Atmospheres*, vol. 117, no. D7, pp. n/a–n/a, Apr. 2012. [Online]. Available: http://doi.wiley.com/10.1029/2011JD016355

[106] X. Wang, J. Gu, C. Shen, and X. Wang, "Warpage optimization with dynamic injection molding technology and sequential optimization method," *The International Journal of Advanced Manufacturing Technology*, vol. 78, no. 1-4, pp. 177–187, Apr. 2015. [Online]. Available: http://link.springer.com/10.1007/s00170-014-6621-x

[107] G.-J. Kang, C.-H. Park, and D.-H. Choi, "Metamodel-based design optimization of injection molding process variables and gates of an automotive glove box for enhancing its quality," *Journal of Mechanical Science and Technology*, vol. 30, no. 4, pp. 1723–1732, Apr. 2016. [Online]. Available: http://link.springer.com/10.1007/s12206-016-0328-x

[108] S. Kitayama, H. Miyakawa, M. Takano, and S. Aiba, “Multi-objective optimization of injection molding process parameters for short cycle time and warpage reduction using conformal cooling channel,” *The International Journal of Advanced Manufacturing Technology*, vol. 88, no. 5-8, pp. 1735–1744, Feb. 2017. [Online]. Available: http://link.springer.com/10.1007/s00170-016-8904-x

[109] W. Xia, B. Luo, and X.-p. Liao, “An enhanced optimization approach based on Gaussian process surrogate model for process control in injection molding,” *The International Journal of Advanced Manufacturing Technology*, vol. 56, no. 9-12, pp. 929–942, Oct. 2011. [Online]. Available: http://link.springer.com/10.1007/s00170-011-3227-4

[110] M. G. Villarreal-Marroquín, J. D. Svenson, F. Sun, T. J. Santner, A. Dean, and J. M. Castro, “A comparison of two metamodel-based methodologies for multiple criteria simulation optimization using an injection molding case study,” *Journal of Polymer Engineering*, vol. 33, no. 3, pp. 193–209, May 2013. [Online]. Available: https://www.degruyter.com/document/doi/10.1515/polyeng-2013-0022/html

[111] G. Xu and Z. Yang, “Multiobjective optimization of process parameters for plastic injection molding via soft computing and grey correlation analysis,” *The International Journal of Advanced Manufacturing Technology*, vol. 78, no. 1-4, pp. 525–536, Apr. 2015. [Online]. Available: http://link.springer.com/10.1007/s00170-014-6643-4

[112] S. M. S. Mukras, H. M. Omar, and F. A. al Mufadi, “Experimental-Based Multi-objective Optimization of Injection Molding Process Parameters,” *Arabian Journal for Science and Engineering*, vol. 44, no. 9, pp. 7653–7665, Sep. 2019. [Online]. Available: http://link.springer.com/10.1007/s13369-019-03855-1

[113] J. Li, Y. Wang, X. Wang, and D. Wu, “Development of Polyoxymethylene/Polylactide Blends for a Potentially Biodegradable Material: Crystallization Kinetics, Lifespan Prediction, and Enzymatic Degradation Behavior,” *Polymers*, vol. 11, no. 9, p. 1516, Sep. 2019. [Online]. Available: https://www.mdpi.com/2073-4360/11/9/1516

[114] A. Durmus, A. Kasgoz, N. Ercan, D. Akın, and S. Şanlı, “Effect of polyhedral oligomeric silsesquioxane (POSS) reinforced polypropylene (PP) nanocomposite on the microstructure and isothermal crystallization kinetics of polyoxymethylene (POM),” *Polymer*, vol. 53, no. 23,

pp. 5347–5357, Oct. 2012. [Online]. Available: https://linkinghub.elsevier.com/retrieve/pii/S003238611200794X

[115] S. R. Sandler, "Differential Scanning Calorimetry," in *Polymer synthesis and characterization: a laboratory manual.* San Diego: Academic Press, 1998, pp. 120–130.

[116] N. P. Cheremisinoff, "Thermal Analysis," in *Polymer characterization: laboratory techniques and analysis.* Westwood, N.J: Noyes Publications, 1996, pp. 17–24.

[117] M. M. Cross, "Rheology of non-Newtonian fluids: A new flow equation for pseudoplastic systems," *Journal of Colloid Science*, vol. 20, no. 5, pp. 417–437, Jun. 1965. [Online]. Available: https://linkinghub.elsevier.com/retrieve/pii/009585226590022X

[118] M. L. Williams, R. F. Landel, and J. D. Ferry, "The Temperature Dependence of Relaxation Mechanisms in Amorphous Polymers and Other Glass-forming Liquids," *Journal of the American Chemical Society*, vol. 77, no. 14, pp. 3701–3707, Jul. 1955. [Online]. Available: https://pubs.acs.org/doi/abs/10.1021/ja01619a008

[119] T. Nguyen-Chung, G. Jüttner, C. Löser, T. Pham, and M. Gehde, "Determination of the heat transfer coefficient from short-shots studies and precise simulation of microinjection molding," *Polymer Engineering & Science*, vol. 50, no. 1, pp. 165–173, Jan. 2010. [Online]. Available: https://onlinelibrary.wiley.com/doi/10.1002/pen.21536

[120] M. Stricker and G. Steinbichler, "Determination of heat transfer coefficients at the polymer-mold-interface for injection molding simulation by means of calorimetry," 2014, pp. 137–141. [Online]. Available: http://aip.scitation.org/doi/abs/10.1063/1.4873750

[121] S. Kleindel, R. Eder, H. Schretter, and C. Hochenauer, "The Elastic Mold Deformation During the Filling and Packing Stage of the Injection Molding Process," *Smart Science*, vol. 2, no. 1, pp. 44–53, Jan. 2014. [Online]. Available: http://www.tandfonline.com/doi/full/10.1080/23080477.2014.11665603

[122] Y. Spoerer, R. Boldt, R. Androsch, and I. Kuehnert, "Pressure- and Temperature-Dependent Crystallization Kinetics of Isotactic Polypropylene under Process Relevant Conditions," *Crystals*, vol. 11, no. 9, p. 1138, Sep. 2021. [Online]. Available: https://www.mdpi.com/2073-4352/11/9/1138

[123] B. Efron, “Nonparametric estimates of standard error: The jackknife, the bootstrap and other methods,” *Biometrika*, vol. 68, no. 3, pp. 589–599, 1981. [Online]. Available: https://academic.oup.com/biomet/article-lookup/doi/10.1093/biomet/68.3.589

[124] K. F. Wissbrun, “The equilibrium melting point of polyoxymethylene,” *Journal of Polymer Science Part A-2: Polymer Physics*, vol. 4, no. 5, pp. 827–829, 1966. [Online]. Available: https://onlinelibrary.wiley.com/doi/abs/10.1002/pol.1966.160040513

[125] N. M. Rudolph, A. C. Agudelo, J. C. Granada, H. E. Park, and T. A. Osswald, “WLF model for the pressure dependence of zero shear viscosity of polycarbonate,” *Rheologica Acta*, vol. 55, no. 8, pp. 673–681, Aug. 2016. [Online]. Available: http://link.springer.com/10.1007/s00397-016-0945-4

[126] Autodesk, “Autodesk Knowledge Network,” 2021. [Online]. Available: https://knowledge.autodesk.com/support/moldflow-insight/learn

[127] C. J. G. Plummer and H.-H. Kausch, “A DSC investigation of the crystallization kinetics of polyoxymethylene,” *Polymer Bulletin*, vol. 32, no. 1, pp. 117–124, 1994. [Online]. Available: https://link.springer.com/article/10.1007/BF00297423

[128] ——, “DSC non-isothermal crystallization curves in polyoxymethylene,” *Colloid and Polymer Science*, vol. 273, no. 3, pp. 227–232, 1995. [Online]. Available: https://link.springer.com/article/10.1007/BF00657828

Appendix A

Cross-WLF Viscosity Model

The Cross-WLF viscosity model [117] describes the temperature, shear rate, and pressure dependency of the viscosity for thermoplastic materials. This model is used in Autodesk Moldflow Insight 2021.1 to calculate the viscosity of the polymer during its injection molding.

$$\eta = \frac{\eta_0}{1 + (\frac{\eta_0 \dot{\gamma}}{\tau^*})^{1-n}} \tag{A.1}$$

where:

- η is the viscosity of the melt,
- η_0 is the zero shear viscosity,
- $\dot{\gamma}$ is the shear rate,
- τ^* is the critical stress at the transition to shear thinning,
- n is the power law index in the high shear rate regime.

The zero shear viscosity parameter, η_0, in the above equation is given by the WLF model [118]:

$$\eta_0 = D_1 \exp\left[-\frac{A_1(T - T^*)}{A_2 + (T - T^*)}\right] \tag{A.2}$$

where:

- T is the temperature,
- $T^* = D_2 + D_3 P$ is the glass transition temperature,

- $A_2 = A_3 + D_3 P$,
- P is the pressure,
- A_1, A_2, D_1, D_2 and D_3 are data-fitted coefficients.

Sandra Saad

Towards the use of surrogate modeling in model parameter calibration in injection molding process simulation

Résumé : Les coûts de calcul des simulations du procédé de moulage par injection ont augmenté au cours des dernières années en raison de la complexité accrue des modèles intégrés. Ceci est particulièrement problématique pour des calculs d'optimisation de pièces ou pour les analyses de sensibilité de paramètres. Une façon de surmonter ce problème est d'implémenter des métamodèles pour réaliser ces simulations haute-fidélités. Ces métamodèles peuvent jouer un rôle important dans le cas du moulage par injection de polymères semi-cristallins pour modéliser le processus de cristallisation induit par l'écoulement. À ce jour, la plupart des logiciels commerciaux ne prennent pas explicitement en compte la cristallisation des polymères, ce qui conduit à diverses erreurs dans les prédictions de remplissage, d'évolution des champs de contraintes et dans les prédictions dimensionnelles. La faisabilité de l'utilisation des métamodèles pour identifier les paramètres d'un modèle physique est d'abord présentée. Il s'en suit la mise en œuvre d'un modèle de cristallisation thermo-mécanique afin de décrire la cristallisation induite par l'écoulement d'un matériau thermoplastique semi-cristallin non renforcé pendant le procédé de moulage par injection. Le modèle de cristallisation est couplé aux modèles de viscosité et PVT dans le logiciel commercial Autodesk® Moldflow® Insight 2021 en utilisant la fonction Solver API. Les paramètres du modèle sont identifiés à l'aide d'un schéma de recalage qui utilise trois différents métamodèles représentant les résultats de pression simulés pour effectuer une optimisation multi-objectifs. Les prédictions de remplissage ainsi que les pressions calculées sont présentées en utilisant les paramètres du modèle calibré en comparaison avec celles mesurées pendant le moulage par injection réel d'une pièce en polyoxyméthylène avec différentes conditions de processus. Les résultats montrent des améliorations majeures dans les prédictions des signaux de pression ainsi que dans l'état de remplissage des pièces produites et les épaisseurs estimées de la couche de peau formée dans des conditions de cisaillement élevé. Les modèles recalés sont testés en utilisant différentes géométries de moules pour évaluer leurs performances.

Mots clés : modélisation de substitution, moulage par injection, cristallisation, simulation, thermoplastique, paramètre de modèle, métamodèle.

Abstract: The computational costs of injection molding simulations have been increasing in the past years due to the higher complexity of the embedded models. This is especially problematic in case of using such simulation models for optimization routines or sensitivity analyses. One way to overcome this challenge is by having a surrogate model, also known as a metamodel, of these high-fidelity simulations, which provides a cheaper way to perform these types of analyses. These surrogate models can play an important role in the case of the injection molding of semi-crystalline polymers to model the flow-induced crystallization process. To date, most commercial software do not explicitly take polymer crystallization into account leading to various errors in the fill predictions as well as the calculation of warpage and shrinkage. This is mainly due to the common complexity of the models used to describe crystallization and the challenging respective model parameter identification process under injection molding conditions. To close this gap, in this thesis, the feasibility of using surrogate modeling to identify modeling parameters is first studied. This is then followed by the implementation of a thermo-mechanical crystallization model in order to describe the flow-induced and quiescent crystallization of an unreinforced semi-crystalline thermoplastic material during injection molding. The crystallization model is defined alongside crystallization-dependent viscosity, PVT and solidification models in the commercial software Autodesk® Moldflow® Insight 2021 using the Solver API feature. The model parameters are identified using a calibration scheme that employs three surrogate models representing the simulated pressure results to perform a multi-objective optimization. The fill predictions as well as the calculated pressure fields are presented using the calibrated model parameters in comparison to those measured during the actual injection molding of a polyoxymethylene part with different process conditions. The results show major improvements in the predictions of the pressure signals as well as the filling status of the produced parts and the estimated skin layer thicknesses formed under high-shear conditions. Additionally, the calibrated models are tested using various mold geometries to assess the calibrated models' performance.

Keywords: surrogate modeling, injection molding, crystallization, simulation, thermoplastic, model parameter, metamodel.